Physics-Based Control-Oriented Modelling for Floating Offshore Wind Turbines

by

Jeffrey R. Homer

B.A.Sc., The University of British Columbia, 2013

A THESIS SUBMITTED IN PARTIAL FULFILLMENT OF
THE REQUIREMENTS FOR THE DEGREE OF

MASTER OF APPLIED SCIENCE

in

The Faculty of Graduate and Postdoctoral Studies

(Mechanical Engineering)

THE UNIVERSITY OF BRITISH COLUMBIA

(Vancouver)

September 2015

Abstract

As offshore wind technology advances, floating wind turbines are becoming larger and moving further offshore, where wind is stronger and more consistent. Despite the increased potential for energy capture, wind turbines in these environments are susceptible to large platform motions, which in turn can lead to fatigue loading and shortened life, as well as harmful power fluctuations. To minimize these ill effects, it is possible to use advanced, multi-objective control schemes to minimize harmful motions, reject disturbances, and maximize power capture. Synthesis of such controllers requires simple but accurate models that reflect all of the pertinent dynamics of the system, while maintaining a reasonably low degree of complexity.

In this thesis, we present a simplified, control-oriented model for floating offshore wind turbines that contains as many as six platform degrees of freedom, and two drivetrain degrees of freedom. The model is derived from first principles and, as such, can be manipulated by its real physical parameters while maintaining accuracy across the highly non-linear operating range of floating wind turbine systems. We validate the proposed model against advanced simulation software FAST, and show that it is extremely accurate at predicting major dynamics of the floating wind turbine system.

Furthermore, the proposed model can be used to generate equilibrium points and linear state-space models at any operating point. Included in the linear model is the wave disturbance matrix, which can be used to accommodate for wave disturbance in advanced control schemes either through disturbance rejection or feedforward techniques. The linear model is compared to other available linear models and shows drastically improved accuracy, due to the presence of the wave disturbance matrix.

Finally, using the linear model, we develop four different controllers of

increasing complexity, including a multi-objective PID controller, an LQR controller, a disturbance-rejecting H_∞ controller, and a feedforward H_∞ controller. We show through simulation that the controllers that use the wave disturbance information reduce harmful motions and regulate power better than those that do not, and reinforce the notion that multi-objective control is necessary for the success of floating offshore wind turbines.

Preface

This dissertation is original intellectual property of the author, Jeffrey Homer, under supervision of Dr. Ryozo Nagamune.

A version of Chapters 3 and 4 has been published in:

- J. R. Homer and R. Nagamune, Control-oriented physics-based models for floating offshore wind turbines, in the *Proceedings of 2015 American Control Conference*, Chicago, IL, USA, July 1–3, pp. 3696–3701.

I performed this work independently and wrote all of the manuscript, under guidance of Dr. Ryozo Nagamune.

Table of Contents

Appendices

List of Tables

List of Figures

Nomenclature

	General Non-Linear Model Variables
f	The general non-linear model function
$\mathbf{x}$	The state vector for the proposed non-linear model
$\mathbf{u}$	The input vector for the proposed non-linear model
$\mathbf{v}$	The wind disturbance vector for the proposed non-linear model
$\mathbf{w}$	The wave disturbance vector for the proposed non-linear model
$\mathcal{F}^0$	The world frame, also can be written without superscript
$\mathcal{F}^b$	The body coordinate frame
$\mathcal{F}^n$	The nacelle coordinate frame
$\mathcal{F}^s$	The shaft coordinate frame
$\mathcal{F}^r$	The rotor coordinate frame
$\mathcal{F}^g$	The generator coordinate frame
$\hat{e}_i$	The unit vector about axis i
$\vec{x}_g$	The displacement vector, also the vector between the origins of the world and body frame, in the world coordinate system
x_g	The first component of $\vec{x}_g$
y_g	The second component of $\vec{x}_g$
z_g	The third component of $\vec{x}_g$
$\underline{\mathrm{R}}$	The rotation matrix that represents the rotation from the world frame to the body frame
$\vec{\theta}$	The orientation quasi-vector whose components make up the rotation matrix $\underline{\mathrm{R}}$
θ_x	The first component of $\vec{\theta}$
θ_y	The second component of $\vec{\theta}$
θ_z	The third component of $\vec{\theta}$
θ_r	The azimuth angle of the rotor, also the rotation between the shaft frame and the rotor frame
ω_r	The rotor speed
θ_g	The azimuth angle of the generator, also the rotation between the shaft frame and the generator frame

	General Non-Linear Model Variables (cont'd)
ω_g	The generator speed
β	The collective blade pitch angle
T_g	The generator torque
γ	The yaw angle, also the rotation between the body frame and nacelle frame
v_x	The first component of the wind disturbance vector
v_y	The second component of the wind disturbance vector
v_z	The third component of the wind disturbance vector
$\vec{w}_{v,i}$	The wave disturbance velocity vector at column i
$\vec{w}_{a,i}$	The wave disturbance acceleration vector at column i
$w_{p,i}$	The wave disturbance dynamic pressure at column i
$w_{h,i}$	The wave disturbance height at column i
$\vec{f}_F$	The force model for the non-linear model function
$\vec{f}_T$	The torque model for the non-linear model function
f_Q	The shaft model for the non-linear model function
$\vec{F}_A$	The total aerodynamic force
$\vec{F}_B$	The total buoyancy and gravity force
$\vec{F}_C$	The total catenary line force
$\vec{F}_D$	The total drag force
T_r	The aerodynamic rotor torque
$\vec{H}_r$	The angular momentum vector of the rotor about the rotor axis
$\vec{T}_{gyro}$	The gyroscopic torque that the rotor induces on the WTS
$\underline{\underline{\mathrm{R}}}_x(a)$	A rotation of angle a about the x axis
$\underline{\underline{\mathrm{R}}}_y(a)$	A rotation of angle a about the y axis
$\underline{\underline{\mathrm{R}}}_z(a)$	A rotation of angle a about the z axis
	General Constants for the Sample WTS
g	The gravitational constant
m_g	The physical mass of the wind turbine system
$\vec{m}_a^b$	The hydrodynamic added mass vector
$\underline{\underline{\mathrm{I}}}_g^b$	The moment of inertia of the wind turbine system, given in the body frame
J_r	The rotor inertia
J_g	The generator inertia

Aerodynamic Constants for the Sample WTS

ρ	The air density
A_r	The swept area of the rotor
C_t	The thrust coefficient
C_p	The power coefficient
λ	The tip-speed ratio, given by the speed of the blades at the tip divided by the wind speed
$\vec{v}_n$	The wind speed projected onto the rotor axis
θ_{tilt}	The tilt angle of the rotor shaft with respect to $\hat{e}_2^b$
$\vec{r}_{gt}^{\,b}$	The displacement vector between the center of gravity of the WTS and the center of thrust, given in the body frame
P	The aerodynamic power
N_{GR}	The drivetrain gear ratio
k	The drivetrain stiffness on the rotor side
b	The drivetrain damping constant on the rotor side

Hydrodynamic Constants for the Sample WTS

ρ_w	The water density
A_i	The cross-sectional area of cylinder i
l_i	The length of cylinder i
$l_{0,i}$	The submerged length of uppermost cylinder i in the undisplaced state of the wind turbine system
$\vec{r}_{gi}^{\,b}$	The distance from the center of gravity of the wind turbine system to the center of volume of cylinder i, in the body frame coordinate system
$\vec{r}_{gi,0}^{\,b}$	The distance from the center of gravity of the undisplaced wind turbine system to the center of submerged volume of cylinder i, in the body frame coordinate system
$K_{d,i}$	The drag constant from the Morison equation for cylinder i
$K_{a,i}$	The inertial constant from the Morison equation for cylinder i
$K_{dh,i}$	The heave drag constant from the Morison equation for cylinder i
$K_{ah,i}$	The heave inertial constant from the Morison equation for cylinder i

Mooring Line Constants for the Sample WTS

L	The mooring line length
x	The horizontal position of the attachment point relative to the anchor of the 2-D mooring line representation
y	The vertical position in the attachment point relative to the anchor in the 2-D mooring line representation
F_x	The horizontal force of the 2-D mooring line representation at the attachment point
F_y	The vertical force of the 2-D mooring line representation at the attachment point
w	The equivalent weight of the mooring line in water
$\vec{x}_{a,i}$	The position of the anchor point for mooring line i
$\vec{x}_{t,i}$	The displacement vector between the anchor point and attachment point of mooring line i
$\vec{r}^{\,b}_{gci}$	The distance between the center of gravity of the WTS and the attachment point of mooring line i, in the body frame

Wave Equation Parameters

h	The height of a regular wave. For irregular waves, the height of each monochromatic frequency is distinguished by the subscript i
A	The amplitude of a regular wave. For irregular waves, the amplitude of each monochromatic frequency is distinguished by the subscript i
ω	The temporal frequency of a regular wave. For irregular waves, each of the frequencies is distinguished by the subscript i
ϕ	The phase angle of a regular wave. For irregular waves, the phase angle of each monochromatic frequency is distinguished by the subscript i
ζ	The summation of the temporal, spatial and phase angle. For irregular waves, this summation is distinguished by the subscript i for each monochromatic frequency
α	The angle indicating the wave direction about the $\hat{e}_e$ axis
$\vec{x}_w$	The displacement vector indicating the location in the $\hat{e}_1$-$\hat{e}_2$ plane that we would like the wave information
z	The vertical distance from the mean water level to the location we would like the wave information
$\vec{v}$	The total wave velocity vector
$\vec{a}$	The total wave acceleration vector
P_d	The total dynamic pressure of the wave

	Wave Equation Parameters (cont'd)
$S(\omega)$	The Pierson-Moskowitz spectrum magnitude at frequency ω
s_β, s_α	The constants used in the Pierson-Moskowitz spectrum fit
U_x	The mean wind velocity at an elevation x m
h_x	The height of x m
κ	The wind power exponent for the wind power law
	Linearization Parameters
$\mathbf{p}$	The operating point for linearization
$\mathbf{x_{op}}$	The state vector at the operating point $\mathbf{p}$
$\mathbf{u_{op}}$	The control input vector at the operating point $\mathbf{p}$
$\mathbf{v_{op}}$	The wind disturbance vector at the operating point $\mathbf{p}$
$\mathbf{w_{op}}$	The wave disturbance vector at the operating point $\mathbf{p}$
$\underline{\mathrm{A}}\|_{\mathbf{p}}$	The linear state matrix for the linearization at $\mathbf{p}$
$\underline{\mathrm{B}}\|_{\mathbf{p}}$	The linear input matrix for the linearization at $\mathbf{p}$
$\underline{\mathrm{B}}_v\|_{\mathbf{p}}$	The linear wind disturbance matrix for the linearization at $\mathbf{p}$
$\underline{\mathrm{B}}_w\|_{\mathbf{p}}$	The linear wave disturbance matrix for the linearization at $\mathbf{p}$
$\underline{\mathrm{C}}\|_{\mathbf{p}}$	The linear output state matrix for the linearization at $\mathbf{p}$
$\underline{\mathrm{D}}\|_{\mathbf{p}}$	The linear input matrix for the outputs of a linearization at $\mathbf{p}$
$\underline{\mathrm{D}}_v\|_{\mathbf{p}}$	The linear output wind disturbance matrix for the linearization at $\mathbf{p}$
$\underline{\mathrm{D}}_w\|_{\mathbf{p}}$	The linear output wave disturbance matrix for the linearization at $\mathbf{p}$
n_x	The number of states at the equilibrium point
n_u	The number of inputs at the equilibrium point
n_v	The number of wind disturbances at the equilibrium point
n_w	The number of wave disturbances at the equilibrium point
$\mathbf{p_u}$	The parameters to-be-determined by the equilibrium point solver
$\underline{\mathrm{T}}_{\mathbf{p}}$	The transformation from the operating point $\mathbf{p}$ to $\mathbf{p_u}$
f_u	The parts of the non-linear function necessary that describe the to-be-determined parameters only
$\underline{\mathrm{T}}_f$	The transformation from the non-linear function f to f_u
g_o	The non-linear output function

Controller Design Parameters

G_i	The PID system i
$\underline{\mathrm{J}}$	The input weighting matrix for LQR design
$\underline{\mathrm{Q}}$	The combined state-output weighting function for LQR design
$\underline{\mathrm{Q}}_x$	The state weighting function for LQR design
$\underline{\mathrm{Q}}_y$	The output weighting function for LQR design
$\mathbf{z}$	The combined state-output vector for LQR design
$\underline{\mathrm{P}}$	The observer transformation matrix
$\underline{\mathrm{B}}_y$	The observer output B matrix
$\underline{\mathrm{B}}_u$	The observer input B matrix
$\underline{\mathrm{L}}$	The observer gain
$\underline{\mathrm{A}}_{obs}$	The observer state matrix
$\tilde{\underline{\mathrm{A}}}_{11}$	The first block of the transformed state matrix used for observer design
$\tilde{\underline{\mathrm{A}}}_{12}$	The second block of the transformed state matrix used for observer design
$\tilde{\underline{\mathrm{A}}}_{21}$	The third block of the transformed state matrix used for observer design
$\tilde{\underline{\mathrm{A}}}_{22}$	The fourth block of the transformed state matrix used for observer design
$\tilde{\underline{\mathrm{B}}}_1$	The first block of the transformed input matrix used for observer design
$\tilde{\underline{\mathrm{B}}}_2$	The second block of the transformed input matrix used for observer design
$\mathbf{x_{aug}}$	The augmented state vector for H_∞ design
$\mathbf{e}$	The output vector for H_∞ design
$\tilde{\mathbf{e}}$	The output minimization vector for H_∞ design
$\tilde{\mathbf{u}}$	The input minimization vector for H_∞ design
$\tilde{\mathbf{w}}$	The weighted wave disturbance vector for H_∞ design
$\mathbf{u_k}$	The controller output for H_∞ design
$\underline{\mathrm{P}}_{aug}$	The augmented plant for H_∞ design
$\mathbf{u_P}$	The proportional control input for H_∞ design
$\mathbf{u_I}$	The integral control input for H_∞ design
$\mathbf{x_I}$	The integral state vector for H_∞ design
$\mathbf{x_w}$	The wave disturbance state vector for H_∞ design

	Controller Parameters (cont'd)
$\underline{\mathrm{W}}_u$	The input weighting function for H_∞ design
$\underline{\mathrm{W}}_e$	The output weighting function for H_∞ design
$\underline{\mathrm{W}}_v$	The wind disturbance weighting function for H_∞ design
$\underline{\mathrm{W}}_w$	The wave disturbance weighting function for H_∞ design
$\underline{\mathrm{W}}_{w,a_z}$	The transfer function used to reject wave acceleration in the heave direction
$\underline{\mathrm{A}}_{W,w}$	A part of the state-space system representing the wave disturbance weighting function
$\underline{\mathrm{B}}_{W,w}$	A part of the state-space system representing the wave disturbance weighting function
$\underline{\mathrm{C}}_{W,w}$	A part of the state-space system representing the wave disturbance weighting function
$\underline{\mathrm{D}}_{W,w}$	A part of the state-space system representing the wave disturbance weighting function
$P_{z,i}$	The measured pressure at the bottom of heave plate i
$\underline{\mathrm{C}}_{P,w}$	The linear output matrix describing the effect of states on the heave pressure
$\underline{\mathrm{D}}_{P,w}$	The linear output matrix describing the effect of control inputs on the heave pressure
v_r	The measured relative wind velocity at the center of thrust i
$\underline{\mathrm{C}}_{v_r}$	The linear output matrix describing the effect of states on the relative wind velocity
$\underline{\mathrm{D}}_{v_r}$	The linear output matrix describing the effect of control inputs on the relative wind velocity
$\underline{\mathrm{D}}_{v_r,v}$	The linear output matrix describing the effect of wind disturbance on the relative wind velocity

List of Abbreviations

DAC	Disturbance accommodating controller
DOF	Degree of freedom
FAST	Fatigue, aerodynamics, structures and turbulence (simulation software)
GSPI	Baseline gain-scheduled PI controller
H_∞	H-Infinity control
IBP	Individual blade pitch
LQR	Linear quadratic regulator
MBC	Multi-blade coordinate transformation
MOPID	Proposed multi-objective PID controller
PID	Proportional-Integral-Derivative (control)
RMS	Root-mean-square
TSR	Tip-speed-ratio, or the ratio of the velocity of the blade tip to the mean wind speed
WTS	The wind turbine system (wind turbine and platform)

Acknowledgements

I would like to thank my supervisor Prof. Ryozo Nagamune for his incredible support throughout the duration of my degree. The amount of hours he spent teaching me, discussing problems and solutions, and reviewing my work, are far and beyond what I could have asked for.

I am very grateful to my committee members Prof. Jon Mikkelsen and Prof. Juri Jatskevich for taking the time to review my thesis, and for providing me with invaluable feedback.

I would also like to thank Dr. Jason Jonkman and Dr. Alan Wright from the National Renewable Energy Laboratory in the United States for answering all my questions related to wind turbine simulation software FAST, and providing me with important information on its usage.

Finally, this thesis was supported by the National Sciences and Engineering Research Council of Canada and the Institute for Computing, Information and Cognitive Systems at the University of British Columbia.

Dedication

To my friends and family

Chapter 1

Introduction

1.1 Motivation

Wind power has grown enormously over recent years. Over the 2007-2013 period, the United States saw an average 7.1 GW increase in wind power capacity per year. If the same trend were to continue over the next ten years, approximately 40% of the entire country's electricity generation could be supplied via wind power [2]. As wind turbine technology advances, researchers are beginning to look toward offshore environments where wind is stronger and more consistent than wind on land. By the end of 2012, 1,662 offshore wind turbines had been constructed across 10 European countries and generated enough electricity to power five million houses [3]. A further trend for offshore wind turbines is that as the industry evolves, larger wind turbines are being constructed further from the coast in deeper waters, where energy resources are plentiful and floating platforms are necessary. For example, the average water depth for offshore wind farms went from 22m in 2012 to 215m for projects announced for 2013 and beyond. Likewise, average distance from shore went from 29km to 200km [3].

An important factor, particularly for deep water floating offshore wind turbines, is the design of the base, or floating platform. Typically, a balance must be made between capital cost and stability. An expensive base is undesirable from an economic perspective, however a low-cost platform that is sensitive to wind and wave effects can allow harmful fatigue loads to significantly reduce the operating life of the wind turbine. Furthermore, the dynamic response of a particular platform will be affected not only by its physical characteristics, but also by its control scheme [3]. Generally, the optimal platform design is a tightly coupled problem involving the water depth,

the site's typical wind and wave characteristics, the physical characteristics of the mounted wind turbine, and the control scheme used. Figure 1.1 shows several offshore wind turbine concepts for various water depths.

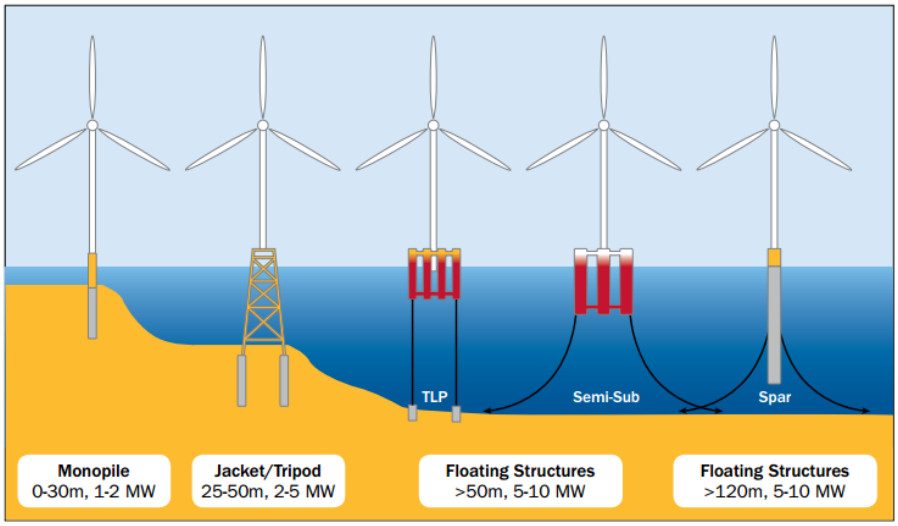

Figure 1.1: Evolution of Offshore Wind Turbines (Source: Principle Power)

It is possible to reduce the high capital costs associated with the floating platform via intelligent, multi-objective control schemes. That is, instead of simply maximizing power capture, the many available actuators can be utilized to achieve secondary objectives of regulating platform motions and drivetrain loads. Many researchers have shown that such advanced control can significantly increase fatigue life of deep water floating wind turbine systems at a small deficit or sometimes even positive effect to captured power. For example, the multi-objective LQR controller used in [4] was able to reduce platform pitch motions by 18%, compared to a simple baseline PI gain-scheduled controller, with a negligible effect to power capture. Since the floating wind turbine is subject to large wind and wave disturbances, it is no surprise that there is huge potential in advanced controllers that predict and accommodate for such disturbances. In particular, one study showed that using wind disturbance estimation, a 38% reduction in tower side-to-side fatigue loading could be made while reducing power error by 44%, relative

to a simple baseline controller [5]. Controllers that utilize wave disturbance information are also very promising, but less common in research due to the difficulty in acquiring a linear wave disturbance matrix with existing modelling methods. In general, control of floating offshore wind turbines is trending toward multi-objective, disturbance-accommodating control; the success of which depends on effective mathematical models.

Another important consideration for both onshore and offshore floating wind turbines is wind farm optimization. Because wind changes in both magnitude and direction, and because wind turbines that are aligned in the direction of the wind will interfere with the power capture of one another, it is important to place the wind turbines such that cost of energy is minimized [6]. The layout problem is especially complicated in the case of offshore wind turbines because, while available wind energy increases with water depth and turbine spacing, so do the cost of the support platform required and the cost of electrical interconnection [7]. Furthermore, while in operation, it is inevitable that some turbines will be operating in the wake of other turbines, resulting in a decrease in power capture of the farm. It is possible to minimize this power loss by developing a combined feedback control strategy for all the wind turbines that are aligned in each other's wake. Generally, highly simplified models of the individual turbines are used to estimate the total power capture of the farm and from them design control strategies, such as in [8] and [9]. In both of these models, relative motion of the wind turbines and feedback control of nacelle yaw have been neglected. With a slightly more advanced model, both the relative motion of the turbines and nacelle yaw control may be utilized to further optimize wind farm control.

Mathematical modelling of key dynamics represents an additional challenge for the success in analysis and control of floating offshore wind turbines. Because of the mobility of the floating platform, and the flexibility of such a massive structure, a high fidelity model requires a massive amount of states. On the more complex end of the modelling spectrum, there exists a high fidelity simulator built by the National Renewable Energy Laboratory called FAST (Fatigue, Aerodynamics, Structures, Turbulence). FAST, which is described in [10], has 44 states in its full form, which is far too many for

model-based controller design. On the other hand, simpler control-oriented models have been shown to accurately represent the important dynamics of the system and to be suitable for controller design, such as the 2-D model in [11]. In this way, there is a need for a control-oriented model with adequate degrees of freedom to represent all the important dynamics of the floating wind turbine system, but simple enough for controller design.

1.2 Problem Statement

Due to the size and mobility of floating platforms, effective control schemes for offshore wind turbines must incorporate both power production and fatigue minimization as control objectives to maximize the cost effectiveness of offshore wind energy. The construction of controllers depends on effective control-oriented models that contain all the relevant dynamics of the system, including the effects of wind and wave disturbances, while containing a minimal number of states. Existing models either lack the wave disturbance relationship [10], or the number of degrees of freedom to adequately predict the highly coupled motions of the non-linear system [11]. In this thesis we propose a simple control-oriented, physics-based model that satisfies the above requirements, and using it we design several controllers to prove the potential improvements that are possible for both power capture and reduction of fatigue loads.

1.3 Research Objectives

The objectives of this thesis can be summarized as follows

- Create and validate a simplified control-oriented model that
  - is modular and easily adjustable for various systems,
  - includes effects of wind and wave disturbance,
  - can be used to generate equilibrium points for linearization, and
  - can be used to create linear state-space models including the wind and wave disturbance information.

- Use linear state-space models to construct advanced controllers that
  - utilize wind and wave disturbance information, and
  - perform better than existing controllers due to consideration of disturbance in their design.

1.4 Thesis Outline

The thesis has been organized as follows. In Chapter 2, a literature review of existing research relevant to this thesis is conducted. First, we describe a baseline offshore wind turbine that has been used extensively in research, and that will be used for validation purposes in this thesis. Next, existing modelling methods for floating offshore wind turbines are described and compared. Finally, advanced control techniques based on these mathematical models are explored. Following this preliminary chapter, in Chapter 3, we propose, describe, and validate our own simplified, physics-based non-linear model. This proposed model is given in both a general form, which can easily be extended to different floating offshore wind turbine systems, and also more specifically for the sample wind turbine. For validation we perform multiple tests that cover a wide range of possible operating conditions, and compare the non-linear model results with those from the high-fidelity simulator FAST. Next, Chapter 4 presents how we obtain a linear model from the proposed non-linear model. This chapter also covers the generation of equilibrium points, where linearization is possible. Finally, we validate the linear model with an all-encompassing realistic open-loop test, compared to both the non-linear model and FAST. In Chapter 5, we design several advanced controllers based on the linear model in order to verify several facts. First, we confirm the importance of multi-objective control in floating offshore wind turbine systems. After this confirmation, we show the advantages of considering wind and wave disturbance in the controller design process, both in the form of disturbance rejection, and feed-forward control. Finally, we summarize and conclude the thesis in Chapter 6, and revisit the research objectives. We will also make some concluding remarks and outline

future work.

A preliminary version of this thesis has been published in [12].

Chapter 2

Literature Review

This chapter provides a summary of the modelling and control techniques employed by other researchers on horizontal-axis floating wind turbines. An introduction to the fundamentals of simple wind turbine modelling and control strategies can be found in [13]. Offshore wind turbine control presents further challenges, which were introduced and explained in [14]. We begin the literature review by detailing a baseline wind turbine that is used copiously in research, as well as in this thesis. In the next section, two existing mathematical models for floating wind turbines are described with their advantages and disadvantages. One such model is a highly complex simulation-oriented model, and the other, a simplified, control-oriented 2-D model. Finally, following the model descriptions, a thorough survey of existing wind turbine control strategies is carried out.

2.1 Baseline Offshore Wind Turbine

The baseline offshore wind turbine is a virtual wind turbine created by the National Renewable Energy Laboratory (NREL) in the United States. It is by far the most commonly used wind turbine by control researchers for realistic simulation purposes [4, 5, 15–17], as it is publicly available in open source simulation software FAST [10], and more importantly it provides a common ground for comparison purposes. The combined wind turbine system, which we call the WTS throughout this thesis, consists of both the wind turbine and the floating platform upon which the turbine sits. In this thesis, whenever validations are conducted for proposed modelling and control methods, we consider the semi-submersible platform specifically, which is taken from [1] and shown with the attached wind turbine in Figure 2.1.

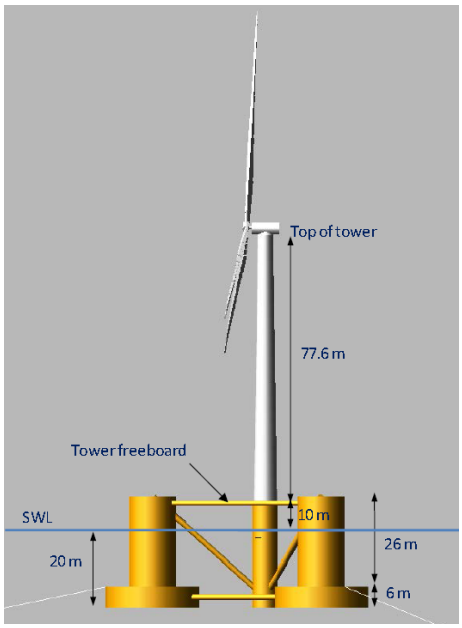

Figure 2.1: 5MW Baseline Wind Turbine on the Semi-Submersible Platform (Taken from [1]).

The wind turbine is extensively described in [18], including its structural, geometric, aerodynamic, and drivetrain properties. It also includes a baseline PI-gain-scheduling controller for collective blade pitch control above rated wind speed that is commonly employed in literature as a comparison object for other controllers. The tower is 87.7m tall, with a blade swept diameter of 126m. Its generator is rated for 5MW at 1173.7rpm, which makes the rotor side rated speed 12.1rpm, after a 97 times gear reduction. The baseline wind turbine was initially designed as an onshore wind turbine, but it was eventually extended for offshore use, with most properties remaining the same. For offshore applications, various baseline platforms have been designed and detailed by NREL. These platforms include the barge [19], spar-buoy [20], tension-leg platform [21], and finally the semi-submersible platforms [1]. Even though the modelling and control results in this thesis are applicable to all these platforms, wherever we show the applicability, we will focus on the semi-submersible platform due to its recently increasing

popularity.

The semi-submersible platform that was presented in [1] consists of three outer buoyant columns arranged in an equilateral triangular fashion, in addition to the central column that supports the tower. The platform has a mass of 13.5 ktonnes, with a center of mass at 13.46m below sea level. Its stability comes from a combination of its low center of gravity and largely spaced out columns. Compared to other platforms, the experienced fatigue loading for given wind and wave disturbances is very low, with the exception of tower loading [22]. Since tower loads can be reduced by limiting platform motions, the semi-submersible platform is a good test subject for platform motion control. From an economic perspective, the levelized cost of energy has been compared between various types of floating and bottom-fixed wind turbines [23]. In this study, all aspects of the manufacturing, installation and maintenance were considered for the platforms, assuming the same average wind speed and years of operation for all concepts. The semi-submersible was found to have very low installation and mooring line costs, comparable grid, development and turbine costs, but high structural costs. Overall, the semi-submersible was deemed slightly more expensive than its competitors, however it also experiences minimal increase in cost with increasing depth. Since wind power is more available further offshore, at increasing water depths, it is expected that the cost for the semi-submersible platform in this analysis is overestimated for deep-water locations.

The modelling for floating wind turbines plays an essential role in subsequent controller design. Existing modelling techniques that can be applied to the baseline floating offshore wind turbines, including the baseline semi-submersible wind turbine, are explained in the following section.

2.2 Physical Modelling of Floating Offshore Wind Turbines

Multi-objective control is a necessity for floating offshore wind turbines due to the significant structural fatigue damage that occurs when using simple

power-optimization control strategies [16]. This presents a need for mathematical models of the floating wind turbine system that accurately reflect all the important dynamics of the complex system. In particular, the mathematical model must accurately predict the power extraction from wind, as well as the major platform motions which cause the harmful tower bending loads [5]. Several general and publicly available mathematical models exist for floating wind turbine systems, including the highly-complex but accurate simulator FAST developed by Jonkman and Buhl [10], and the simplified, control-oriented model proposed by Betti et al. [11]. Other researchers have used their own mathematical models for floating wind turbine systems, as in [24] and [25]. However, the complex model in [24] is not open-source, and the model in [25] does not contain platform motion beyond a 1-D horizontal displacement of the nacelle. The latter model was also not validated either experimentally or in simulation. Therefore, the review of existing models will focus on FAST, as well as the model in [11] which we call *Betti model* in this thesis.

FAST is an open-source, highly complex non-linear simulator for onshore and offshore wind turbines, developed at NREL in the United States [10]. It is based on a mixture of both fundamental physical laws and empirical relationships, and has been validated by Germanischer Lloyd, the world's largest renewable energy consultancy, for several onshore wind turbines. FAST calculates the aerodynamic loads on the wind turbine using full field in-flow data, solving for the the rotor-wake effects and blade-element forces along each blade. Hydrodynamic loads include hydrostatic, radiation, diffraction, and viscous forces, calculated over the entire platform structure, including support beams. All actuators and electronic devices associated with the control are also modelled. Finally, the structural dynamics are modelled using first or second order flexibility modes for all three blades, about two axes, and the tower, about two axes. Although the non-linear FAST model is much too complex for controller design, it is capable of generating linear state-space models numerically at static equilibrium points. These generated state-space models have been used quite readily in wind turbine control research, including in [26], [27], and [5]. As we will see, disturbance accom-

modation has been very important in the control of floating wind turbines, and although FAST is able to produce a linear wind disturbance matrix, to date, it is not able to produce a wave disturbance matrix. This means that the FAST model cannot be used for advanced control design techniques that take into account rejection of wave disturbance. Furthermore, the complexity of building a FAST project may not be available for the control engineer, as it requires a highly detailed knowledge of the geometric, inertial, elastic, aerodynamic and hydrodynamic properties of the floating wind turbine. On the other hand, the Betti model, for instance, is able to accurately reproduce the same major platform motions as FAST, while requiring far fewer input parameters.

The Betti model (BM) is a simplified 2-D control-oriented model of the floating wind turbine. In contrast to FAST which has 44 states in full form, BM only has 7. The simplicity of the model is achieved by constructing an equivalent 2-D wind turbine and assuming all wind and wave disturbances act only in the 2-D plane. The authors further simplified the non-linear system by using lumped forces and assuming no flexibility in the wind turbine structure. Despite being far less complex, it was shown in [11] and [28] that such large simplifications had very little consequence to the accuracy of the major platform motions and power capture model under 2-D disturbances for their tests on the 5MW baseline wind turbine on a tension-leg type platform. The authors of this paper validated their model by running identical open- and closed-loop tests in the simulator FAST, and in their own model. To measure the similarity, they calculated the mean and standard deviations of the time series data, for both FAST and BM. With all degrees of freedom activated in FAST, the differences between the performance metrics for both models were within 10%. Like FAST, BM can be used to generate linear state-space models at specific equilibrium points, with the unique advantage of being able to generate the wave disturbance matrix. This enabled the authors to design an H_∞ controller for the entirety of the high speed wind region, called Region 3, while rejecting both wind and wave disturbances. Unfortunately, despite the accuracy of the 2-D motions, the platform motions out-of-plane are also very important for fatigue damage reduction [5].

In fact, in [4], it was shown that 2-D platform pitch control could actually induce undesired platform roll motions.

In summary, in this section, we have reviewed two existing models for floating offshore wind turbines. FAST, which was designed as a high-fidelity simulation tool, is capable of producing linear state-space models for controller design, but falls short in that it cannot produce the wave disturbance matrix. It is also extremely complex and requires a high-level knowledge of the WTS. BM addresses many of the issues with the FAST model by simplifying the equations of motion and relying on accurate estimation of 2-D platform motions to mitigate structural fatigue loading. Unfortunately the 2-D limitation is not realistic because of coupling of motion in and out of the assumed 2-D plane. Table 2.1 summarizes the differences between FAST, BM and a control-oriented model proposed in this thesis. The proposed model covers the drawbacks of the FAST and BM models, by predicting 3-D platform motions, and by including the wave disturbance matrix for disturbance rejection and feedforward control.

	FAST	BM	Proposed
States	44	8	15
Flexibility	Y	N	N
Platform Motions	3-D	2-D only	3-D
Linear model with wind disturbance matrix	Y	Y	Y
Linear model with wave disturbance matrix	N	Y	Y

Table 2.1: Complexity and Functionality Comparison of Models.

In the next section, we consider the existing control research that has been done using the existing models.

2.3 Multivariable Control for Reduction of Fatigue Loads

The main control objective for all wind turbines, both on- and offshore, is to maximize the cost-effectiveness of wind energy. For onshore wind turbines, this typically translates to maximizing the power capture within the capacity of the on-board generator. A good example of a controller with such a control objective is described in [18]. The designed PI gain-scheduled controller maximizes power capture using blade pitch angle actuation in the operating region where extracted power is less than the maximum capacity of the generator (Region 2). Above the transitional wind speed (Region 3), where the potential power extraction exceeds the generator limit, the controller simply regulates power at the maximum capacity. On the other hand, for floating offshore wind turbines, the same control strategies are not optimal due to the fatigue life impact of uncontrolled platform motions. It was shown in [16] that traditional onshore control strategies can actually lead to negative damping of platform motions, exacerbating the lifetime reduction of floating wind turbines due to wind and wave disturbances. Therefore, multivariable control strategies which target both power maximization and platform motion reduction, as in [4, 5, 11, 15, 17, 24–27, 29–31], are necessary for the success of floating offshore wind turbines. This subsection reviews the existing advanced control techniques for dealing with this multi-objective problem.

2.3.1 Multi-Objective Control

In [4], the authors developed a full-state-feedback controller for Region 3 operation of the 5MW baseline wind turbine on a barge platform, using the LQR method. The control objectives for this controller were to regulate both rotor speed and platform pitch. The linear model required for controller synthesis was created using FAST's linearization feature, and was chosen to have four states including rotor speed, platform pitch and their respective time derivatives. By tuning the Q and R gains, specifically to put heavy

weight on the platform pitch speed, the authors were able to achieve a 21% reduction in rotor speed root-mean-square error, an 18% reduction in platform pitch oscillations, and a 23% reduction in platform pitch rate compared to the baseline PI controller described in [18] for a full DOF FAST simulation. The authors note that the improvements come at a cost to blade pitch actuation and blade flapping modes, and they do not quantify either the improvement or deterioration of power regulation relative to the baseline controller. In the same paper, the authors describe and design a rudimentary individual blade pitching controller with further potential for improvement, however a more complete account of this is described in another paper, described next.

It was described in [5] a disturbance-accommodating, individual blade pitch (IBP) controller for the 5MW baseline wind turbine on a tension-leg platform. The purpose of IBP is to utilize each blade individually to create asymmetric loads that can mitigate platform motions and blade bending loads even more than collective blade pitch controllers. For example, platform pitch can be controlled by adjusting the pitch angles of top-most blade and bottom-most blade, oppositely, without affecting the net power capture or net thrust force. Because the blades are constantly rotating, IBP is inherently a periodic problem. However, to avoid the complexity of periodic control, the authors employed a a method called Multi-blade coordinate (MBC) transformation. MBC effectively captures the periodic properties of a system and transforms them into a linear time-invariant model, which is much simpler to deal with from a controls perspective. The other method that the authors make use of is that of Disturbance Accommodating Control (DAC). In this method, persistent disturbances that are not measurable are estimated by assuming a specific disturbance waveform and by the use of measurable states of the system. The authors use this method to reject the periodic wind disturbance of the system. The final proposed controller was based on a 6 DOFs linearized state-space model created using FAST, including platform roll, pitch and yaw, tower side-side bending, rotor speed and drivetrain twist. Following the synthesis of the IBP DAC, a full DOF Region 3 simulation was carried out using FAST for both the proposed con-

troller and a modified version of the baseline controller made for the offshore tension-leg system. The simulation results showed 44% reduction in power error 73% reduction in rotor speed error, 13% reduction in platform pitching and 38% reduction in tower side-side fatigue loading relative the baseline PI controller.

Another example of the use of wind estimation for floating wind turbine control can be found in [25]. In this paper, the authors a simplified 8-state model was adopted that includes the drivetrain dynamics, the tower-top motion, and the wind turbulence to develop an optimal LQR controller. The authors suggested the use of an extended Kalman filter to estimate the non-periodic relative wind speed at the wind turbine hub using the realistic measurements of rotor velocity, blade pitch angle and generator torque. An observer was also designed to estimate what the authors deem as unmeasurable or unrealistically measurable states. Similar to the previous works, the proposed controller was compared to the baseline gain-scheduled PI controller by running Region 3 simulations with stochastic wind and wave conditions. The proposed controller achieved a 19% reduction in platform pitch moments, a 6% reduction in tower base foreaft moments, and a 24% reduction in generator speed standard deviation, compared to the baseline controller. A compromise was made however, as the proposed controller suffered a 5% increase in damage-equivalent-loading of the drivetrain due to torsion, compared to the baseline controller.

2.3.2 Utilization of Wave Disturbance

Despite the effectiveness of wind disturbance accommodation in research, the accommodation of waves has not been explored in very much detail. This is largely because most existing modelling techniques do not offer a way to construct the wave disturbance matrix in linear state-space models. Some attempts have been made, however, and the results are described in this subsection.

In [27], the authors developed a linear-parameter-varying model for the floating wind turbine system that depends on the frequency of the propagat-

ing ocean wave. A wave interaction analysis tool called WAMIT was utilized to generate the linear hydrodynamic damping matrix at various wave frequencies within the expected range for ocean waves. Using the set of linear models for various wind speeds and wave frequencies, the authors generated a set of LQR controllers assuming full state feedback, including the wave period and wind speed. The authors then proposed a method for estimating the peak period of the waves based on measured wave height, and a method for estimating wind speed, based on the extended Kalman filter described in [25]. Finally, they applied a gain-scheduling method to combine their set of controllers, and validate it using a realistic simulation test, compared to a baseline controller. The simulation study demonstrated that accounting for both wind and wave disturbance results in a 50% improvement in platform pitch motions, a 7-20% improvement in power capture, and a 5-17% improvement in fore-aft deflection. This comes at a cost of 150% to blade pitch activity.

In [11], the authors used their developed non-linear 2-D physics-based model to create a linear model of their system, including both the wind and wave disturbance matrices. Using this linear model, the authors developed an H_∞ controller for the entirety of Region 3 that rejects wind and wave disturbances in their expected frequency range. They compared their H_∞ regulator to the baseline GSPI controller in a realistic simulation with stochastic wind and wave disturbances. In this test, they showed a large improvement in rotor speed regulation and torque variation, at a slight cost to power regulation, platform pitch regulation, and blade pitch actuation.

The major control contributions for floating offshore wind turbines are summarized in Table 2.2, below. Here, we can clearly see the benefit of increasing the amount of information used in controller design on both power regulation and platform motion. It is expected, then, that by utilizing a model with an adequate amount of states, as well as the wind and wave disturbance matrices, we will see yet greater improvements in controller performance.

Source	States	Considers Wind	Considers Wave	Rotor Speed Regulation	Platform Motion Reduction	Power Regulation
[18]	1	No	No	0%	0%	0%
[4]	4	No	No	-21%	-18%	-
[5]	12	Yes	No	-73%	-13%	-44%
[27]	24	Yes	Partial	-	-50%	-14%
[11]	8	Yes	Yes	-66%	+37%	+22%

Table 2.2: Summary of Control Contributions of Floating Offshore Wind Turbines.

2.4 Summary

In this section, a commonly used baseline 5MW wind turbine and floating platform were outlined, existing models and their advantages and disadvantages were described, and advanced control techniques that have shown promise in maximizing the cost effectiveness of wind energy were detailed. More precisely, it was shown that simple onshore control strategies do not maximize the cost effectiveness of offshore wind power due to the neglect of structural fatigue loading and its effect on turbine lifetime, and that advanced control strategies are necessary for further reducing fatigue load. Many researchers have shown the potential in wind disturbance accommodation for fatigue reduction in floating wind turbines, but the accommodation of wave disturbance is yet to be explored. This is largely due to the inability in existing modelling techniques to generate the wave disturbance matrix, or mathematical relationship between waves and important states of the floating wind turbine system. It should be clear, then, that a control-oriented floating wind turbine model would include the ability to generate such a disturbance matrix. The following chapter will describe the process in creating such a model.

Chapter 3

Non-Linear Modelling

3.1 Introduction

The objective of this chapter is to prove that highly simplified, control-oriented models can accurately predict the dynamics of floating wind turbine systems. This is important, because it allows for the use of complex, high-information control strategies to push both the performance, and lifespan of floating wind turbine systems beyond what is possible with existing models. The first part of this chapter will formulate a higher level, generalized model, that can be extended to any floating wind turbine system with known forces and torques. The next section will detail the force and torque models for the Baseline 5MW Semi-Submersible system, and apply them to the generalized model. Finally, the performance will be measured in four distinct tests by comparing the dynamic response of the simplified model to the FAST equivalent model.

3.2 Generalized Non-Linear Model

The purpose of the control-oriented non-linear model is to accurately predict the relationship between the relevant states of the system ($\mathbf{x}$), the control inputs ($\mathbf{u}$) and the environmental wind and wave disturbances ($\mathbf{v}$ and $\mathbf{w}$). The proposed model follows the form

$$\dot{\mathbf{x}} = f(\mathbf{x}, \mathbf{u}, \mathbf{v}, \mathbf{w}), \tag{3.1}$$

where f denotes the non-linear function relating the states to the inputs and disturbances. The simplicity of the proposed model depends on several

important assumptions. First, it is assumed that the wind turbine and platform behave as a single rigid body, which we call the wind turbine system (WTS). With this assumption, we inherently neglect all flexibility and effects of flexibility of the wind turbine tower structure. Even without flexibility in the model, it is still possible to take into account fatigue load attenuation indirectly in controller design because internal fatigue loads are related to platform motion [17]. Furthermore, we assume all platform angular motions are relatively small ($\leq 10°$). Finally, we assume that the inertia tensor of the wind turbine system is constant with respect to a coordinate frame rigidly attached to its center of gravity. This last assumption is generally true if the inertia of the rotor is negligible compared to that of the platform and tower.

3.2.1 Coordinate Systems

In order to properly define the states and disturbances of the WTS, it is necessary to define a set of coordinate frames. In particular, five coordinate frames will be defined. These are illustrated in Figure 3.1.

The world frame is an inertial reference frame denoted $\mathcal{F}^0$. It is defined by its orthogonal unit vectors $\hat{e_1}^0$, $\hat{e_2}^0$ and $\hat{e_3}^0$. With respect to the world, the unit vector $\hat{e_3}^0$ points vertically upward, opposite to gravity, while unit vectors $\hat{e_1}^0$ and $\hat{e_2}^0$ point horizontally, parallel to the surface of the earth. In this thesis, any vector that does not have an attached superscript is defined in this frame.

The body frame is attached to the center of gravity of the model WTS, and is denoted $\mathcal{F}^b$. The body frame can be defined by orthogonal unit vectors $\hat{e_1}^b$, $\hat{e_2}^b$ and $\hat{e_3}^b$, which make up the principal axes of the rigid body. The unit vector $\hat{e_1}^b$ points in the nominal wind direction for an un-yawed state. The unit vector $\hat{e_3}^b$, points parallel to the tower of the wind turbine, vertically upward, from platform to nacelle. Finally, the unit vector $\hat{e_2}^b$ points orthogonally to $\hat{e_1}^b$ and $\hat{e_3}^b$ such as to satisfy the criteria of a right handed coordinate system. When the WTS is not under the influence of wind or wave disturbance, the body frame aligns with the world frame.

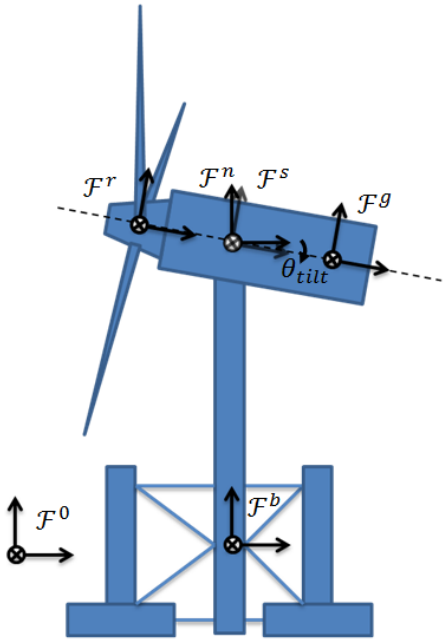

Figure 3.1: Coordinate Frames for the General Non-Linear Model.

The nacelle frame is attached to the nacelle of the WTS, at the point where the yaw axis meets the rotor axis. It is denoted $\mathcal{F}^n$. This frame can be defined by orthogonal unit vectors $\hat{e_1}^n$, $\hat{e_2}^n$ and $\hat{e_3}^n$, where $\hat{e_3}^n$ is always pointing in the same direction as $\hat{e_3}^b$. Unit vectors $\hat{e_1}^n$ and $\hat{e_2}^n$ rotate about the yaw axis of the WTS with the nacelle.

The shaft frame, $\mathcal{F}^s$, shares its origin with the nacelle frame, but is rotated with respect to $\mathcal{F}^n$ about its second axis by the constant angle θ_{tilt}. $\mathcal{F}^s$ and is composed of the orthogonal unit vectors $\hat{e_1}^s$, $\hat{e_2}^s$ and $\hat{e_3}^s$.

The rotor and generator frames align their first axes with the first axis of the shaft frame, and are denoted $\mathcal{F}^r$ and $\mathcal{F}^g$, respectively. These two frames rotate independently about $\hat{e_1}^s$ with the rotor and generator, respectively.

3.2.2 States

For controller design, it is important for the model to be as minimalistic as possible, while still maintaining adequate accuracy. Following the above

assumptions, a general floating wind turbine with six platform DOFs, and a flexible-drivetrain, will have as many as 16 states. This includes three states for both position and orientation of the platform, one azimuth angle state for each the rotor and generator, and the time derivatives of all of the above.

The three position states make up the displacement vector $\vec{x}_g = (x_g, y_g, z_g)$ $[m]$ between the origin of the world frame and the origin of the body frame, given in world frame coordinates. These three states are shown in Figure 3.2, below. Likewise, the time derivatives of the three position states are also states $\dot{\vec{x}}_g = (\dot{x}_g, \dot{y}_g, \dot{z}_g)$ $[m/s]$.

Next, if we let $\underline{\mathrm{R}}$ be the rotation matrix that specifies the orientation of the body frame $\mathcal{F}^b$ with respect to the world frame $\mathcal{F}^0$, then by consequence of the small angle assumption, we can formulate $\underline{\mathrm{R}}$ with three distinct angles such that

$$\underline{\mathrm{R}} = \begin{bmatrix} 1 & -\theta_z & \theta_y \\ \theta_z & 1 & -\theta_x \\ -\theta_y & \theta_x & 1 \end{bmatrix}. \tag{3.2}$$

The three orientation states of the WTS, then, are the three angles $(\theta_x, \theta_y, \theta_z)$ $[rad]$ that form the rotation matrix. We can also write these states more compactly as the pseudo-vector $\vec{\theta}$. The three orientation states are shown in Figure 3.2, below. Three additional time derivative states exist, and are $\dot{\vec{\theta}} = (\dot{\theta}_x, \dot{\theta}_y, \dot{\theta}_z)[rad/s]$.

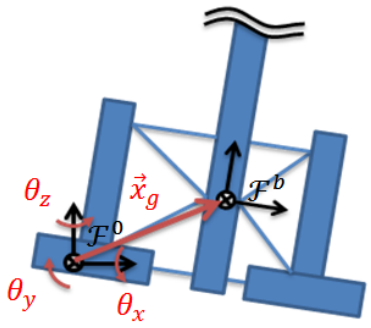

Figure 3.2: Position and Orientation States.

The rotor azimuth angle, $\theta_r[rad]$, is defined as the angle between the third axis of the rotor frame, and the third axis of the shaft frame. Likewise, the generator azimuth angle, $\theta_g[rad]$ is defined similarly between the generator frame and the shaft frame. If our model depends on one or both of these angles explicitly, they make up the azimuth states of the WTS. However, it is possible that only the difference between these two angles is important. In this case, we can define the azimuth state to simply be the difference between the rotor angle, and the equivalent generator angle on the low-speed side, or $\theta_r - \frac{1}{N_{GR}}\theta_g$, where N_{GR} is the gear ratio between the rotor and generator side shafts. In either case, it is necessary to define two derivative states, as the aerodynamic equations of motion in Section 3.3.2 depend on the rotor speed explicitly. These derivative states can be written as ω_r $[rad/s]$ and ω_g $[rad/s]$, for rotor speed and generator speed, respectively.

The rotor and generator azimuth angles are illustrated in Figure 3.3. The three position and orientation states of the WTS are illustrated in Figure 3.2.

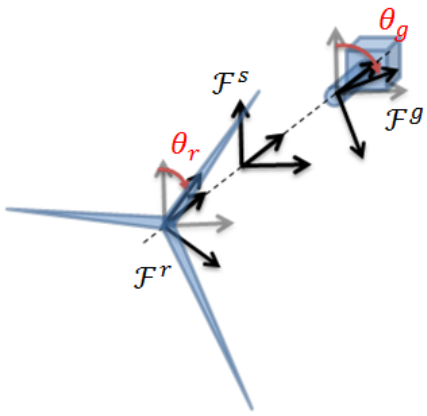

Figure 3.3: Rotor and Generator Angle States.

To recap, the state vector of the WTS can be written as follows:

$$\mathbf{x} = \begin{bmatrix} \vec{x}_g \\ \vec{\theta} \\ \begin{pmatrix} \theta_r \\ \theta_g \end{pmatrix} \text{ or } \left(\theta_r - \frac{1}{N_{GR}}\theta_g\right) \\ \dot{\vec{x}}_g \\ \dot{\vec{\theta}} \\ \omega_r \\ \omega_g \end{bmatrix}. \tag{3.3}$$

3.2.3 Control Inputs

Only three inputs are considered for this model, which are collective blade pitch angle β $[deg]$, generator torque, T_g $[Nm]$, and nacelle yaw angle γ $[deg]$.

Each blade rotates about an axis that travels through its long dimension. When all blades rotate together, we call the unified angle the collective blade pitch angle β. Individual blade-pitch-actuation, on the other hand, has been shown to be quite effective for control of floating wind turbines [5, 17] and is possible using our model. However, doing so introduces periodic effects which must be dealt with using advanced control techniques. For simplicity, we will only present collective blade pitch control in this thesis. Our simplified model neglects actuator dynamics for this rotation, which results in the unrealistic ability to instantaneously change the angle. We can prevent such unrealistic motions in the non-linear model by limiting the rate at which this angle is allowed to move. Furthermore, we must ensure that designed controllers obey this limit.

Generator torque T_g can be controlled via the electric current applied to the generator. This allows for the manipulation of instantaneous power extraction, as well as the the control of equilibrium rotor speed.

Nacelle yaw angle is the angle between the unit vectors $\hat{e}_1^n$ and $\hat{e}_1^b$, in the body frame. As in the blade pitch case, we ignore actuator dynamics. Again, we can prevent unrealistic rotations in the non-linear model by limiting the

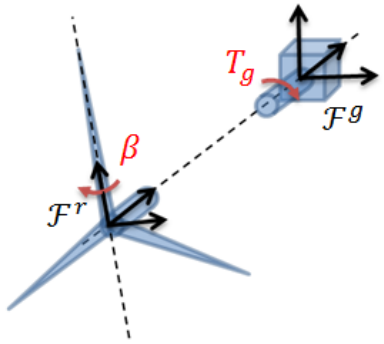

Figure 3.4: Blade Pitch Angle and Generator Torque Inputs.

rate at which this angle is allowed to change. As with the blade pitch rate, we must ensure that any designed controllers obey this limit.

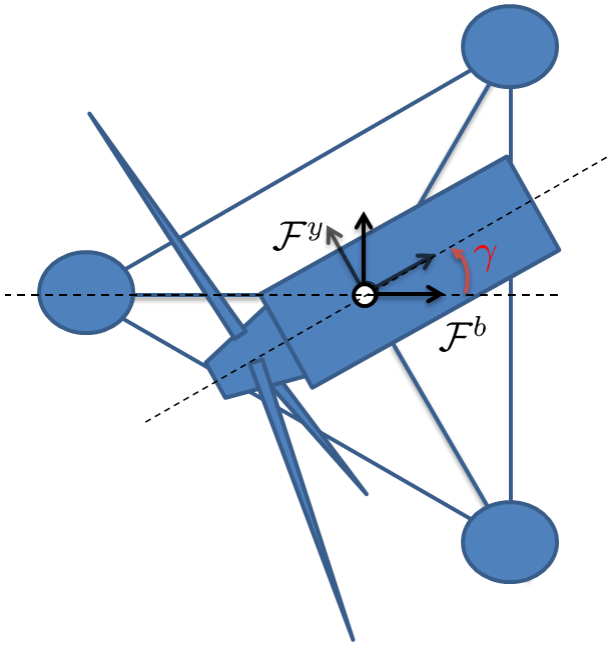

Figure 3.5: Yaw Angle Control Input.

Thus, the input vector of the WTS can be written as followed:

$$\mathbf{u} = \begin{bmatrix} \beta \\ T_g \\ \gamma \end{bmatrix} \tag{3.4}$$

.

3.2.4 Disturbances

The wind disturbance is simplified as the point wind velocity vector relative to the world frame, located at the center of thrust of the rotor. Thus, it can be written as:

$$\mathbf{v} = \begin{bmatrix} v_x \\ v_y \\ v_z \end{bmatrix} [m/s] \tag{3.5}$$

.

The wave disturbance can be simplified as a collection of n wave velocity vectors $\vec{w}_{v,1} \dots \vec{w}_{v,n} - [m/s]$, n wave acceleration vectors $\vec{w}_{a,1} \dots \vec{w}_{a,n} - [m/s^2]$, n wave heights $w_{h,n} \dots w_{h,n} - [m]$ and n dynamic pressure terms $w_{p,n} \dots w_{p,n} - [Pa]$, all relative to the world frame. The number of such terms is highly dependent on the geometry of the platform, and will be discussed in more detail in Section 3.3.1. For now, let us write the wave disturbance vector as:

$$\mathbf{w} = \begin{bmatrix} \vec{w}_{v,1} \dots \vec{w}_{v,n}, \vec{w}_{a,1} \dots \vec{w}_{a,n}, w_{h,n} \dots w_{h,n}, w_{p,n} \dots w_{p,n} \end{bmatrix}^T \tag{3.6}$$

.

3.2.5 Equations of Motion

With the states $\mathbf{x}$, control inputs $\mathbf{u}$ and disturbances $\mathbf{v}$ and $\mathbf{w}$ identified, we can return to (3.1) and derive the equations of motion. The non-linear

function f can be written as

$$f(\mathbf{x},\mathbf{u},\mathbf{v},\mathbf{w}) = \begin{bmatrix} \begin{pmatrix} \dot{\vec{x}}_g \\ \dot{\vec{\theta}} \\ \begin{pmatrix} \omega_r \\ \omega_g \end{pmatrix} \text{ or } \left(\omega_r - \frac{1}{N_{GR}}\omega_g\right) \end{pmatrix} \\ \vec{f}_F(\mathbf{x},\mathbf{u},\mathbf{v},\mathbf{w}) \\ \vec{f}_T(\mathbf{x},\mathbf{u},\mathbf{v},\mathbf{w}) \\ f_Q(\mathbf{x},\mathbf{u},\mathbf{v}) \end{bmatrix}, \tag{3.7}$$

where $\vec{f}_F - [m/s^2]$, $\vec{f}_T - [rad/s^2]$, and $f_Q - [rad/s^2]$ are obtained from the force, torque and shaft torque models, respectively.

The force model is a summation of all relevant forces that act on the wind turbine system and takes the form

$$\vec{f}_F(\mathbf{x},\mathbf{u},\mathbf{v},\mathbf{w}) = (m_g \underline{\mathrm{I}}_{3x3} + \mathrm{diag}[\vec{m}_a])^{-1} \sum_j \vec{F}_j(\mathbf{x},\mathbf{u},\mathbf{v},\mathbf{w}), \tag{3.8}$$

where m_g is the total mass of the turbine platform, $\underline{\mathrm{I}}_{3x3}$ is a $3x3$ identity matrix, and $\vec{m}_a$ is the hydrodynamic added mass vector, which is described in Section 3.3.1. The summation of forces $\vec{F}_j$ contains all the relevant forces on the system such as aerodynamic forces $\vec{F}_A$, buoyancy forces $\vec{F}_B$, catenary forces $\vec{F}_C$, and hydrodynamic forces $\vec{F}_D$, as depicted in Figure 3.6. These forces are described in detail in Section 3.3. Forces can easily be added, modified or dropped from the summation for each specific wind turbine system.

Like its force counterpart, the torque model is a summation of all the relevant torques acting on the wind turbine about its center of gravity. This takes the form

$$\vec{f}_T(\mathbf{x},\mathbf{u},\mathbf{v},\mathbf{w}) = (\underline{\mathrm{R}}\underline{\mathrm{I}}_g^{-1}\underline{\mathrm{R}}^T) \sum_j \vec{T}_j(\mathbf{x},\mathbf{u},\mathbf{v},\mathbf{w}). \tag{3.9}$$

Here, $\underline{\mathrm{I}}_g$ is the inertia tensor of the wind turbine in its upright orientation, $\underline{\mathrm{R}}$ is the rotation matrix that represents the orientation of the wind turbine

with respect to the fixed world frame, and the summation of torques $\vec{T}_j$ contains all the torques on the system. Most torques take the form

$$\vec{T}_j(\mathbf{x}, \mathbf{u}, \mathbf{v}, \mathbf{w}) = \underline{\mathrm{R}}\vec{r}_{gj} \times \vec{F}_j(\mathbf{x}, \mathbf{u}, \mathbf{v}, \mathbf{w}), \tag{3.10}$$

where $\vec{r}_{gj}$ is the position vector from the turbine center of gravity to the location of the corresponding force in the fixed body frame. Finally, the rotor torque model is given by the torque balance

$$f_Q(\mathbf{x}, \mathbf{u}, \mathbf{v}) = \begin{bmatrix} \sum_{k_r} \frac{1}{J_r} Q_{k_r}(\mathbf{x}, \mathbf{u}, \mathbf{v}) \\ \sum_{k_g} \frac{1}{J_g} Q_{k_g}(\mathbf{x}, \mathbf{u}, \mathbf{v}) \end{bmatrix}, \tag{3.11}$$

where J_r and J_g represent the inertia about the rotor-side shaft and generator-side shaft, respectively, and Q_{k_r} and Q_{k_g} represent the ${k_r}^{th}$ and ${k_g}^{th}$ torque about each respective shaft.

So far, we described the structure of the proposed simplified model for a general floating wind turbine system. Depending on the turbine type, mooring type, and platform type, the forces and torques that make up the force and torque models, and the locations of the forces may be different. In the next section, we derive the force and torque models for the baseline 5MW semi-submersible wind turbine. We then validate it using simulation software FAST in Section 3.5.

3.3 Forces and Torques for the Baseline Turbine

This section describes the force and torque models used to construct the example 5-MW semi-submersible wind turbine [1, 18]. Forces are depicted in Figure 3.6 and include the the aerodynamic force $\vec{F}_A$, buoyancy force $\vec{F}_B$, catenary line forces $\vec{F}_C$ and hydrodynamic drag/inertial force $\vec{F}_D$. For each of these forces, there is an accompanying torque ($\vec{T}_A$, $\vec{T}_B$, $\vec{T}_C$ and $\vec{T}_D$), however these are not shown for clarity. The rotor torque T_r, however, which is a part of the shaft model and does not directly affect the wind turbine

system, but instead acts directly on the rotor is also shown in the diagram.

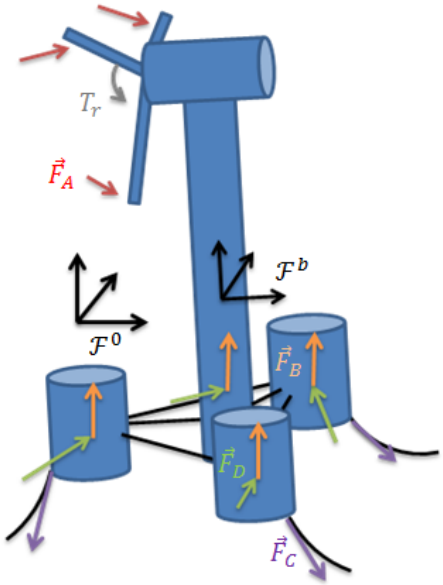

Figure 3.6: Overall Force Diagram of the Non-Linear Model.

3.3.1 Hydrodynamics

The hydrodynamic model includes all forces related to the interaction between the platform and the surrounding water. These forces act continuously and unevenly over the submerged surface area of the platform, making it extremely difficult to integrate them analytically. Instead, we can split the platform up into small cylinders, inside which we assume that the variables affecting the hydrodynamic forces are constant. We can then apply to each cylinder Archimedes' principle to determine the buoyancy force, and Morison's equation to obtain the drag and inertial forces. For the semi-submersible platform, we can achieve good results by considering three cylinders for each column. These are shown graphically in Figure 3.7. Here, only the four top-most cylinders are partially submerged, and thus their submerged lengths change. The rest always remain fully submerged.

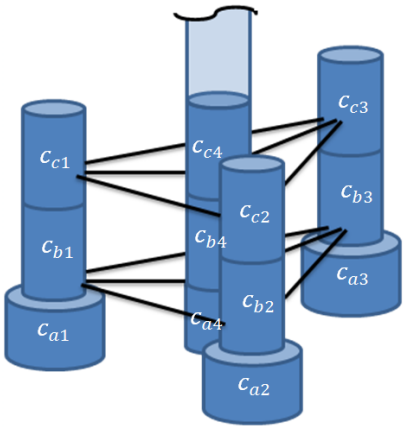

Figure 3.7: Separated Cylinder Segments.

Buoyancy Archimedes' principle states that the buoyancy force on an object is equal to the weight of fluid that it displaces [32]. A depiction of the buoyancy model is given in Figure 3.8. Here, $\vec{x}_g$ and $\vec{x}_i$ represent the wind turbine center of mass and the cylinder center of volume in the world frame, respectively. The force on a submerged cylinder i is given by

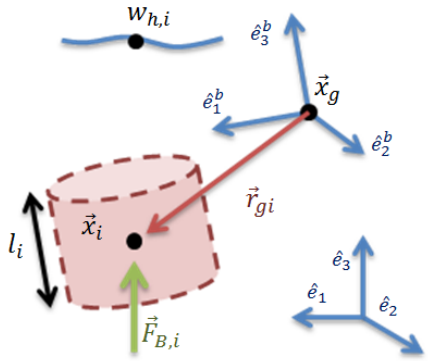

Figure 3.8: Buoyancy Force Diagram.

$$\vec{F}_{B,i}(\mathbf{x}) = \rho_w g A_i l_i \hat{e}_3, \tag{3.12}$$

where ρ is the density of the fluid, g is the gravitational constant, and A_i and l_i are the cross sectional area and length of the cylinder, respectively. For the top-most cylinders, the length will change based on platform position and orientation. This relationship can be approximated by the expression:

$$l_i(\vec{x}_g, \vec{\theta}) = \frac{l_{0,i}}{2} - w_{h,i} - \begin{bmatrix} \theta_y & \theta_x & 1 \end{bmatrix} \vec{r}^{\,\flat}_{gi,0} \tag{3.13}$$

where $\vec{r}^{\,\flat}_{gi,0}$ is the constant vector that points from the center of gravity of the wind turbine to the initial center of volume of the cylinder, given in the body-fixed frame. Note that we do not include changes in water level due to waves or other factors in this expression. Instead, we deal with the resulting effects from wave height via dynamic pressure which is considered in the drag and inertial forces.

Given the force on the cylinder, the torque that it transmits to the wind turbine is given by

$$\vec{T}_{B,i}(\mathbf{x}) = \underline{\mathrm{R}}\vec{r}^{\,\flat}_{gi} \times \vec{F}_{B,i}, \tag{3.14}$$

where $\vec{r}^{\,\flat}_{gi}$ is the vector that points from the center of gravity of the WTS to the center of volume of the cylinder, in the body frame. For all but the top-most cylinders, this vector is equivalent to $\vec{r}^{\,\flat}_{gi,0}$. For the top-most cylinders, the location of the force changes with platform position, and can be expressed as

$$\vec{r}^{\,\flat}_{gi} = \vec{r}^{\,\flat}_{gi,0} + \begin{bmatrix} 0 & 0 & 1 \end{bmatrix}^T \left(\frac{l_i - l_{i,0}}{2} \right). \tag{3.15}$$

Lastly, we must include the force of gravity acting at the center of gravity of the wind turbine system, and given by

$$\vec{F}_G = -m_g g \hat{e}_3^0. \tag{3.16}$$

This does not produce a torque on the WTS because it is acting at the center of gravity, and thus the cross product is zero. Finally, the total buoyancy

force is give by

$$\vec{F}_B(\mathbf{x}) = \sum_i \vec{F}_{B,i} + \vec{F}_G, \tag{3.17}$$

and the torque by

$$\vec{T}_B(\mathbf{x}) = \sum_i \vec{T}_{B,i}. \tag{3.18}$$

Drag and Inertial Forces Drag is the dissipative force that resists relative motion between a body and a fluid. A depiction of the force model is given in Figure 3.9. For a submerged cylinder in transverse flow, Morison's equation gives a simple approximation for the drag force on the cylinder face in the relative direction of flow [1]. For the 3-D case, this force can be realized using the following equation:

$$\vec{F}_{Dt,i}(\mathbf{x}, \mathbf{w}) = K_{d,i}||\vec{v}_{t,i}||\vec{v}_{t,i} + K_{a,i}\vec{a}_{t,i}, \tag{3.19}$$

where the drag and inertia constants $K_{d,i}$ and $K_{a,i}$ are the constants from Morison's equation, and $\vec{v}_{t,i}$ and $\vec{a}_{t,i}$ are the equivalent transverse velocity and acceleration vectors for the calculation. The transverse velocity and acceleration vectors can be calculated via the series of transformations

$$\vec{v}_t = \underline{\mathrm{R}} \begin{bmatrix} 1 & & \\ & 1 & \\ & & 0 \end{bmatrix} \underline{\mathrm{R}}^T \vec{w}_{rel}, \tag{3.20}$$

$$\vec{a}_t = \underline{\mathrm{R}} \begin{bmatrix} 1 & & \\ & 1 & \\ & & 0 \end{bmatrix} \underline{\mathrm{R}}^T \dot{\vec{w}}_{rel}, \tag{3.21}$$

and the magnitude of the transverse velocity can be simplified to

$$||\vec{v}_t|| = \left(\vec{w}_{rel}^T \underline{\mathrm{R}} \begin{bmatrix} 1 & & \\ & 1 & \\ & & 0 \end{bmatrix} \underline{\mathrm{R}}^T \vec{w}_{rel} \right)^{\frac{1}{2}}. \tag{3.22}$$

In the previous three equations, the relative wave velocity, $\vec{w}_{rel}$, and its time derivative $\dot{\vec{w}}_{rel}$ are given by

$$\vec{w}_{rel} = \vec{w} - \dot{\vec{x}}_g - \dot{\underline{\mathrm{R}}}\vec{r}^{b}_{gi} \tag{3.23}$$

$$\dot{\vec{w}}_{rel} = \dot{\vec{w}}. \tag{3.24}$$

Here, $\vec{w}$ is the undisturbed wave velocity at the center of volume of the cylinder. Note that the inertial force due to the platform's acceleration has not been included here as it is included in the overall force model in the form of added mass.

For the bottom-most cylinders, there is also a drag force and inertial force in the heave direction. This force is described in 1-D in [1], and can be extended to 3-D with the following equation:

$$\vec{F}_{Dh,i}(\mathbf{x}, \mathbf{w}) = K_{dh,i}||\vec{v}_{h,i}||\vec{v}_{h,i} + K_{ah,i}\vec{a}_{h,i} + P_i A_i \hat{e}_h, \tag{3.25}$$

Again, $K_{dh,i}$ and $K_{ah,i}$ are the constants from the heave plate equation in [1], and $\vec{v}_{h,i}$ and $\vec{a}_{h,i}$ are the equivalent heave velocity and acceleration vectors for the calculation. These vectors can be calculated via a similar series of transformations as for the transverse case, but with a different projection matrix. This is shown for the heave velocity calculation below:

$$\vec{v}_h = \underline{\mathrm{R}} \begin{bmatrix} 0 & & \\ & 0 & \\ & & 1 \end{bmatrix} \underline{\mathrm{R}}^T \vec{w}_{rel}. \tag{3.26}$$

Finally, we write the total drag and inertia force on each cylinder as

$$\vec{F}_{D,i}(\mathbf{x}, \mathbf{w}) = \vec{F}_{Dt,i} + \vec{F}_{Dh,i}. \tag{3.27}$$

Again, the induced torques on the wind turbine are given by crossing the vector travelling from the turbine center of mass to the cylinder center of volume with the forces at the cylinder center. Then the torque can be

written as

$$\vec{T}_{D,i}(\mathbf{x}, \mathbf{w}) = \underline{\mathrm{R}}\vec{r}^{\,b}_{gi} \times \vec{F}_{D,i}. \tag{3.28}$$

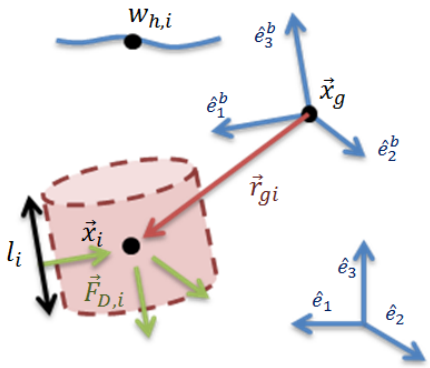

Figure 3.9: Drag and Inertial Force Diagram.

Added Mass Added mass is the effective mass increase experienced by a submerged body in motion due to the liquid that accelerates with the object. In the proposed model, we assume that this is constant in the body frame (i.e., it does not get recomputed as the lengths of the submerged cylinders change). Added mass is calculated as it appears in Morison's equation for each cylindrical face exposed to the water. For the lateral and bottom faces, the added mass is given respectively by $m_{a,i} = K_{a,i}$ and $m_{a,i} = K_{az,i}$. The total added mass then is given by the sum of all these parts, or:

$$\vec{m}_a = \sum_i \underline{\mathrm{R}} \begin{bmatrix} K_{a,i} \\ K_{a,i} \\ K_{az,i} \end{bmatrix}. \tag{3.29}$$

Inertia is also affected by this effect, however because the inertia tensor is defined in the body frame, it remains constant, even in platform rotations. Therefore, the modified inertia tensor we use in our model represents both the physical inertia of the system, as well as the additional inertia from added mass.

3.3.2 Aerodynamics

The aerodynamic model is concerned with the interaction between the wind and the turbine. This includes the forces acting on the blades and the resulting power transferred to the rotor. In the proposed model, a separate thrust and drag force is calculated for each blade in order to accurately predict individual blade pitch actuation.

Thrust and Drag The thrust force is the wind force in a direction parallel to the rotation axis of the rotor, whereas the drag force is the wind force in the direction of motion of a point on the blade. In reality, these forces act continuously over the entire blade; however, for simplicity, we localize the net thrust force for all three blades at a location we call the center of thrust. A depiction of the thrust and drag forces is given in Figure 3.11. The net

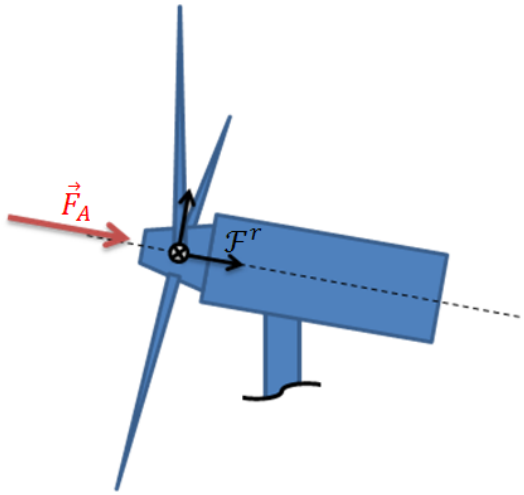

Figure 3.10: Aerodynamic Force Diagram.

thrust force vector for is given by the relationship

$$\vec{F}_A(\mathbf{x}, \mathbf{u}, \mathbf{v}) = \frac{1}{2}\rho A_r C_t(\lambda, \beta)||\vec{v}_n||\vec{v}_n, \tag{3.30}$$

where C_t is the thrust coefficient which is a function of the tip-speed-ratio (TSR) λ, and the blade pitch angle β [33]. Parameters ρ and A_r represent the air density and the swept area of the rotor, respectively. The equivalent velocity vector normal to the face of the rotor blades, $\vec{v}_n$, can be calculated by

$$\vec{v}_n = \underline{\mathrm{R}}_{eq} \begin{bmatrix} 1 & & \\ & 0 & \\ & & 0 \end{bmatrix} \underline{\mathrm{R}}_{eq}^T \vec{v}_{rel}, \tag{3.31}$$

and the magnitude simplified to

$$||\vec{v}_n|| = \begin{bmatrix} 1 & 0 & 0 \end{bmatrix} \underline{\mathrm{R}}_{eq}^T \vec{v}_{rel} \tag{3.32}$$

where

$$\underline{\mathrm{R}}_{eq} = \underline{\mathrm{R}}_y(\theta_{tilt}) \underline{\mathrm{R}}_z(\gamma) \underline{\mathrm{R}}. \tag{3.33}$$

The last inclusion is the gyroscopic torque that is transferred to the platform when we utilize the generator torque input to accelerate or decelerate the rotor. The magnitude of this torque is simply the product of the generator torque and the gear ratio, and thus the total aerodynamic torque can then be written as

$$\vec{T}_A(\mathbf{x}, \mathbf{u}, \mathbf{v}) = (\underline{\mathrm{R}} \vec{r}_{gt}^{\,b} \times \vec{F}_A) + \underline{\mathrm{R}}_{eq} N_{GR} T_g \hat{e}_1, \tag{3.34}$$

where N_{GR} is the gear ratio between the two shafts.

Power Finally, the aerodynamic power is given by

$$P = \frac{1}{2} \rho A_r C_p(\lambda, \beta) ||\vec{v}_n||^3. \tag{3.35}$$

The torque balance about the rotor shaft and generator shaft are then given by

$$\dot{\vec{\omega}}_r = \frac{1}{J_r} \left(\frac{P}{\omega_r} - k \left(\theta_r - \frac{1}{N_{GR}} \theta_g \right) - b \left(\omega_r - \frac{1}{N_{GR}} \omega_g \right) \right), \tag{3.36}$$

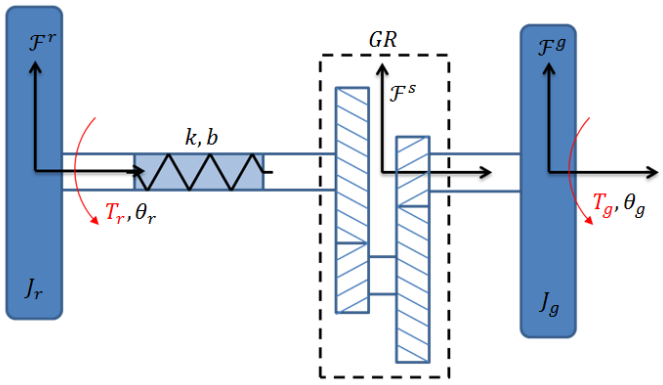

Figure 3.11: Rotor-Generator Shaft Torque Diagram.

and

$$\dot{\vec{\omega}}_g = \frac{1}{J_g}\left(-T_g + \frac{k}{N_{GR}}\left(\theta_r - \frac{1}{N_{GR}}\theta_g\right) + \frac{b}{N_{GR}}\left(\omega_r - \frac{1}{N_{GR}}\omega_g\right)\right), \quad (3.37)$$

respectively. Finally, we can write the shaft torque model f_Q from Section 3.2 as

$$f_Q = \begin{bmatrix} \dot{\vec{\omega}}_r \\ \dot{\vec{\omega}}_g \end{bmatrix}. \quad (3.38)$$

Gyroscopic Effect Because we consider the entire WTS as a single rigid body, we are neglecting the gyroscopic effect that results from the rotor frame rotating with respect to the world frame. It turns out that for the semi-submersible platform, this effect is negligible, and for simplicity it is not included in the proposed model. However, for platforms with less inertia, this may not be the case. For these platforms, we can account for the gyroscopic torque on the WTS by enforcing the conservation of angular momentum about the entire system. That is, when the angular momentum of the shaft changes, the angular momentum of the platform must change in an equal and opposite way. We can quantify this effect by considering the

rate of change of the angular momentum of the rotor

$$\frac{d\vec{H}_r}{dt} = \frac{d}{dt}\left(\underline{\mathrm{R}}_{eq}\begin{bmatrix} J_r\omega_r \\ 0 \\ 0 \end{bmatrix}\right), \tag{3.39}$$

where $\vec{H}_r$ is the angular momentum of the rotor. This can be further simplified to

$$\underline{\mathrm{R}}_{tilt}\left(\dot{\underline{\mathrm{R}}}_{\gamma}\underline{\mathrm{R}} + \underline{\mathrm{R}}_{\gamma}\dot{\underline{\mathrm{R}}}\right)\begin{bmatrix} J_r\omega_r \\ 0 \\ 0 \end{bmatrix} + \underline{\mathrm{R}}_{tilt}\underline{\mathrm{R}}_{\gamma}\underline{\mathrm{R}}\begin{bmatrix} J_r\dot{\omega}_r \\ 0 \\ 0 \end{bmatrix}. \tag{3.40}$$

The left-most term represents the change in angular momentum of the shaft as the shaft frame rotates in the world frame, and the right-most term represents the change in angular momentum of the shaft due to acceleration in its own frame, which has already been accounted for in 3.3.2. The gyroscopic torque, then, is an equal and opposite torque to the left-most term in (3.40), or.

$$\vec{T}_{gyro} = -\underline{\mathrm{R}}_{tilt}\left(\dot{\underline{\mathrm{R}}}_{\gamma}\underline{\mathrm{R}} + \underline{\mathrm{R}}_{\gamma}\dot{\underline{\mathrm{R}}}\right)\begin{bmatrix} J_r\omega_r \\ 0 \\ 0 \end{bmatrix}. \tag{3.41}$$

Relative Tip-Speed Effect The wind power and thrust models used in the proposed model assume that the wind travels in a direction perpendicular to the rotation path of the blades. In reality, this is not the case, and when the wind vector is not aligned in such a fashion, there will be azimuth-dependent changes in the aerodynamic force for each blade as it moves relative to the wind vector. In [34], the authors accounted for this by considering an aerodynamic force at the midpoint of each blade, instead of at a single location. This adds periodicity to the model, which makes linearization at static operating points not possible. As it turns out, however, the complexity of adding this effect does not provide a substantial increase in overall accuracy of the major dynamics of the semi-submersible system.

The effect is more important for vibrational analysis of the blades.

3.3.3 Mooring Line

The mooring system consists of a series of cables attaching the wind turbine to the sea bed. These cables provide a restoring force in response to platform displacements caused by wind, waves and other disturbances. The quasi-static model for a single cable in 2-D is described in [35] and consists of two coupled, non-linear equations that relate horizontal and vertical distance between cable ends with the 2-D force at the wind turbine attachment point. It is important to note that these equations change depending on whether a portion of the line rests on the sea bed, or whether it is fully ungrounded. For simplicity, we will only consider the former case. This follows the assumption that the wind turbine does not move a large distance from its equilibrium position. A depiction of the catenary force model is shown in Figure 3.12.

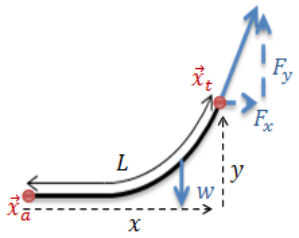

Figure 3.12: 2-D Catenary Line Model

By using a multi-dimensional Newton-Raphson iteration, the unique 2-D forces $F_x(x, y)$ and $F_y(x, y)$ are determined for a range of relevant values of x and y. If we define $\vec{x}_{t,i}$ as the total 3-D distance vector between the anchor point of the i'th mooring line and the i'th attachment point on the turbine, then x is the magnitude of the projection of $\vec{x}_{t,i}$ on the x-y plane. Similarly, y is the projection of $\vec{x}_{t,i}$ on the z-axis. Vector $\vec{x}_{t,i}$ then is given by

$$\vec{x}_{t,i} = \vec{x}_{a,i} - \vec{x}_g - \underline{\mathrm{R}}\vec{r}^{\,b}_{gci}, \tag{3.42}$$

where $\vec{r}_{gci}$ is the distance vector between the turbine center of gravity and

the attachment point in the BF. Finally, the total catenary force at the attachment point of mooring line i is given by

$$\vec{F}_{C,i}(\mathbf{x}) = \begin{pmatrix} F_x(\vec{x}_{t,i})||\text{proj}_{\hat{e}_1}(\vec{x}_{t,i})||, \\ F_x(\vec{x}_{t,i})||\text{proj}_{\hat{e}_2}(\vec{x}_{t,i})|| \\ F_y(\vec{x}_{t,i}) \end{pmatrix}, \tag{3.43}$$

It follows that the total force and torque are given by

$$\vec{F}_C(\mathbf{x}) = \sum_i \vec{F}_{C,i}(\mathbf{x}) \tag{3.44}$$

$$\vec{T}_C(\mathbf{x}) = \sum_i \left(\underline{\mathrm{R}} \vec{r}^{\,b}_{gci} \times \vec{F}_{C,i} \right), \tag{3.45}$$

respectively.

3.4 Parameter Identification

All of the parameters used in the non-linear model are listed in Appendix A. The majority of said parameters, such as the inertial and geometric information for the WTS structure and platform, and for the flexibility information for the shaft, were found in [18] and [1]. Some parameters, however, had to be collected from FAST simulations. These include the C_p and C_t curves, the modified inertia tensor, and small tunings to the drag constants. The process of obtaining this additional information is explained in this section.

3.4.1 C_p and C_t Curves

The power and thrust curves are a function of blade-pitch angle, β, and TSR, λ, which is the ratio of blade tip speed and normal wind velocity, or

$$\lambda = \frac{\omega_r r}{v} \tag{3.46}$$

The Cp and Ct surfaces were obtained by running a series of FAST simulations ($i = 1 : n$) under the following conditions:

- All DOFs disabled except aerodynamic force
- Rotor shaft tilt brought down to 0°
- Perfectly horizontal wind speed that steps by Δv every T seconds
- Constant rotor speed ω_i
- Sinusoidal blade pitch angle with half period equal to T

The time series information for the simulation input conditions is shown in Figure 3.13. Following the simulations, the C_p and C_t values were extracted from the simulation data at one hundred equally spaced values of ω_r and v and the surfaces, shown in Figure 3.14 were created.

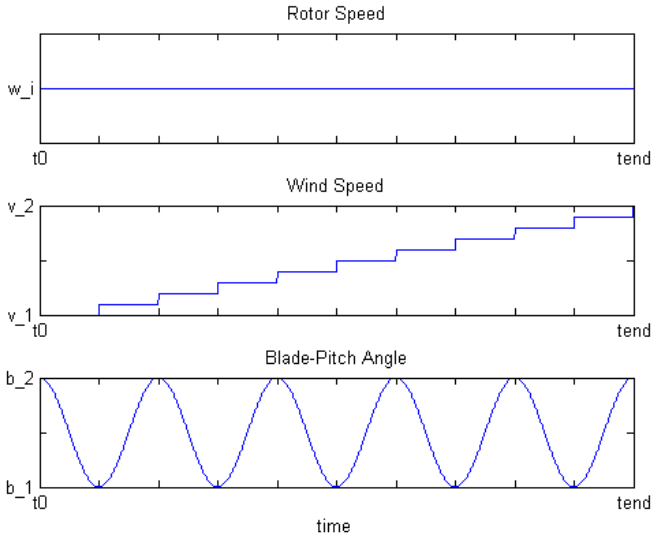

Figure 3.13: Simulation Conditions for Obtaining C_p and C_t Surfaces.

3.4.2 Added Inertia and Drag Constants

Both the added inertia and the drag constants were found by tuning the platform natural frequencies and damping characteristics in a test similar to

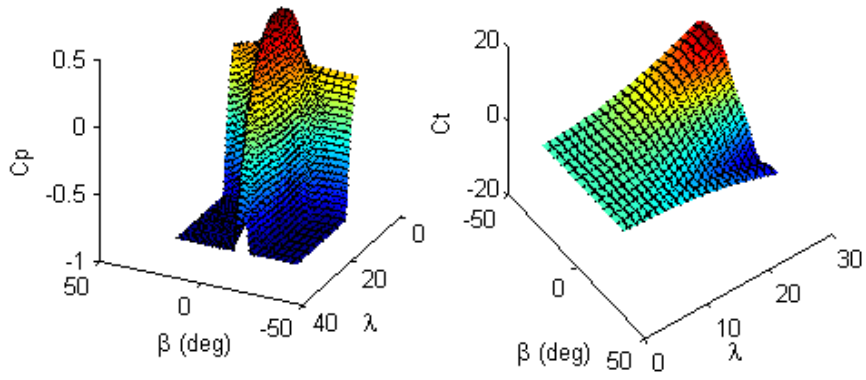

Figure 3.14: C_p and C_t Surfaces.

the perturbation test, described in Section 3.5.1. The resulting values are given in Appendix A

3.5 Validation of Non-Linear Model

In order to validate the model derived for the Baseline 5MW wind turbine, several tests were performed targeting specific effects of the non-linear model both in isolation and all together. First, a series of simple 2-D perturbation tests were performed to examine the inertial-elastic response of the WTS to initial displacements of the states. Next, a series of tests were performed to analyze the effect of wind disturbance at various WTS operating conditions. Following these tests without wave excitation, a simple wave test was performed to analyze the hydrodynamic response of the WTS and the effect of wave disturbances. Finally, an overall realistic open-loop response test was performed to validate the WTS under realistic wind, wave and control input

trajectories.

3.5.1 Perturbation Test

As a means to validate the inertial and elastic response of the non-linear model to perturbations in platform position, the perturbation response test was conducted. In this test, the platform was given an initial displacement in each of the six DOFs under no wind or wave disturbance, and the time series responses were collected. The responses are shown for both the non-linear model and for FAST in Figure 3.15.

To quantify the test results, the RMS errors between the time series of FAST and the proposed non-linear model were calculated, as well as the major oscillation frequency differences between them. It should be noted that the rotor and generator speed degrees of freedom were excluded from the simulation. The results are shown in Table 3.1, with initial displacements in parentheses.

Table 3.1: Perturbation Response Results

Direction	RMS error	Frequency error
Surge (9m)	0.48m	0.93%
Sway (9m)	0.45m	1.97%
Heave (9m)	0.20m	3.19%
Roll (9°)	0.34°	2.34%
Pitch (9°)	0.35°	1.85%
Yaw (9°)	0.536°	2.57%

With all the translational RMS errors less than 0.5m and the rotational RMS errors less than 0.6 degrees, the undisturbed inertial-elastic response of the WTS is clearly very close to that of FAST. Furthermore, all the major natural frequencies of the WTS are within 3.2% of those measured in FAST, which effectively validates the mooring line and buoyancy models, and the inertial properties of the wind turbine system over a large operating range ($10m$ in translational displacement and $10deg$ in rotational displacement is larger than we would expect to see in typical operation).

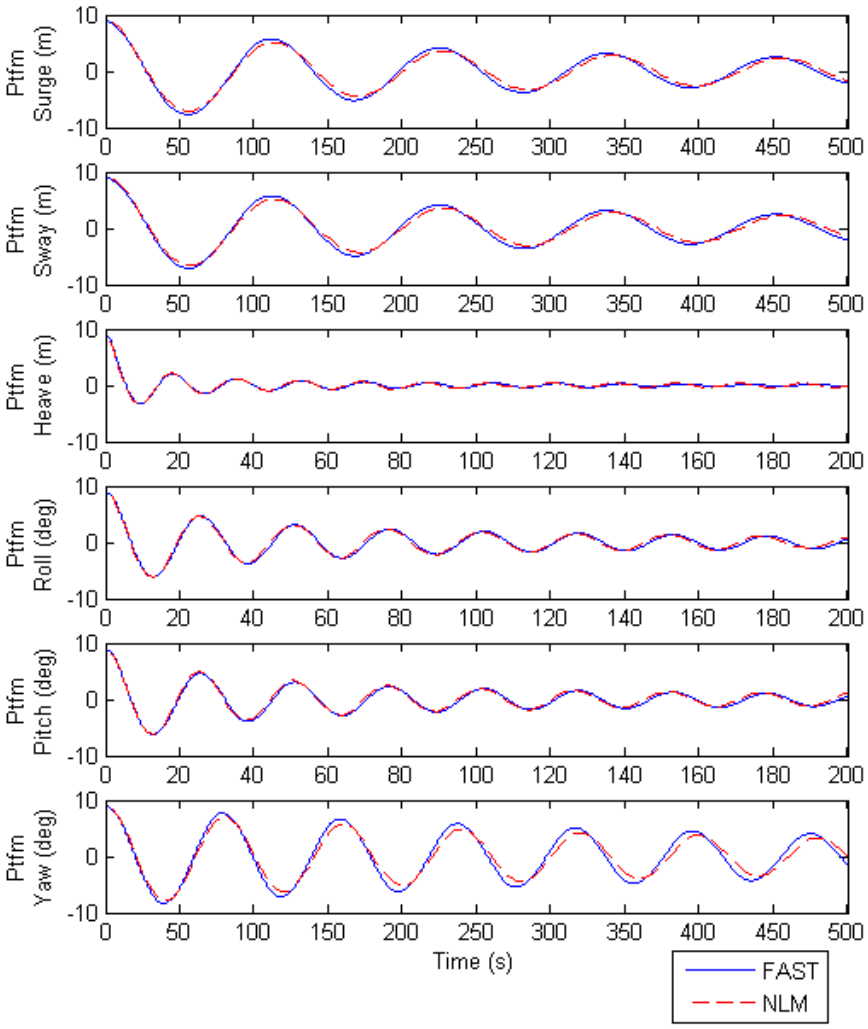

Figure 3.15: Perturbation Test Results.

3.5.2 Gust Test

Next, we consider the effect of wind disturbance. As a means to validate the effect of wind disturbance on the WTS model, several tests involving the instantaneous application of wind were performed. Because the aerodynamic

forces are a function of both the wind disturbance, and the rotor speed, the test was run at various tip-speed-ratios and wind speeds. However, to exclude the effects of rotor shaft dynamics, the rotor speed was held fixed for the duration of each test. Blade pitch angle was also fixed at zero degrees. Again, the time series response data was collected in FAST and the proposed model, which is illustrated in Figure 3.16 for the affected states.

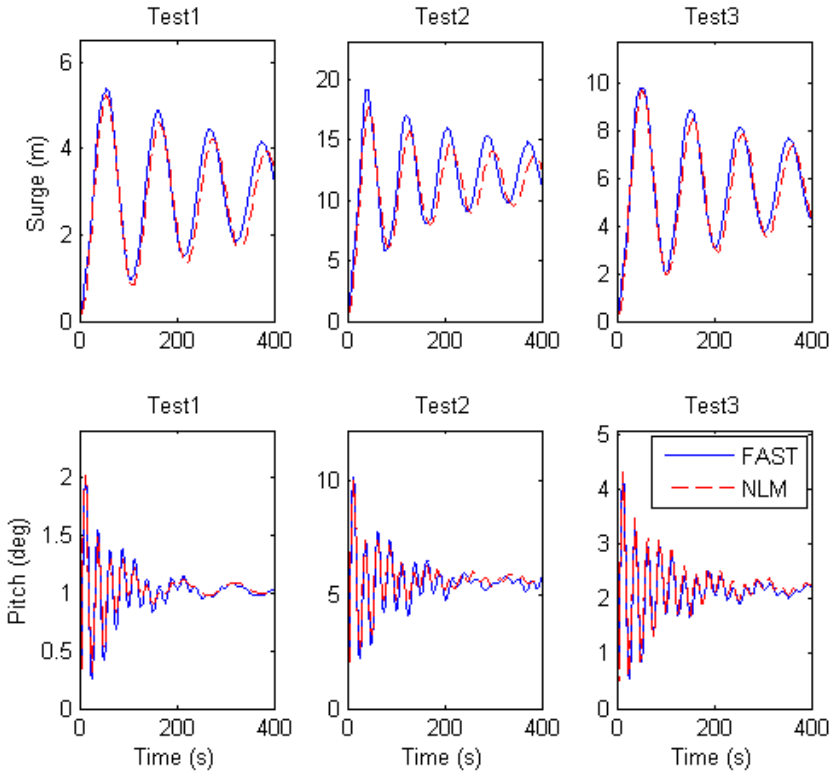

Figure 3.16: Wind Gust Test Results

RMS errors were calculated for the affected states, as shown in Table 3.2. The average state values over the course of the simulation are also given in the table as a reference point for the RMS error.

Once again, the RMS values for the non-linear model compared to FAST

Table 3.2: Aerodynamic Response Results

TSR	Wind Speed	Surge RMS	Pitch RMS
1.32	25m/s	0.51m (average 5.64m)	0.11° (average 1.10°)
5.05	17m/s	1.46m (average 11.75m)	0.33° (average 2.80°)
17.15	5m/s	0.33m (average 2.95m)	0.05° (average 0.52°)

are very similar over a wide operating range. For both translation and rotation, the RMS error is at the highest 12.4% of the average, and even that is likely caused by a small difference in the steady state value of the two curves. Once again we consider this test a success, which effectively validates the aerodynamic force model and effect of wind disturbance on the WTS.

3.5.3 Regular Wave Test

With the inertial-elastic, and aerodynamic responses validated, we turn to the effect of wave disturbance on the WTS. The next test looked at the platform response to wave disturbance. Unfortunately, due to the complexity of irregular waves, and their spatial and time dependence, the multi-frequency wave profile generated by FAST could not be duplicated for the non-linear model. Instead, a regular wave profile, or single frequency sinusoid profile was obtained using linear wave theory [36], using a wave elevation of 1.75 m and a single spectral period of 12 s. In linear wave theory, we assume the 3-D wave height in space and time is given by

$$h(\vec{x}_w, t, \alpha) = A\sin(\zeta(\vec{x}_w, t, \alpha)), \tag{3.47}$$

where A is the amplitude of the wave, t is time, α is the wave direction about the world frame z axis, $\vec{x}_w$ is the spatial location of the wave height,

and the space/time dependent parameter ζ_i is given by

$$\zeta(\vec{x}_w, t, \alpha) = \frac{-\omega^2}{g}\left(\hat{e}_1 \underline{\mathrm{R}}_z^T(\alpha)\vec{x}_w\right) + \omega t + \phi. \tag{3.48}$$

Here, ω represents the frequency of the wave, $\underline{\mathrm{R}}_z^T(\alpha)$ is the z-rotation of magnitude α, g is the gravitational constant, and ϕ is the phase angle. Unfortunately, as FAST only allows for the specification of period and amplitude, the phase parameter and direction of the spatial term had to be fitted. With the frequency, amplitude and phase known, we can calculate the remaining hydrodynamic disturbances as follows

$$\vec{v}(\vec{x}_w, t, \alpha) = \omega \exp\left(\frac{-\omega^2}{g} z\right) \begin{bmatrix} \cos(\alpha)\sin(\zeta) \\ \sin(\alpha)\sin(\zeta) \\ \cos(\zeta), \end{bmatrix} \tag{3.49}$$

$$\vec{a}(\vec{x}_w, t, \alpha) = \omega^2 \exp\left(\frac{-\omega^2}{g} z\right) \begin{bmatrix} \cos(\alpha)\cos(\zeta) \\ \cos(\alpha)\cos(\zeta) \\ -\sin(\zeta) \end{bmatrix}, \tag{3.50}$$

$$P_d(\vec{x}_w, t, \alpha) = \rho g \exp\left(\frac{-\omega^2}{g} z\right) \sin(\zeta), \tag{3.51}$$

where parameter z is given by

$$z = \hat{e}_3 \underline{\mathrm{R}}_z^T(\alpha)\vec{x}_w. \tag{3.52}$$

After collecting all the necessary parameters to recreate the FAST wave profile, an identical simulation was run using the WTS, and the responses for the relevant states are shown in Figure 3.17.

Once again, the time responses of FAST and the proposed model are very similar. The biggest discrepancy seems to be a slight difference in the damping, however it is minimal. At this point, we say that all the individual pieces of the non-linear model have been validated. However, it is important to validate not only each piece individually, but also the entire system as a whole, with realistic wind and wave disturbances, varying control inputs,

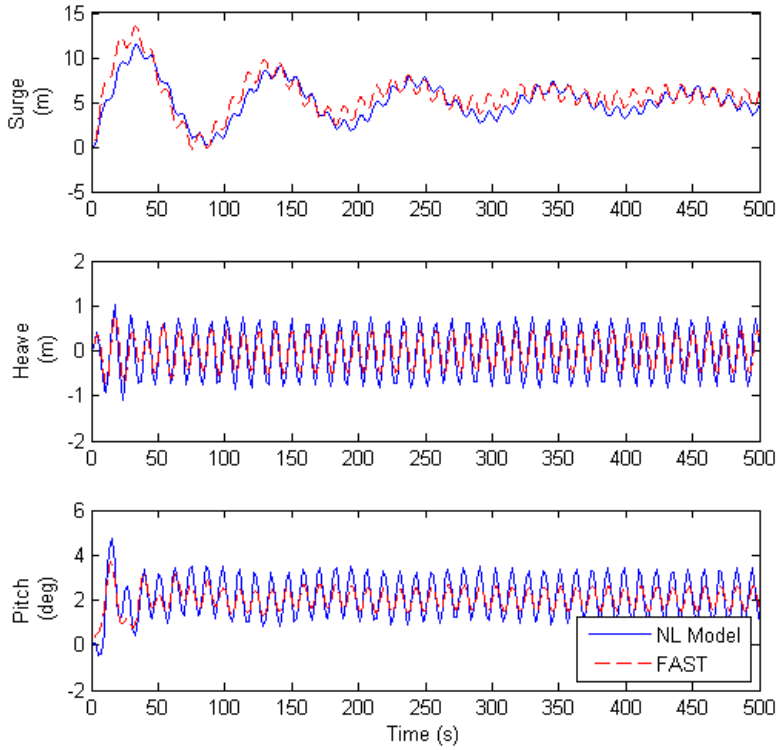

Figure 3.17: Time Response Comparison for the Regular Waves Test.

and varying states.

3.5.4 Realistic Open-Loop Test

The purpose of the realistic open test is to compare the time response of the non-linear model to the FAST model with all degrees of freedom activated, under realistic disturbance and control input. For the comparison, we first explain specific wind and wave disturbances that we employed in the test.

Disturbances The realistic wind disturbance profile was created by program TurbSim [37] with a mean wind speed of 18 m/s at a mean angle of 20° about the $\hat{e}_3$ axis, as shown in Figure 3.18. Using this program, we are able

to produce similar wind profiles for FAST, which is capable of using TurbSim output files, and the proposed model, which takes a single 3-D wind velocity vector. This wind vector is given relative to the world frame at a hub height of 90 m (the height of the center of thrust for the undisplaced WTS) and is shown in Figure 3.19. We make the assumption that this wind vector is always acting at the center of thrust of the WTS.

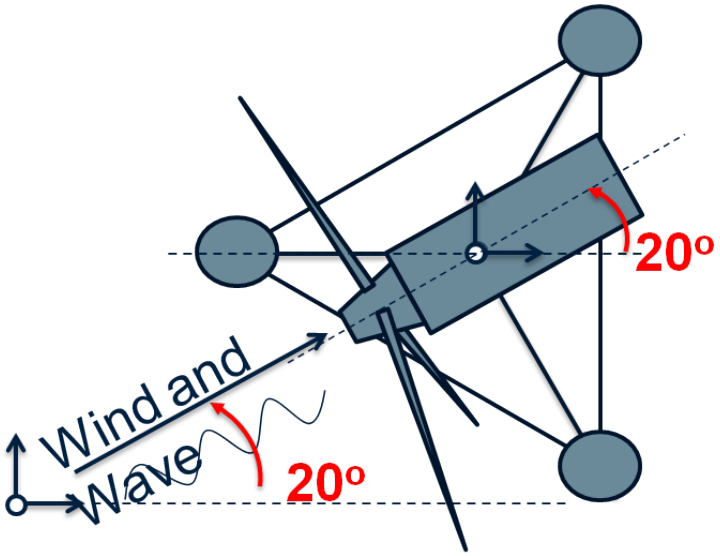

Figure 3.18: Overview of the Realistic Open-Loop Test Wind and Wave Disturbances.

Again, due to the limitation of collecting wave information in FAST, only a single frequency wave was used. The frequency and amplitude of the wave were determined by considering the Pierson-Moskowitz ocean wave spectrum [38]. This wave energy spectrum assumes a fully developed wave profile caused by steadily blowing wind over an infinitely long amount of time, and can be calculated by

$$S(\omega) = \frac{s_\alpha g^2}{\omega^5} \exp\left(s_\beta \left(\frac{\omega_0}{\omega}\right)^4\right), \tag{3.53}$$

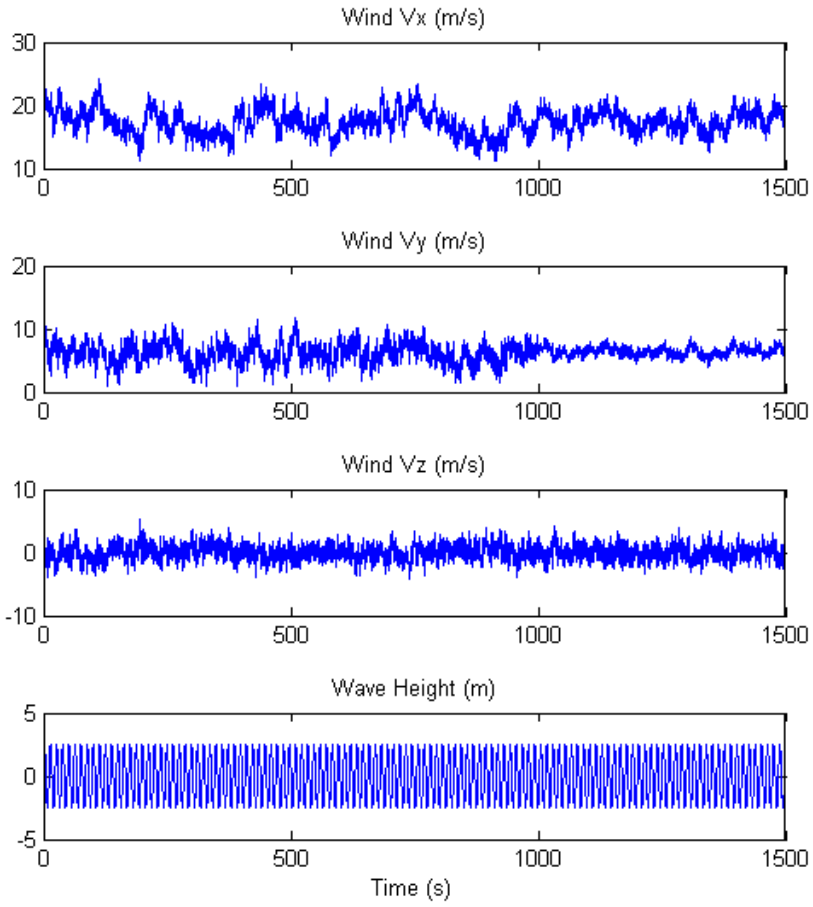

Figure 3.19: Wind and Wave Profiles for Realistic Open-Loop Test.

where parameters s_α, g and s_β are constants, and ω_0 is given by

$$\omega_0 = \frac{g}{U_{19.5}}. \tag{3.54}$$

Here, $U_{19.5}$ is the wind velocity at a height of 19.5 m above sea level. Since our reference height is much higher, we can estimate $U_{19.5}$ by using the

power law approximation

$$U_{19.5} = U_{90}\left(\frac{h_{19.5}}{h_{90}}\right)^{\kappa}, \tag{3.55}$$

where U_{90} is the wind speed at height 90 m, $h_{19.5}$ and h_{90} represent reference heights of 19.5 m and 90 m, respectively, and κ is the wind power exponent which has the value 0.11 over open water environments [39]. The Pierson-Moskowitz spectrum is shown in Figure 3.20 for the above conditions. From here we extract the significant wave height and peak spectral period for the above wind conditions, which we can then use as inputs to FAST.

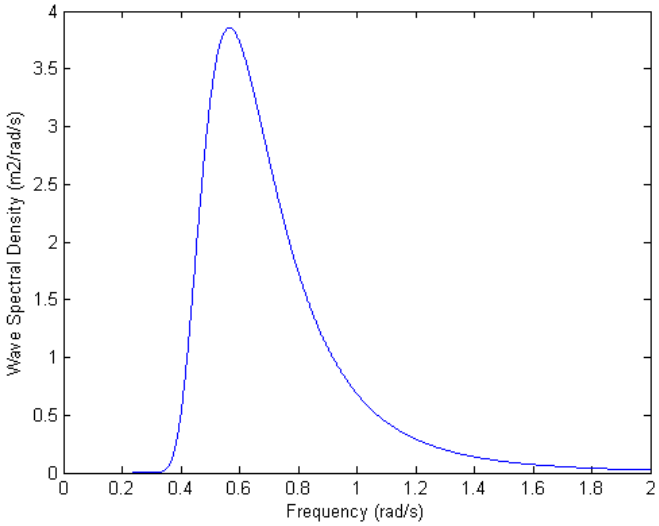

Figure 3.20: Pierson-Moskowitz Energy Density Spectrum for Given Criterion.

Control Inputs The open-loop control input trajectories were chosen to mimic realistic responses to the wind disturbance with the objective of simple power capture, similar to that of the 5MW baseline controller. First, the yaw angle was created with the objective of tracking the wind direction. However, given the limited speed of the yaw actuator, the one-to-one trajectory was smoothed using a locally weighted scatter plot smoothing method

such that its maximum time derivative was less than the actuator limitation of 0.3 deg/s. The resulting yaw trajectory, overlaid on the wind direction, is shown in Figure 3.21.

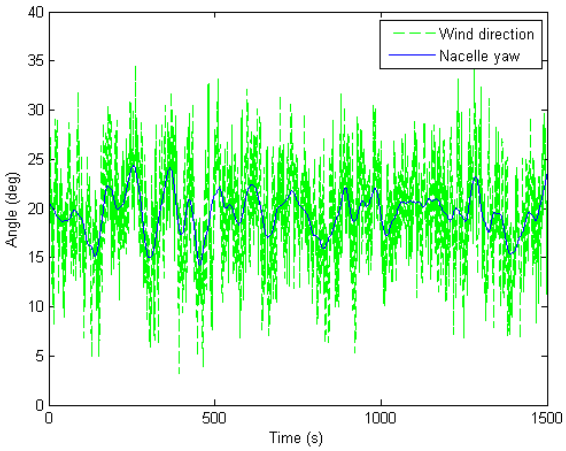

Figure 3.21: Nacelle Yaw Angle Trajectory.

The blade pitch angle trajectory was then created with the goal of maintaining constant aerodynamic power. This is accomplished by setting the instantaneous change in power to zero for all time, or

$$\delta P(t) = \frac{\partial P(t)}{\partial \mathbf{x}}\delta\mathbf{x} + \frac{\partial P(t)}{\partial \mathbf{u}}\delta\mathbf{u} + \frac{\partial P(t)}{\partial \mathbf{v}}\delta\mathbf{v} = 0. \tag{3.56}$$

As this is an open-loop simulation, and thus we are not interested in integrating the equations of motion and solving for the states over time, we ignore the state vector $\mathbf{x}$. Removing the state term, and inserting the relevant inputs, this simplifies to

$$\frac{\partial P(t)}{\partial \beta}\delta\beta + \frac{\partial P(t)}{\partial \gamma}\delta\gamma + \frac{\partial P(t)}{\partial \mathbf{v}}\delta\mathbf{v} = 0. \tag{3.57}$$

Finally, we solve for the blade pitch angle

$$\delta\beta = -\left(\frac{\partial P(t)}{\partial \gamma}\delta\gamma + \frac{\partial P(t)}{\partial \mathbf{v}}\delta\mathbf{v}\right) / \left(\frac{\partial P(t)}{\partial \beta}\right). \tag{3.58}$$

As in the case for the yaw angle, the resulting trajectory invalidates the actuator limits. To resolve this issue, we again apply locally weighted scatter plot smoothing, leading to the final trajectory, shown in Figure 3.22.

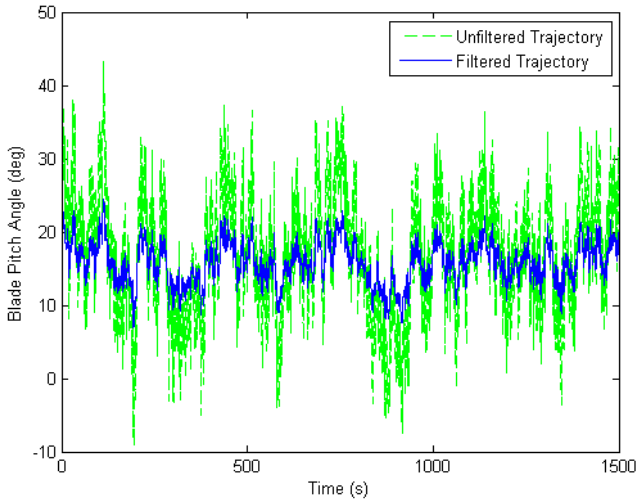

Figure 3.22: Blade Pitch Angle Trajectory for Realistic Open-Loop Test.

In region 3, generator torque is typically either held fixed at the rated value, letting the blade pitch actuation maintain constant power, or it is adjusted inversely to generator speed to help maintain constant power. Neglecting state changes, both these options result in constant torque for the open-loop simulation. However, for the purpose of validating the effects of all control inputs and disturbances, we elect to use a slightly more advanced generator torque control strategy. That is, we attempt to hold rotor speed constant with generator torque. This can be done by ignoring the shaft dynamics between the rotor and generator side shafts, and translating the generator torque directly to the rotor side

$$\dot{\omega}_r = \frac{1}{J_r}\left(\frac{P}{\omega_r} - (N_{GR})T_g\right) = 0. \tag{3.59}$$

Following similar steps to the blade pitch angle case, we can simplify this

equation to

$$\delta T_g = \frac{1}{N_{GR}\omega_r}\left(\frac{\partial P(t)}{\partial \beta}\delta\beta + \frac{\partial P(t)}{\partial \gamma}\delta\gamma + \frac{\partial P(t)}{\partial \mathbf{v}}\delta\mathbf{v}\right) \tag{3.60}$$

The final trajectory is shown in Figure 3.23.

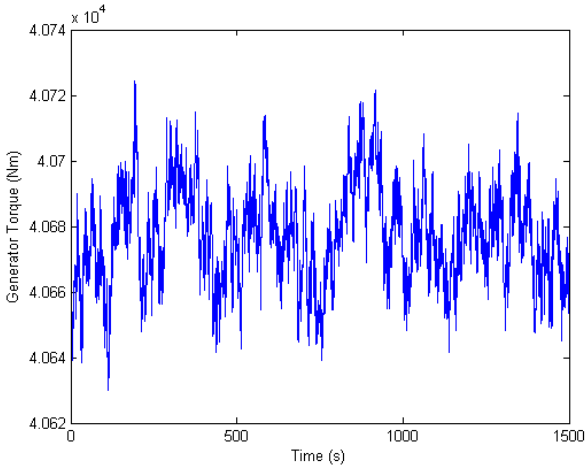

Figure 3.23: Generator Torque Trajectory.

Results The time series results for the simulations done in both FAST and the proposed non-linear model are shown in Figure 3.24, and the mean and standard deviations of the time series' are tabulated in Table 3.3.

Evidently, from Figure 3.24, the proposed control-oriented model very accurately predicts the major motions of the full 44-state FAST model, even in the presence of wind and wave disturbance, actuator effects, and coupled 3-D motion. There is minor discrepancy in the platform yaw degree of freedom as well as the two drivetrain velocities. In all three cases, this can be attributed to the periodic bending motions of the blades as they rotate about the hub due to periodic gravitational effects, and the tip-speed effect discussed in Section 3.3.2. Because the effect is minor, however, and because introducing periodicity to the non-linear model would make generating linear time-invariant plants impossible, we continue in our decision not to model

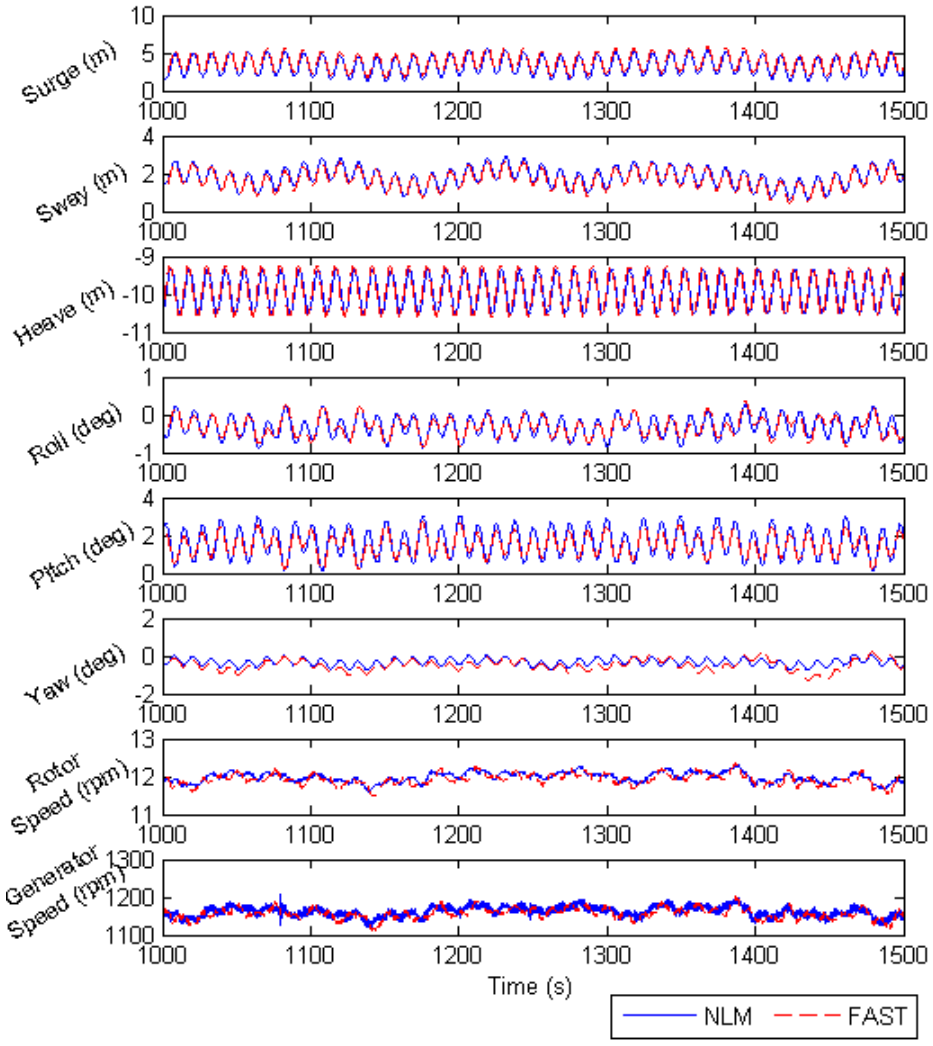

Figure 3.24: Realistic open-loop Test Results.

it.

As an additional source of validation, we looked at the frequency response of the time series responses of the realistic open-loop test. These are shown in Figures 3.25, 3.26 and 3.27. In Figure 3.25, the large amplitude spikes at 0.5

Table 3.3: Realistic Open-Loop Test Results for Non-Linear Models

DOF	Mean COM	Mean FAST	RMS COM	RMS FAST
Surge (m)	3.4363	3.8418	1.1789	1.152
Sway (m)	1.8477	1.7045	0.55266	0.53453
Heave (m)	-9.9328	-9.9155	0.407	0.46666
Roll (deg)	-0.34107	-0.33334	0.27595	0.26428
Pitch (deg)	1.6481	1.5351	0.76216	0.5842
Yaw (deg)	-0.15391	-0.48659	0.17994	0.32669
Rotor Speed (rpm)	11.9842	11.9191	0.14502	0.161
Generator Speed (rpm)	1162.4665	1156.1478	15.1428	15.6932

rad/s correspond to the effect of the wave disturbance on the translational states. The lower frequency excitation can be attributed to the natural

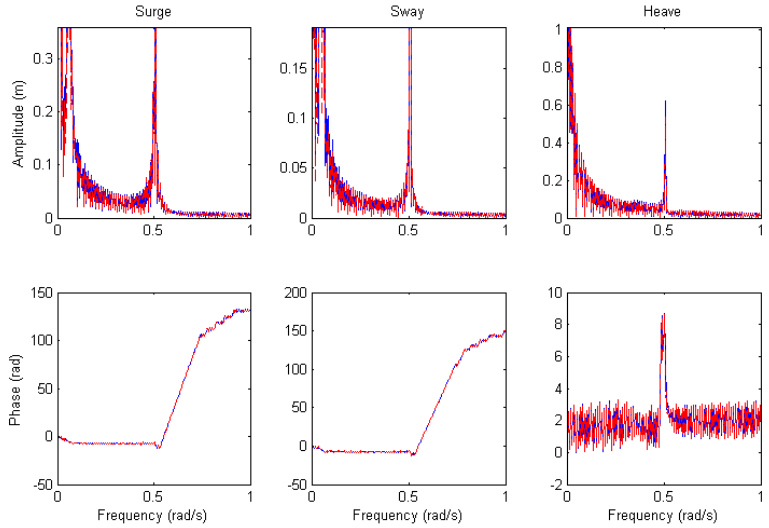

Figure 3.25: Frequency Response for Translational States.

frequencies of the the platform, and the actuator effects. Figure 3.26 shows the frequency response of the rotational states of the system. Again, we

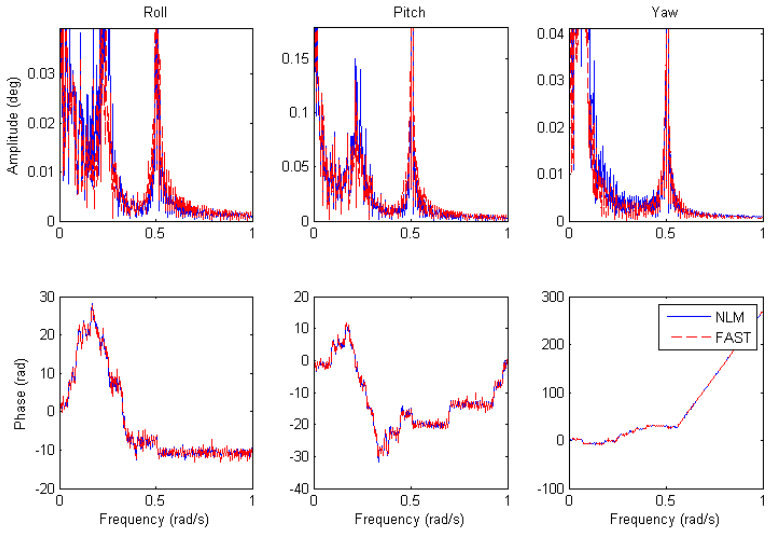

Figure 3.26: Frequency Response for Rotational States.

see the effect of wave disturbance, as well as several other modes. The additional peaks are a result of the fact that the rotational reactions are affected by both the temporal frequency of the waves (like the displacement states) and the spatial frequency. Finally, in Figure 3.25, we see that the drivetrain degrees of freedom are relatively unaffected by the wave effects, and dominated by the wind and actuator effects.

3.6 Summary

In this chapter, we defined a general, control-oriented, non-linear model for floating offshore wind turbines that captures the major dynamics of a WTS. By considering the 5MW baseline wind turbine, we described the details of generating this non-linear model and acquiring the necessary parameters from existing software. Finally, we subjected the proposed model to four validation tests spanning a multitude of operating conditions to verify its effectiveness in the presence of wind and wave disturbances, actuator dynamics, and strongly coupled 3-D motions. More importantly, we confirmed

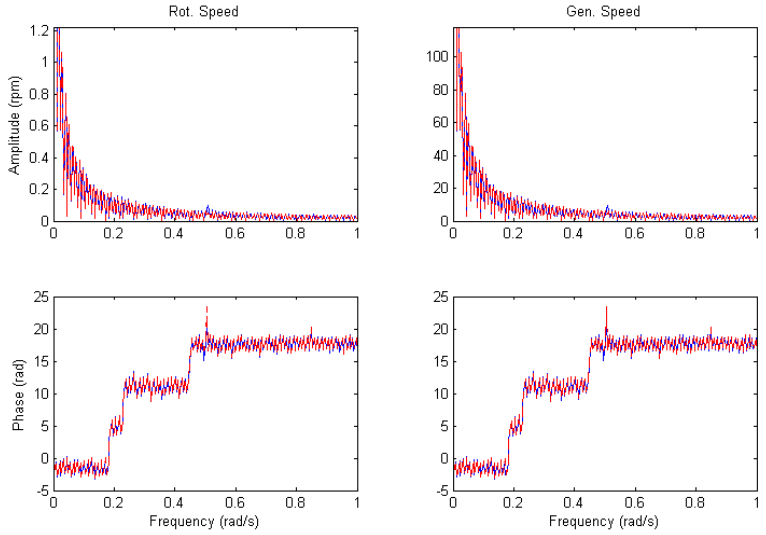

Figure 3.27: Frequency Response for Shaft States.

that a simple non-linear model could very accurately predict the major dynamics of a floating wind turbine, while maintaining reasonable simplicity such that is a good fit for controller design.

The major contributions of this chapter stem from two key facts. The first is simply that the proposed model offers an optimized balance of simplicity and accuracy. Simplicity allows us to maintain a fundamental understanding of its workings and perform operations like analytical linearization, while accuracy is necessary for controller design purposes. More specifically, the model remains accurate throughout the highly non-linear operating range of the wind turbine. This means that this one model is always valid, and does not need to be re-derived or regenerated like many of the simple control models used in research [11, 25, 28, 31]. On a more fundamental level, though, because the model is physics based, it means that we can make intuitive changes to the parameters for testing design changes or replaceable components. For example we can experiment with different levels of mooring line stiffness, tower heights, mass properties, or aerodynamic properties. The allowance for these mechanical design changes means

that the non-linear model could even be used as a first step in collaborating mechanical design with the design of the control system. Traditionally, mechanical design would precede controller design, and the processes would be independent.

Chapter 4

Linear Model

4.1 Introduction

In the previous chapter, we derived the simplified non-linear model from first principles. For controller design, however, it is generally more advantageous to have a time-invariant linear model. The purpose of this section is to show how to use the physically-derived non-linear model from Chapter 3 to generate a linear model. We begin by defining the operating point for a such a linear model, and describing a method to generate it. Next, we use the generated operating point to derive the time-invariant linear model, and perform some simple manipulations to it to improve its accuracy. Finally, we validate it by comparing it to FAST and a linearized model generated by FAST, in a time-series simulation.

4.2 Derivation of Linear Model and Equilibrium Points

In order to create a linear model from a non-linear model, we first need to define an operating point, $\mathbf{p}$. The operating point can be either constant, or periodic, and comprises the states, inputs and disturbances for the particular trajectory. More precisely, we define the operating point as

$$\mathbf{p} = \begin{bmatrix} \mathbf{x_{op}} \\ \mathbf{u_{op}} \\ \mathbf{v_{op}} \\ \mathbf{w_{op}} \end{bmatrix}, \tag{4.1}$$

where the subscript "op" indicates the operating point. Given such an operating point, any small perturbation from it can be approximated by a linear state space model

$$\delta\dot{\mathbf{x}} = \underline{\mathrm{A}}|_{\mathbf{p}}\,\delta\mathbf{x} + \underline{\mathrm{B}}|_{\mathbf{p}}\,\delta\mathbf{u} + \underline{\mathrm{B}}_v|_{\mathbf{p}}\,\delta\mathbf{v} + \underline{\mathrm{B}}_w|_{\mathbf{p}}\,\delta\mathbf{w} \tag{4.2}$$

$$\delta\mathbf{y} = \underline{\mathrm{C}}|_{\mathbf{p}}\,\delta\mathbf{x} + \underline{\mathrm{D}}|_{\mathbf{p}}\,\delta\mathbf{u} + \underline{\mathrm{D}}_v|_{\mathbf{p}}\,\delta\mathbf{v} + \underline{\mathrm{D}}_w|_{\mathbf{p}}\,\delta\mathbf{w}, \tag{4.3}$$

where the perturbation state vector is defined by $\delta\mathbf{x} := \mathbf{x} - \mathbf{x_{op}}$, and other perturbation vectors $\delta\mathbf{u}$, $\delta\mathbf{v}$ and $\delta\mathbf{w}$ are defined analogously. The following subsections will explain the process of acquiring a valid operating point from the non-linear model, and deriving the linear state space model at the acquired operating point.

4.2.1 Selection of an Operating Point

Due to the non-linearity of the WTS, the selection of an operating point can make a large difference in the accuracy of the model. For example, the effect of a positively increasing control input β and the produced power is positive in one part of the operating region of the wind turbine, and negative in another. Hence, a controller synthesized at a far operating point would not only be ineffective, but almost surely unstable.

The only criterion for the validity of an operating point or trajectory is that the non-linear equation of motion for the WTS from Chapter 3 is satisfied, that is

$$\dot{\mathbf{x}}_{\mathbf{op}}(t) = f(\mathbf{x}_{\mathbf{op}}(t), \mathbf{u}_{\mathbf{op}}(t), \mathbf{v}_{\mathbf{op}}(t), \mathbf{w}_{\mathbf{op}}(t)). \tag{4.4}$$

Generally, a time-varying operating trajectory should be periodic. If the operating point is time-invariant, this restriction can be simplified to

$$f(\mathbf{x}_{\mathbf{op}}, \mathbf{u}_{\mathbf{op}}, \mathbf{v}_{\mathbf{op}}, \mathbf{w}_{\mathbf{op}}) = \mathbf{0}. \tag{4.5}$$

It is important to note that we cannot solve for an independent rotor and generator azimuth angle using this method. That is, we must use the com-

bined state $\theta_r - \frac{\theta_g}{N_{GR}}$. The method of finding the operating point differs depending on whether or not we are interested in a fixed operating point, or a periodic operating trajectory. While the proposed model can be linearized about either, for simplicity we will focus on only the fixed operating point.

Fixed operating point Fixed operating points can easily be solved for using iterative methods, once the problem has been properly defined. First, consider the non-linear function f from (4.5). Let the variables $\mathbf{x_{op}}, \mathbf{u_{op}}, \mathbf{v_{op}}$ and $\mathbf{w_{op}}$ have n_x, n_u, n_v and n_w elements, respectively. Then, f must have n_x rows. Furthermore, in order for the operating point to be time-invariant, several states are predetermined. This can also be shown as a consequence of (3.7) and (4.5), or

$$\begin{aligned} \dot{\vec{x}}_g &= \vec{0} \\ \dot{\vec{\theta}} &= \vec{0} \\ \omega_r &= \tfrac{1}{N_{GR}}\omega_g \end{aligned} \quad . \tag{4.6}$$

Through this simplification, both the number of undetermined state variables and order of the non-linear equations drop from n_x to a certain number which we call n_{xu}. Let us also define a new non-linear function that does not include the redundant information

$$f_u(\mathbf{x}, \mathbf{u}, \mathbf{v}, \mathbf{w}) := \begin{bmatrix} \vec{f}_F(\mathbf{x}, \mathbf{u}, \mathbf{v}, \mathbf{w}) \\ \vec{f}_T(\mathbf{x}, \mathbf{u}, \mathbf{v}, \mathbf{w}) \\ f_Q(\mathbf{x}, \mathbf{u}, \mathbf{v}) \end{bmatrix}. \tag{4.7}$$

The order of the function f_u represents the maximum number of variables that can be solved for using iteration methods. In other words, n_{xu} of the $n_{xu} + n_u + n_v + n_w$ operating point variables can be explicitly solved for, the others must be chosen. If we denote the to-be-determined variables $\mathbf{p_u}$, then there exists a linear transformation $\underline{\mathrm{T}}_p$ such that

$$\mathbf{p_u} = \underline{\mathrm{T}}_p \mathbf{p}, \tag{4.8}$$

and another linear transformation $\underline{\mathrm{T}}_f$ such that

$$f_u = \underline{\mathrm{T}}_f f \tag{4.9}$$

Using a multi-variable form of Newton's method [40], we can iteratively solve for $\mathbf{p_u}$ using the expression

$$\mathbf{p_u^{k+1}} = \mathbf{p_u^k} - \left[\frac{\partial \mathbf{f_u}}{\partial \mathbf{p_u^k}}\right]^{-1} \mathbf{f_u}(\mathbf{p^k}), \tag{4.10}$$

where the superscript k represents the k^{th} iteration, and the inverse term can be found by solving the equation

$$\left[\frac{\partial f_u}{\partial \mathbf{p_u^k}}\right] \underline{\mathrm{T}}_p = \underline{\mathrm{T}}_{fg} \left[\begin{array}{cccc} \underline{\mathrm{A}}|_{\mathbf{p^k}} & \underline{\mathrm{B}}|_{\mathbf{p^k}} & \underline{\mathrm{B}}_v|_{\mathbf{p^k}} & \underline{\mathrm{B}}_w|_{\mathbf{p^k}} \end{array} \right]. \tag{4.11}$$

Equation (4.11) represents a very important result, as it lets us solve for the equilibrium point very quickly using only the partial derivatives of the non-linear function at each iteration step. On the other hand, in FAST, equilibrium points are determined by running long simulations in the time domain. Depending on the initial conditions, the time it takes to reach equilibrium often exceeds the maximum allowable runtime, which makes the equilibrium point unobtainable.

4.2.2 Derivation of the State-Space Model

Consider a small perturbation about the equilibrium trajectory from (4.4). From general linearization theory, as long as the perturbation is sufficiently small, we can write a linear system as

$$\delta\dot{\mathbf{x}} = \left.\frac{\partial \mathbf{f}}{\partial \mathbf{x}}\right|_{\mathbf{p(t)}} \delta\mathbf{x} + \left.\frac{\partial \mathbf{f}}{\partial \mathbf{u}}\right|_{\mathbf{p(t)}} \delta\mathbf{u} + \left.\frac{\partial \mathbf{f}}{\partial \mathbf{v}}\right|_{\mathbf{p(t)}} \delta\mathbf{v} + \left.\frac{\partial \mathbf{f}}{\partial \mathbf{w}}\right|_{\mathbf{p(t)}} \delta\mathbf{w}. \tag{4.12}$$

It is clear, then, that the linear model matrices from (4.2) are simply the partial derivative matrices from (4.12), or

$$\begin{aligned} \underline{\mathrm{A}}|_{\mathbf{p}(t)} &= \left.\frac{\partial f}{\partial \mathbf{x}}\right|_{\mathbf{p}(t)}, \quad \underline{\mathrm{B}}|_{\mathbf{p}(t)} = \left.\frac{\partial f}{\partial \mathbf{u}}\right|_{\mathbf{p}(t)} \\ \underline{\mathrm{B}}_v|_{\mathbf{p}(t)} &= \left.\frac{\partial f}{\partial \mathbf{v}}\right|_{\mathbf{p}(t)}, \quad \underline{\mathrm{B}}_w|_{\mathbf{p}(t)} = \left.\frac{\partial f}{\partial \mathbf{w}}\right|_{\mathbf{p}(t)} \end{aligned} . \tag{4.13}$$

Similarly, if we are interested in outputs $\mathbf{y}$, given by the equation

$$\mathbf{y} = \mathbf{g_o}(\mathbf{x}, \mathbf{u}, \mathbf{v}, \mathbf{w}), \tag{4.14}$$

then the output matrices from (4.2) can be written as

$$\begin{aligned} \underline{\mathrm{C}}|_{\mathbf{p}(t)} &= \left.\frac{\partial g_o}{\partial \mathbf{x}}\right|_{\mathbf{p}(t)}, \quad \underline{\mathrm{D}}|_{\mathbf{p}(t)} = \left.\frac{\partial g_o}{\partial \mathbf{u}}\right|_{\mathbf{p}(t)} \\ \underline{\mathrm{D}}_v|_{\mathbf{p}(t)} &= \left.\frac{\partial g_o}{\partial \mathbf{v}}\right|_{\mathbf{p}(t)}, \quad \underline{\mathrm{D}}_w|_{\mathbf{p}(t)} = \left.\frac{\partial g_o}{\partial \mathbf{w}}\right|_{\mathbf{p}(t)} \end{aligned} . \tag{4.15}$$

There are some effects, however, that the partial derivative model does not accurately represent. Therefore, some slight manipulations can be made to the linearization process. These are explained in the following section.

4.3 Manipulation of the Linear Model

4.3.1 Quadratic Drag

From Chapter 3, Morison's equation contains the hydrodynamic drag force expression:

$$\vec{F}_d = C||\vec{v}_t||\vec{v}_t. \tag{4.16}$$

The partial derivative of this, with respect to one of the states, i, can be written as

$$\frac{\partial \vec{F}_d}{\partial \mathbf{x_i}} \left(\frac{\partial ||\vec{v}_t||}{\partial \mathbf{x_i}} \vec{v}_t + ||\vec{v}_t|| \frac{\partial \vec{v}_t}{\partial \mathbf{x_i}} \right). \tag{4.17}$$

For the WTS, we usually linearize the model about a point with zero mean velocity, which renders all terms in the above equation zero. This is not ideal, however, because although we expect zero mean wave velocity, we do expect oscillatory movement about the equilibrium point. For this reason,

we have applied a correction to the above equation, to account for the actual drag force on the system. This is done by replacing the absolute value $||\vec{v}_t||$ in the right-most term by a new, constant value $||\vec{v}_{t,nom}||$. This does not alter the desired directional properties of the force, as the corrected term must always be positive. The corrected velocity is determined by equating the energy dissipated in a 1-D linear drag model and a 1-D quadratic drag models over half an oscillation period. That is,

$$-C\int_0^{\frac{\pi}{\omega}} ||v(t)||v(t)(v(t)dt) = -C||v||_{nom}\int_0^{\frac{\pi}{\omega}} v(t)(v(t)dt). \tag{4.18}$$

If we assume $v(t)$ follows a sinusoidal profile $v(t) = v_0 sin(\omega t)$, the above integrals can be solved analytically. Switching back to the 3-D model, this leaves the relationship

$$||\vec{v}||_{nom} = \left(\frac{8}{3\pi}\right) v_0. \tag{4.19}$$

To obtain v_0, we can excite our non-linear model with a regular wave profile whose frequency and amplitude corresponds to the expected ocean wave spectrum, and find the resulting velocity amplitude v_0 such that

$$v_0 = \max(||\vec{v}(t)||) \tag{4.20}$$

4.4 Validation of the Linear Model

To validate the linear model, we can compare the simulation results for a linear model created using the above process, with the full non-linear FAST simulation that was done in Section 3.5.4. Furthermore, to highlight the advantages of the proposed linear model, we compare it to a 42-state linear model generated by FAST.

4.4.1 Linearization Point - NLM

The equilibrium or linearization point was generated using the static equilibrium point finding process described in Section 4.2. Because of the static condition, all the velocity states were set to zero. The wind velocity vector

was set to constant 18 m/s at 20° about the $\hat{e}_3$-axis. All of the components in the wave disturbance signal were set to zero. Finally, the rotor speed and generator torque were set to their rated values, and the yaw was set to 20°. That left all the displacement states to be determined, as well as the rotor flexibility and the blade pitch angle by the equilibrium point solving method. The full equilibrium point then is

$$\mathbf{x} = \begin{matrix} \{3.90m, 1.76m, -9.91m, \\ -0.50°, 1.60°, -0.06°, \\ 0.26°, \\ 0, \ldots 0, \\ 12.1rpm, 1173.7rpm\} \end{matrix}, \tag{4.21}$$

$$\mathbf{u} = \{15.16°, 40.68kNm, 20°\}, \tag{4.22}$$

$$\mathbf{v} = \{16.91m/s, 6.16m/s0m/s\}, \tag{4.23}$$

$$\mathbf{w} = \{0, \ldots, 0\}. \tag{4.24}$$

4.4.2 Linearization Point - FAST

The linearization point was found by using FAST's linearization feature with all degrees of freedom enabled except the nacelle yaw bearing stiffness. This process is explained in more detail in [10]. The linearization process took just less than 1500 simulated seconds to achieve a convergence tolerance of less than 10^{-3} rad and 10^{-3} rad/s for the 2-norm of displacements and velocities, respectively. For brevity, the full 42-state equilibrium point will not be shown, but the values corresponding to the states and control inputs of the proposed non-linear model are

$$\mathbf{x} = \begin{matrix} \{3.66m, 1.85m, -9.90m, \\ -0.35°, 1.56°, -0.70°, \\ 0.26°, \\ 0, \ldots 0, \\ 12.13rpm, 1176.4rpm\} \end{matrix}, \tag{4.25}$$

$$\mathbf{u} = \{15.11^\circ, 40.65kNm, 20^\circ\}, \tag{4.26}$$

$$\mathbf{v} = \{16.91m/s, 6.16m/s0m/s\}, \tag{4.27}$$

All of these values are very close to those obtained using the non-linear model with one exception, the platform yaw. This deviation can be explained by the relative tip-speed effect which was mentioned in Section 3.3.2. Because of the tilt of the rotor about the $\hat{e}_2$-axis, both due to the steady state platform pitch angle, and the physical tilt of the rotor, the blades alternate between moving toward the incoming wind and away from it, as they perform a full revolution. This effect causes a constant moment about the $\hat{e}_3$-axis due to the changing thrust forces on the blades, which leads to the steady-state platform yaw angle. As explained in 3.3.2, however, the effect is small and thus it is neglected in the proposed model.

4.4.3 Open-Loop Test Results

The test conditions remain exactly the same as those described in Section 3.5.4, and each of the two linear models begin the simulation at all states equal to zero. The time series results for the full-DOF FAST model, proposed linear model, and the linear FAST model are shown in Figure 4.1, and the RMS errors, given in percent, for the time series difference between each linear model and FAST are given in Table 4.1.

Table 4.1: Realistic Open-Loop Test for Linear Models.

DOF	RMS Error % NLM	RMS Error % FAST
Surge	12.3103	98.0504
Sway	33.5927	142.1242
Heave	31.552	100.0169
Roll	57.3344	105.7494
Pitch	43.4443	88.5098
Yaw	89.4817	96.0532
Rotor Speed	108.1024	134.5055
Generator Speed	108.1649	134.0284

As we expect, the lack of a B_w disturbance matrix in the FAST linear

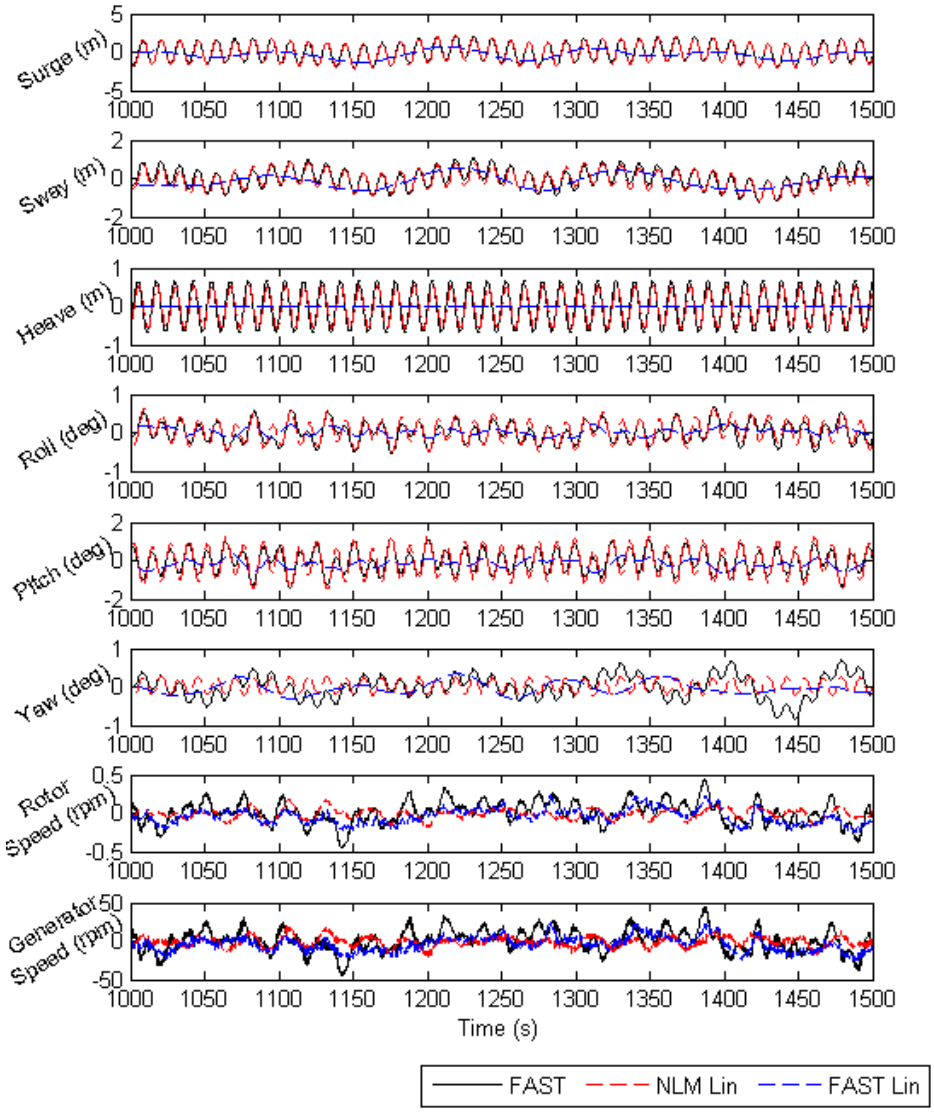

Figure 4.1: Realistic Open-Loop Test Results for the Linear Models.

model results in an inability to predict the wave-induced platform motions. Contrarily, the proposed non-linear model shows very accurate results for the

platform motion DOFs, resulting in massive improvements in RMS error %. For the drivetrain degrees of freedom, the proposed non-linear model is able to predict the major motions caused by the balanced aerodynamic forces (i.e., changing wind disturbance and effects of control input), however it is unable to predict the periodic motions caused by the bending of the blades due to gravity, the tip-speed-effect, and inertial forces. Because this is a periodic effect, it cannot be captured by any time-invariant linear model, including the 42-state FAST linear model. As a result, there is a minor improvement in the rotor and generator RMS error % for the proposed model compared to the FAST linear model.

Another important note to make is, because of the complexity of the FAST model, the equilibrium point that was found was not accurate enough, despite a very lengthy linearization process. As a result, we start to see wandering of the states by the end of the linear simulation. This is analogous to linearizing a non-linear model by taking partial derivatives at an operating point where (4.4) is not satisfied. To combat this, either less states could be chosen, or tolerance restrictions could be raised. The former solution would result in a lower accuracy linear model, and the latter would require exponentially longer linearization time. Furthermore, FAST restricts the total allowable linearization time to 9999s, which is only slightly higher than the time used to find the above equilibrium point.

4.5 Summary

In this chapter, we formulated an explicit procedure for determining time-invariant operating points from the proposed non-linear model, described in Chapter 3. Using this operating point, we then derived the state-space linearized model for use in controller design. Because of the intuitive nature of the proposed model, we were also able to perform manipulations to the linearized model to improve accuracy where the behavior of the WTS was particularly non-linear. Finally, we validated the linear model using a realistic open-loop test, involving changing wind and wave disturbances, actuator dynamics, and fully coupled 3-D motion.

This chapter highlights several important contributions of our work. The most obvious of such being the generation of accurate linear models which are required for many types of controller design. Another major achievement is the proposed method for determining operating points which remains fast and effective even when initial condition selection is poor. In contrast, the linearization feature in FAST is slow and highly sensitive to initial condition selection. Often the linearization point is not solvable to a reasonable degree of accuracy in the maximum allowable runtime of the software, as was indicated by the states drifting in the realistic open-loop test. Furthermore, other interesting things can be done using the proposed method for determining operating points, such as finding the moveable range of the wind turbine at various power levels. This could prove to be very useful in wind farm control to minimize the wake effects of upwind wind turbines on downwind wind turbines.

Chapter 5

Controller Design

5.1 Introduction

In the previous chapters, it was shown that a simplified non-linear model could be used to generate accurate linear state-space models that include the wave disturbance matrix B_w. Based on the effectiveness of disturbance accommodation in other floating wind turbine research [11, 24, 27], it is predicted that controllers that consider this disturbance relationship in their design, will provide significant improvement over control techniques that do not. In this chapter, we explore this thesis by comparing four types of controllers; a non-model-based PID controller that is tuned using the non-linear model; a model-based linear-quadratic-regulator (LQR) with integrator and observer; a disturbance-rejecting model-based robust H_∞ controller; and finally a disturbance-accommodating feedforward H_∞ controller.

5.2 Test Conditions and Equilibrium Point

In this section, the test conditions for the comparison of the three controllers are defined, and the equilibrium point and linear model is established. The general conditions are similar to the validation tests for both the linear and non-linear models, however as we are no longer comparing with FAST, it is possible to use more realistic irregular waves, which will be explained in the following subsection.

5.2.1 Disturbance

The wind disturbance remains the same as in the non-linear and linear validation tests. That is, 18m/s mean at a 20° angle about the z-axis. The wave disturbance was built using the Pierson-Moskowitz spectrum with the same peak spectral period, significant wave height, and direction as before, but the single wave frequency was replaced by a more realistic fully developed wave profile that fits the Pierson-Moskowitz energy density spectrum. The wave profile was constructed using the following method. First, the energy density spectrum is split into $n = \frac{\omega_{co}}{\Delta\omega}$ frequency components, as shown in Figure 5.1. Here, ω_{co} is the cut-off frequency we choose to approximate the highest frequency in the realistic wave profile. Then, an irregular wave

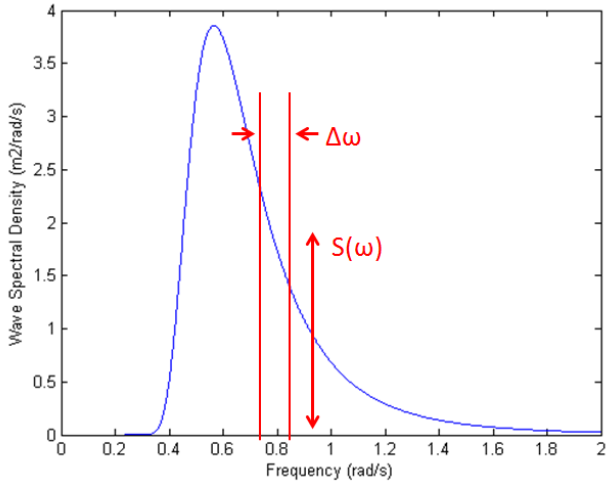

Figure 5.1: Construction of a Wave Profile from the Pierson-Moskowitz Spectrum.

profile can be constructed by the summation of n monochromatic waves, or one for each frequency band. The amplitude of each wave is given by

$$A_i = \sqrt{2S(\omega_i)\Delta\omega}, \tag{5.1}$$

and the phase by

$$\phi_i = rand(0 : 2\pi). \tag{5.2}$$

Finally, we can calculate the full wave disturbance vector at any spatial and temporal location with the following formulae

$$\zeta_i = \frac{-\omega_i^2}{g} x + \omega_i t + \phi_i, \tag{5.3}$$

$$h(x,t) = \sum_i A_i \sin(\zeta_i) \tag{5.4}$$

$$\vec{v}(x,t) = \sum_i \omega_i \exp\left(\frac{-\omega_i^2}{g} z\right) \begin{bmatrix} \cos(\alpha)\sin(\zeta_i) \\ \sin(\alpha)\sin(\zeta_i) \\ \cos(\zeta_i) \end{bmatrix}, \tag{5.5}$$

$$\vec{a}(x,t) = \sum_i \omega_i^2 \exp\left(\frac{-\omega_i^2}{g} z\right) \begin{bmatrix} \cos(\alpha)\cos(\zeta_i) \\ \cos(\alpha)\cos(\zeta_i) \\ -\sin(\zeta_i) \end{bmatrix}, \tag{5.6}$$

$$P(x,t) = \sum_i \rho g \exp\left(\frac{-\omega_i^2}{g} z\right) \sin(\zeta_i). \tag{5.7}$$

5.2.2 Linearization Point

The equilibrium or linearization point was generated using the static equilibrium point finding process described in Section 4.2, and is the same as the one derived in Section 4.4.1. To reiterate, the wind velocity vector was set to constant 18m/s at 20° about the z-axis, the wave disturbance signals were set to zero, the rotor speed and generator torque were set to their rated values, and the yaw was set to 20°. The other displacement states were determined, as well as the rotor flexibility and the blade pitch angle were determined using the equilibrium point solving method. The full equilibrium point then is

$$\mathbf{x} = \begin{matrix} \{3.90m, 1.76m, -9.91m, \\ -0.50°, 1.60°, -0.06°, \\ 0.26°, \\ 0, \ldots 0, \\ 12.1rpm, 1173.7rpm\} \end{matrix}, \tag{5.8}$$

$$\mathbf{u} = \{15.16^{\circ}, 40.68kNm, 20^{\circ}\}, \tag{5.9}$$

$$\mathbf{v} = \{16.91m/s, 6.16m/s0m/s\}, \tag{5.10}$$

$$\mathbf{w} = \{0, \ldots, 0\}. \tag{5.11}$$

5.2.3 Control Objectives

For region 3 operating conditions, the controller objective should be to maintain a constant 5MW power capture, while minimizing platform and rotor twisting motions. More specifically, the controller should minimize platform roll and pitch accelerations, and rotor twist acceleration, while maintaining rotor speed and power captured. It will be assumed that there are multiple sensors on the wind turbine, with the ability to measure all the positional states of the turbine, the rotor twist angle, the platform roll and pitch accelerations, and rotor twist accelerations, the generator speed and the power. All these measurements are realistically obtainable, however it is also possible to use a state-estimator to reduce the number of sensors required. Furthermore, because the design of such a state estimator can be decoupled from the controller design, it is justified to assume access to all the above output information. The output vector $\mathbf{y}$ can then be written as

$$\mathbf{y} = \begin{bmatrix} \vec{x}_g \\ \vec{\theta} \\ \theta_r - \frac{1}{N_{GR}}\theta_g \\ \ddot{\theta}_x \\ \ddot{\theta}_y \\ \omega_g \\ \ddot{\theta}_r - \frac{1}{N_{GR}}\ddot{\theta}_g \\ \omega_g T_g \end{bmatrix}. \tag{5.12}$$

Note that not all the controllers use all the available outputs, but the above vector $\mathbf{y}$ represents the potential outputs available. With all of the test conditions set, and the controller objectives defined, we can design the PID, LQR and H_∞ controllers for comparison purposes. The following sections

will explain the design of each controller, and finally the comparison will be performed.

5.2.4 Performance Metrics

Several performance metrics will be used to compare the relative performance of the various controllers. Specifically, similar to [5] and [17], we will use the RMS of the following signals: platform roll, pitch and their time derivatives, rotor twist and its time derivative, blade pitch rate, power error, and rotor speed error. The platform motion indices give an estimate of the tower structural fatigue loading, the rotor twist indices give an estimate of the drivetrain fatigue loading, and finally the rotor speed and power errors give an estimate of both the power output and the generator loads. Often, we will normalize these performance metrics for a particular controller with respect to a baseline controller by dividing the former by the latter.

5.3 Design of the PID Controller

Gain-scheduling PID controllers are often used in onshore wind turbine control due to the simplicity of their design, analysis and implementation. However, it was shown in Chapter 1 that the floating offshore wind turbine control problem is much more complex than the onshore problem because of the additional aspects to be considered, such as platform motion, auxiliary sensors and wave disturbance. For PID design, this means that for every input/output combination, a distinct PID controller must be developed and tuned in parallel with every other PID controller. It is also important to carefully select a number of such controllers that balances design complexity and controllability. Intuitively, we elect to design six distinct PID controllers $(G_1(s) \dots G_6(s))$, to regulate the platform roll and pitch accelerations, the generator speed, the rotor shaft torsion, and the captured power. The blade

pitch angle, then, is given by

$$\beta(s) = \begin{bmatrix} G_1(s) & G_2(s) & G_3(s) & G_4(s) \end{bmatrix} \begin{bmatrix} \ddot{\theta}_x(s) \\ \ddot{\theta}_y(s) \\ \delta\omega_g(s) \\ \ddot{\theta}_r(s) - \frac{1}{N_{GR}}\ddot{\theta}_g(s) \end{bmatrix}, \quad (5.13)$$

and the generator torque, by

$$T_g(s) = \begin{bmatrix} G_5(s) & G_6(s) \end{bmatrix} \begin{bmatrix} \ddot{\theta}_r(s) - \frac{1}{N_{GR}}\ddot{\theta}_g(s) \\ \delta(\omega_g(s)T_g(s)) \end{bmatrix}. \quad (5.14)$$

Because the complexity of the PID design process is highly dependent on the number of PID controllers used, we elect not to design any controllers for the nacelle yaw input, as its restrictive actuator limitations make it a relatively ineffective choice for control. The block diagram for the overall PID feedback structure is shown in Figure 5.2. The six controllers were designed by following a three step process.

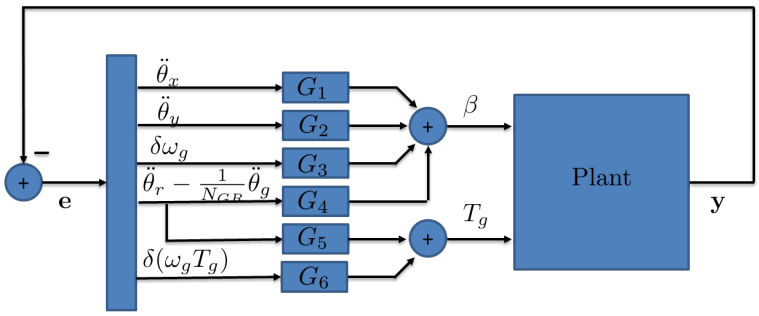

Figure 5.2: PID Block Diagram.

Step 1: Independent Design The first step was to design each controller independently, using the linear model and a process similar to the Ziegler-Nichols tuning formula [41]. Since each output requires regulation, the controllers were tuned for the response to a 1m/s step increase in wind speed, such that the following conditions were met:

- Settling time as fast as possible
- Zero steady state error
- Actuator limits obeyed

Once each controller is tuned, we move on to Step 2.

Step 2: Collective Design With each controller set, the step response is repeated for the linear model with all controllers enabled. Since the controllers are either competing or collaborating for each control input, the independent controller criterion from Step 1 are no longer satisfied. Each controller, then, is tuned once again such that the collection satisfies all the criterion.

Step 3: Non-Linear Implementation Finally, the controller is applied to the full non-linear simulation, as described in Section 5.2. Once again, the conditions are closely monitored and any tunings necessary are made to the controllers such that the criterion are met.

This concludes the design process for the PID controller. The final values obtained after following this process are shown in Appendix B. Next, the LQR controller is examined.

5.4 Design of the LQR Controller with Integrator

The LQR state-feedback controller, which is introduced and described in [42], is very common in literature for the control of floating offshore wind turbines [5],[27],[24],[25]. It is a natural choice because, unlike the PID where each input/output combination is tuned independently by the operator, in the LQR all such combinations are tuned simultaneously. Furthermore, the process is automated and guaranteed to be optimal, with respect to the weighting scheme chosen by the operator. Since the LQR is a state-feedback controller, a state-observer is necessary to acquire the non-measurable states. In the next subsections, the LQR controller and the observer will be presented in order.

5.4.1 LQR with an Integrator

Traditionally, LQR controllers regulate only the states of the plant. In order to also regulate the outputs and eliminate steady-state-error, an integrator is added to the customary state-feedback structure. The full feedback structure, that is state-feedback plus output error integration is shown in Figure 5.3. Here, $\underline{\mathrm{K}}_a$ and $\underline{\mathrm{K}}$ are the integrator and state-feedback gains, re-

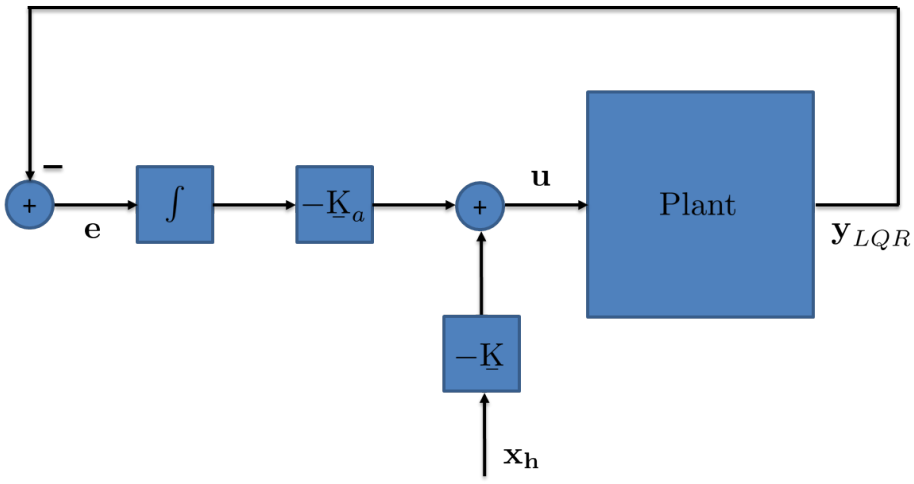

Figure 5.3: LQR Block Diagram.

spectively, and $\mathbf{x_h}$ is the full estimated state vector from the state-observer. The matrices $\underline{\mathrm{K}}_a$ and $\underline{\mathrm{K}}$ can be solved for simultaneously using a traditional LQR cost function by stacking the usual state vector with the output vector. The cost function to be minimized, then, is

$$J = \int_0^\infty (\mathbf{z}^T \underline{\mathrm{Q}} \mathbf{z} + \mathbf{u}^T \underline{\mathrm{R}} \mathbf{u}) dt, \tag{5.15}$$

where the augmented state vector z is given by

$$z = \begin{bmatrix} \mathbf{x} \\ \mathbf{y}_{LQR} \end{bmatrix}, \tag{5.16}$$

and the augmented state weighting matrix Q is the diagonal matrix

$$\underline{\mathrm{Q}} = \begin{bmatrix} \underline{\mathrm{Q}}_x & \\ & \underline{\mathrm{Q}}_y \end{bmatrix}. \tag{5.17}$$

Here, $\underline{\mathrm{Q}}_x$ and $\underline{\mathrm{Q}}_y$ represent the weighting matrices for the states and outputs, respectively. Furthermore, because the position states of $\mathbf{y}$ are included in $\mathbf{x}$, the LQR output vector $\mathbf{y}_{LQR}$ consists of only the latter five components of $\mathbf{y}$. The cost function in (5.15) can be minimized using the function `LQI.m` in Matlab. The initial weighting values were intuitively selected with the goal of normalization with respect to an arbitrarily selected state, state 1. For example, we say one meter of surge is equally weighted to one degree of platform pitch rotation, which is equivalent to 1 degree of blade pitch. Then, the initial weightings for surge, pitch and blade pitch are 1, $180/\pi$, and 1, respectively. Finally, through simulations, the weighting values are iteratively adjusted until we have minimized fatigue-related loads and power fluctuation as much as possible, while staying within our actuator limits. The diagonal values of the final state and output weighting functions, and

input weighting function are

$$\underline{\mathrm{Q}}_x = \mathrm{diag}\begin{bmatrix} 1 \\ 1 \\ 0 \\ 1.05\mathrm{e}1 \\ 1.05\mathrm{e}1 \\ 0 \\ 1.75\mathrm{e}\text{-}2 \\ 1\mathrm{e}\text{-}1 \\ 1\mathrm{e}\text{-}1 \\ 0 \\ 1.75\mathrm{e}\text{-}3 \\ 1.75\mathrm{e}\text{-}3 \\ 0 \\ 1\mathrm{e}\text{-}1 \\ 1.03\mathrm{e}\text{-}3 \end{bmatrix}, \quad \underline{\mathrm{Q}}_y = \mathrm{diag}\begin{bmatrix} 1.75\mathrm{e}\text{-}4 \\ 1.75\mathrm{e}\text{-}4 \\ 1.8\mathrm{e}\text{-}5 \\ 1.19\mathrm{e}8 \\ 1\mathrm{e}\text{-}6 \end{bmatrix}, \quad \underline{\mathrm{R}} = \mathrm{diag}\begin{bmatrix} 1\mathrm{e}3 \\ 1\mathrm{e}{-1} \\ 1\mathrm{e}6 \end{bmatrix}, \tag{5.18}$$

and the final controller gains are given in Appendix B.

5.4.2 Reduced-order Observer

For the LQR controller, it is necessary to have a real-time estimate $\mathbf{x_h}$ for all the states $\mathbf{x}$ of the system. This can be accomplished either with a full-order state-observer, which estimates the measured and unmeasured states, or a reduced-row observer for estimation of only the unmeasured states [43]. It was clear, after implementing both, that the reduced-row observer was more accurate in predicting the unmeasured states. Therefore, the reduced-row observer was selected. The block diagram of the observer is shown in Figure 5.4. Here, $\underline{\mathrm{P}}$ is the transformation matrix that separates the measurable states $\mathbf{x_m}$ and unmeasurable states $\mathbf{x_u}$, such that

$$\begin{bmatrix} \mathbf{x_m} \\ \mathbf{x_u} \end{bmatrix} = \underline{\mathrm{P}}\mathbf{x}. \tag{5.19}$$

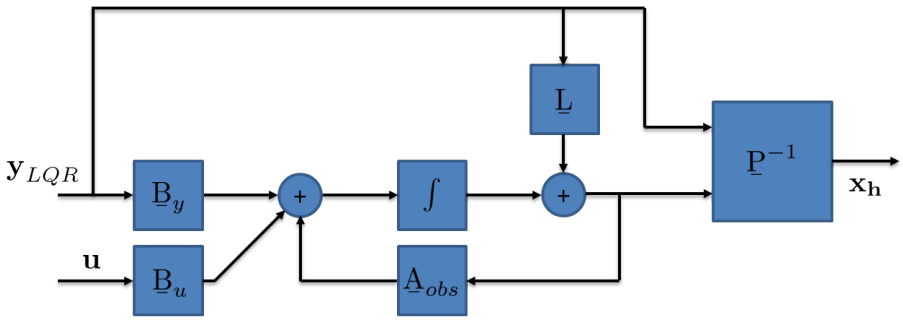

Figure 5.4: Reduced Row Observer Block Diagram.

$\underline{\mathrm{P}}$ is chosen such that $\mathbf{x_m}$ consists of all the platform position and orientation states, the rotor flexibility state and the generator speed, and $\mathbf{x_u}$ consists of the platform velocity and angular velocity states, as well as the rotor speed. $\underline{\mathrm{L}}$ is the observer gain, and the remaining matrices $\underline{\mathrm{B}}_y$, $\underline{\mathrm{B}}_u$, and $\underline{\mathrm{A}}_{obs}$ can be found by following the procedure for a continuous-time reduced order observer in [44]. Using the transformation $\underline{\mathrm{P}}$, we can re-express the linear state-space model as

$$\frac{d}{dt}\begin{bmatrix}\mathbf{x_m}\\ \mathbf{x_u}\end{bmatrix} = \underline{\mathrm{P}}\underline{\mathrm{A}}\underline{\mathrm{P}}^{-1}\begin{bmatrix}\mathbf{x_m}\\ \mathbf{x_u}\end{bmatrix} + \underline{\mathrm{P}}\underline{\mathrm{B}}\mathbf{u}, \tag{5.20}$$

or equivalently

$$\frac{d}{dt}\begin{bmatrix}\mathbf{x_m}\\ \mathbf{x_u}\end{bmatrix} = \begin{bmatrix}\tilde{\underline{\mathrm{A}}}_{11} & \tilde{\underline{\mathrm{A}}}_{12}\\ \tilde{\underline{\mathrm{A}}}_{21} & \tilde{\underline{\mathrm{A}}}_{22}\end{bmatrix}\begin{bmatrix}\mathbf{x_m}\\ \mathbf{x_u}\end{bmatrix} + \begin{bmatrix}\tilde{\underline{\mathrm{B}}}_1\\ \tilde{\underline{\mathrm{B}}}_2\end{bmatrix}\mathbf{u}. \tag{5.21}$$

Finally, $\underline{\mathrm{L}}$ is designed by pole placement of the system $\tilde{\underline{\mathrm{A}}}_{22} - \underline{\mathrm{L}}\tilde{\underline{\mathrm{A}}}_{12}$. For the proposed observer, we use poles $\{-10, -10.5, -11, -11.5, -12, -12.5, -13\}$,. The final observer matrix $\underline{\mathrm{L}}$ is given in Appendix B.

5.5 Design of the H_∞ with Integrator

The H_∞ method is well suited for multi-objective control problems and disturbance rejection, particularly when the disturbance frequency properties

are well known. Although H_∞ control has been applied to onshore wind turbines [45, 46], it remains far less explored for offshore turbines. For an introduction and overview of H_∞ control, see [47], and for a good introduction on selecting weighting functions see [48]. The authors of [11] were able to utilize the known frequency properties of wind and wave for disturbance rejection in their H_∞ controller for a 2-D wind turbine system with success, however as was explained in Chapter 2, this could only be done for unrealistic 2-D motion. This section will explain the methods used to derive the proposed disturbance rejecting H_∞ controller.

A general block diagram for the H_∞ feedback loop is shown in Figure 5.5. Here, $\underline{\mathrm{K}}_\infty$ is the dynamic H_∞ controller, and $\underline{\mathrm{W}}_v$, $\underline{\mathrm{W}}_w$, $\underline{\mathrm{W}}_u$ and $\underline{\mathrm{W}}_e$ are the weighting functions for wind, wave, control inputs and outputs, respectively. All the weighting functions can be either constant or frequency dependent, but generally we select $\underline{\mathrm{W}}_u$ and $\underline{\mathrm{W}}_e$ as constant gains to balance actuator usage and reference tracking, and $\underline{\mathrm{W}}_v$ and $\underline{\mathrm{W}}_w$ as frequency dependent, for disturbance rejection. We also define the augmented plant $\underline{\mathrm{P}}_{aug}$ as the linear

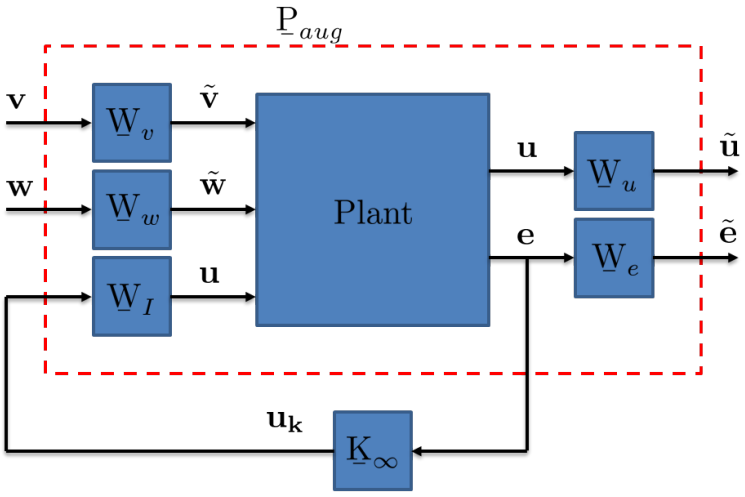

Figure 5.5: H_∞ Block Diagram.

transformation

$$\left[\begin{array}{c} \dot{\mathbf{x}}_{\mathbf{aug}} \\ \hline \tilde{\mathbf{e}} \\ \tilde{\mathbf{u}} \\ \hdashline \mathbf{e} \end{array}\right] = \underline{\mathrm{P}}_{aug} \left[\begin{array}{c} \mathbf{x}_{\mathbf{aug}} \\ \hline \mathbf{v} \\ \mathbf{w} \\ \hdashline \mathbf{u_k} \end{array}\right], \tag{5.22}$$

where $\mathbf{u_k}$ represents the controller outputs, $\mathbf{e}$ the measured outputs, $\tilde{\mathbf{u}}$ and $\tilde{\mathbf{e}}$ the minimization variables, and $\mathbf{x_{aug}}$ the augmented state vector. As we will see, it is convenient to decompose this augmented plant into a state-space system as

$$\underline{\mathrm{P}}_{aug} = \left[\begin{array}{c|c} \underline{\mathrm{A}}_{aug} & \underline{\mathrm{B}}_{aug} \\ \hline \underline{\mathrm{C}}_{aug} & \underline{\mathrm{D}}_{aug} \end{array}\right]. \tag{5.23}$$

Identifying the components of this matrix $\underline{\mathrm{P}}_{aug}$ will be key to synthesizing an H_∞ controller, however before we can do so we must first define the weighting functions.

5.5.1 Integrator

To eliminate steady-state-error, we can force the augmented plant to have an integrator. We do this by splitting the actuator input $\mathbf{u}$ into two parts, the proportional part $\mathbf{u_P}$ and the integrated part $\mathbf{u_I}$ such that $\mathbf{u} = \mathbf{u_P} + \frac{\mathbf{1}}{\mathbf{s}}\mathbf{u_I}$. We also need to define a new state $\mathbf{x_I}$ for the augmented plant which is given by

$$\dot{\mathbf{x}}_I = (-\epsilon I)\mathbf{x_I} + \mathbf{u_I}. \tag{5.24}$$

Here, ϵ is simply a very small scalar which is necessary for numerical stability of the augmented plant, and $\underline{\mathrm{I}}$ is the identity matrix. Graphically, the integrator system is shown in Figure 5.6.

5.5.2 Weighting Selection

Many weighting function combinations were considered in the design of the H_∞ controller. Constant weighting functions $\underline{\mathrm{W}}_u$ and $\underline{\mathrm{W}}_e$ were determined iteratively to give a good balance between output tracking and control input.

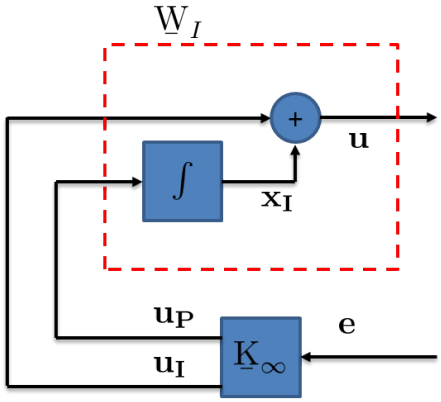

Figure 5.6: H_∞ Integrator Block Diagram.

In the end, the values we used were

$$\underline{\mathrm{W}}_e = \mathrm{diag}[0, \ldots, 0, 0.00396, 0.00726, 8.0617, 0.199, 9.698], \quad (5.25)$$

$$\underline{\mathrm{W}}_u = \mathrm{diag}[10, 0.2, 2]. \quad (5.26)$$

For the frequency-dependent weighting functions $\underline{\mathrm{W}}_v$ and $\underline{\mathrm{W}}_w$, we were careful not to use too many different transfer functions, as each one adds an additional state to the augmented plant. It was determined through experimentation that the most significant wave disturbance was the z-component of wave acceleration, which caused large platform roll and pitch motions. Thus, we designed three identical weighting functions to reject the vertical wave acceleration at each of the outer columns. Using the ocean wave spectrum from Figure 3.20, and with the goal of attenuating frequencies below the apparent cut-off of 1 rad/s, we came to the weighting function

$$\underline{\mathrm{W}}_{w,a_z} = \frac{1.1s + 0.01146}{s + 11.46}. \quad (5.27)$$

The overall wave disturbance weighting matrix $\underline{\mathrm{W}}_w$, then, is a 36x36 diagonal matrix where all the elements have value 1 except those in rows 6, 15, and 24, which have value $\underline{\mathrm{W}}_{w,a_z}$. These three rows correspond to the z-component wave acceleration disturbances at each of the outer columns. Finally, we

can convert the weighting matrix $\underline{\mathrm{W}}_w$ to state space form for compatibility with our augmented plant. This adds three additional states to the model, given by

$$\dot{\mathbf{x}}_w = \underline{\mathrm{A}}_{W,w}\mathbf{x_w} + \underline{\mathrm{B}}_{W,w}\mathbf{w}, \tag{5.28}$$

and the new weighted wave disturbance signal, which is given by

$$\tilde{\mathbf{w}} = \underline{\mathrm{C}}_{W,w}\mathbf{x_w} + \underline{\mathrm{D}}_{W,w}\mathbf{w}. \tag{5.29}$$

The values of these four matrices have been omitted for brevity. The resulting closed-loop transfer functions between the first column's z-component wave acceleration and the platform roll and pitch outputs are shown in Figure 5.7. It is clear that attenuation is achieved below 1 rad/s. It is important to note that we can achieve further attenuation by using higher order weighting functions, however that comes at the cost of increasing the number of states of our augmented plant.

For the wind disturbance weighting function $\underline{\mathrm{W}}_v$, we choose not to add any additional states. That is, $\underline{\mathrm{W}}_v = I_{3\times 3}$. This decision was made for the purposes of this thesis to highlight the benefits of rejecting wave disturbance. In reality, wind spectrum frequency profiles are well understood, and rejecting major frequencies via the wind disturbance weighting function could prove to be very useful.

5.5.3 Final Structure

After applying all of the above-described weighting functions, we can combine the states from the wind turbine system with the integrator and wave disturbance weighting function states to form the augmented state vector $\mathbf{x_{aug}} = [\mathbf{x}, \mathbf{x_I}, \mathbf{x_w}]^\mathbf{T}$. Similarly, we can form the control output vector with the proportional and integrator terms, or $\mathbf{u_k} = [\mathbf{u_P}, \mathbf{u_I}]^\mathbf{T}$. It is easy to show

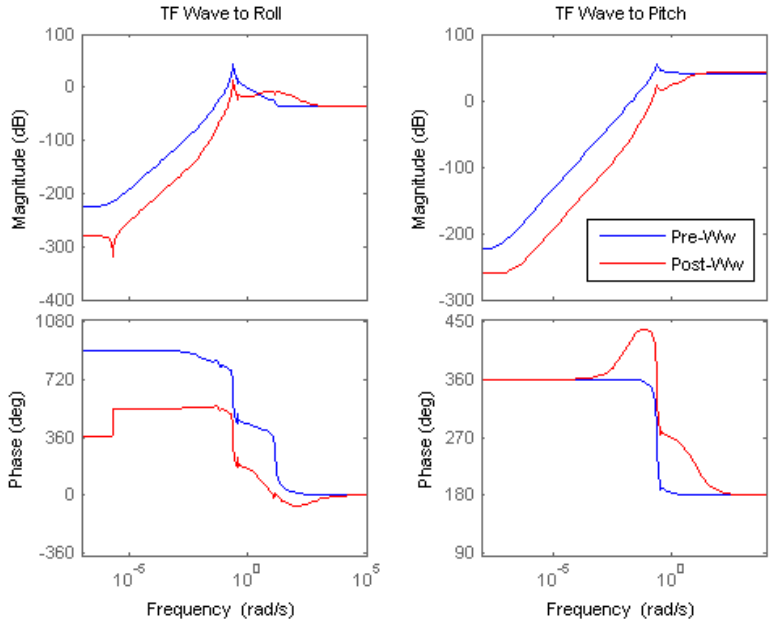

Figure 5.7: Closed-loop Transfer Function Between Wave Acceleration and Platform Motion.

that the four components of the augmented plant P_{aug} are given by

$$\underline{\mathrm{A}}_{aug} = \begin{bmatrix} \underline{\mathrm{A}} & \underline{\mathrm{B}} & \underline{\mathrm{B}}_w\underline{\mathrm{C}}_{W,w} \\ 0 & -\epsilon & 0 \\ 0 & 0 & \underline{\mathrm{A}}_{W,w} \end{bmatrix} \tag{5.30}$$

$$\underline{\mathrm{B}}_{aug} = \begin{bmatrix} \underline{\mathrm{B}}_v & \underline{\mathrm{B}}_w\underline{\mathrm{D}}_{W,w} & \underline{\mathrm{B}} & 0 \\ 0 & 0 & 0 & \underline{\mathrm{I}} \\ 0 & \underline{\mathrm{B}}_{W,w} & 0 & 0 \end{bmatrix} \tag{5.31}$$

$$\underline{\mathrm{C}}_{aug} = \begin{bmatrix} -\underline{\mathrm{W}}_e\underline{\mathrm{C}} & -\underline{\mathrm{W}}_e\underline{\mathrm{D}} & -\underline{\mathrm{W}}_e\underline{\mathrm{D}}_w\underline{\mathrm{C}}_{W,w} \\ 0 & \underline{\mathrm{W}}_u & 0 \\ -\underline{\mathrm{C}} & -\underline{\mathrm{D}} & -\underline{\mathrm{D}}_w\underline{\mathrm{C}}_{W,w} \end{bmatrix} \tag{5.32}$$

$$\underline{\mathrm{D}}_{aug} = \begin{bmatrix} -\underline{\mathrm{W}}_e\underline{\mathrm{D}}_v & -\underline{\mathrm{W}}_e\underline{\mathrm{D}}_w\underline{\mathrm{D}}_{W,w} & -\underline{\mathrm{W}}_e\underline{\mathrm{D}} & 0 \\ 0 & 0 & \underline{\mathrm{W}}_u & 0 \\ -\underline{\mathrm{D}}_v & -\underline{\mathrm{D}}_w\underline{\mathrm{D}}_{W_w} & -\underline{\mathrm{D}} & 0 \end{bmatrix} \tag{5.33}$$

Finally, with the defined augmented plant, we can use the Matlab function `hinfsyn.m`, to find the controller system $\underline{\mathrm{K}}_\infty$ that both stabilizes the closed-loop system from Figure 5.5 and minimizes the infinity norm of the resulting transformation from inputs to outputs of the system. The ensuing controller $\underline{\mathrm{K}}_\infty$ is given in Appendix B.

5.6 Design of the H_∞ Controller with Feedforward Terms

The design process for the feedforward H_∞ controller is largely the same as the disturbance rejecting H_∞ controller, but with two major differences. First, we elect not to use the wave disturbance weighting function that was used in the alternate H_∞ controller. Second, we add two disturbance measurements to the augmented plant outputs.

5.7 Weighting Selection

The constant weighting functions $\underline{\mathrm{W}}_u$ and $\underline{\mathrm{W}}_e$ were once again determined iteratively to balance output tracking and control input. The final values used were

$$\underline{\mathrm{W}}_e = \mathrm{diag}[0, \ldots, 0, 0.32, 0.61, 1.18e4, 25.73, 9.32], \tag{5.34}$$

$$\underline{\mathrm{W}}_u = \mathrm{diag}[10000, 200, 2000]. \tag{5.35}$$

5.7.1 Identification of the Feedforward Terms

For feedforward control, we make use of two disturbance measurements; relative wind velocity, and heave pressure. Heave pressure can be measured by placing a pressure sensor at the bottom of each column of the semi-

submersible platform, and wind velocity can be either measured with lidar technology [49], or estimated with a disturbance estimator [24].

The heave pressure is the total pressure acting on the heave surface, which we assume is the total hydrodynamic force acting perpendicular to the heave plate, divided by the plate area. From Chapter 3, we can formulate the mathematical expression as

$$P_i = \frac{1}{A_i}[\ 0 \quad 0 \quad 1\ ]\underline{\mathrm{R}}^T \vec{F}_{Dh,i}, \tag{5.36}$$

where the heave force $\vec{F}_{Dh,i}$ on each plate i is given by

$$\vec{F}_{Dh,i} = K_{dh,i}||\vec{v}_{h,i}||\vec{v}_{h,i} + K_{ah,i}\vec{a}_{h,i} + P_i A_i \hat{e}_h. \tag{5.37}$$

Using the linearization process described in the Chapter 4, we can generate a linear expression for the pressure P as a function of the system states and the wave disturbance, or

$$\delta P = \underline{\mathrm{C}}_P \mathbf{x} + \underline{\mathrm{D}}_{P,w} \mathbf{w} \tag{5.38}$$

The relative wind velocity is simply the relative speed between the wind and the rotor, in a direction perpendicular to the rotor plane. This is given by

$$v_r = ||\vec{v}_n||, \tag{5.39}$$

where $||\vec{v}_n||$ is described in Chapter 3. Again, we linearize the formulation at the equilibrium point, which gives the expression

$$\delta v_r = \underline{\mathrm{C}}_{v_r} \mathbf{x} + \underline{\mathrm{D}}_{v_r} \mathbf{u} + \underline{\mathrm{D}}_{v_r,v} \mathbf{v}. \tag{5.40}$$

5.7.2 Final Structure

The final structure for the augmented plant is given by

$$\begin{bmatrix} \dot{\mathbf{x}} \\ \dot{\mathbf{x}}_i \\ \hline \tilde{\mathbf{e}} \\ \tilde{\mathbf{u}} \\ \hline \mathbf{e} \\ P \\ v_r \end{bmatrix} = \left[\begin{array}{cc|ccc|cc} \underline{A} & \underline{B} & \underline{B}_v & \underline{B}_w & \underline{B} & 0 \\ 0 & -\epsilon & 0 & 0 & 0 & \underline{I} \\ \hline -\underline{W}_e\underline{C} & -\underline{W}_e\underline{D} & -\underline{W}_e\underline{D}_v & -\underline{W}_e\underline{D}_w & -\underline{W}_e\underline{D} & 0 \\ 0 & \underline{W}_u & 0 & 0 & \underline{W}_u & 0 \\ \hline -\underline{C} & -\underline{D} & -\underline{D}_v & -\underline{D}_w & -\underline{D} & 0 \\ \underline{C}_P & 0 & 0 & \underline{D}_{P,w} & 0 & 0 \\ \underline{C}_{v_r} & \underline{D}_{v_r} & \underline{D}_{v_r,v} & 0 & \underline{D}_{v_r} & 0 \end{array}\right] \begin{bmatrix} \mathbf{x} \\ \mathbf{x_i} \\ \hline \mathbf{v} \\ \mathbf{w} \\ \hline \mathbf{u_P} \\ \mathbf{u_I} \end{bmatrix}. \tag{5.41}$$

Once again, we use the Matlab function `hinfsyn.m` to solve for a controller $\underline{K}_\infty$, which is given in Appendix B.

5.8 Controller Comparison Results

In this section, the results are shown and explained for each controller individually, and then all together at the end.

5.8.1 PID vs Baseline GSPI

The multi-objective PID (MOPID) results can be compared against the baseline GSPI described in [18] and updated for the semi-submersible platform in [1]. This GSPI controller is a constant torque, collective blade pitch controller whose sole objective is rotor speed regulation (and by consequence, power regulation) via blade pitch actuation. The authors do not use platform motion for feedback, instead they choose their controller gains such that the controller does not excite the natural frequencies of the platform motions.

The normalized performance metrics, for the MOPID compared to the GSPI are shown in Figure 5.8. It is clear that the MOPID achieves drastically reduced drivetrain loads and improved power regulation compared to the baseline GSPI, with a 50.1% and 60.4% improvement in rotor speed

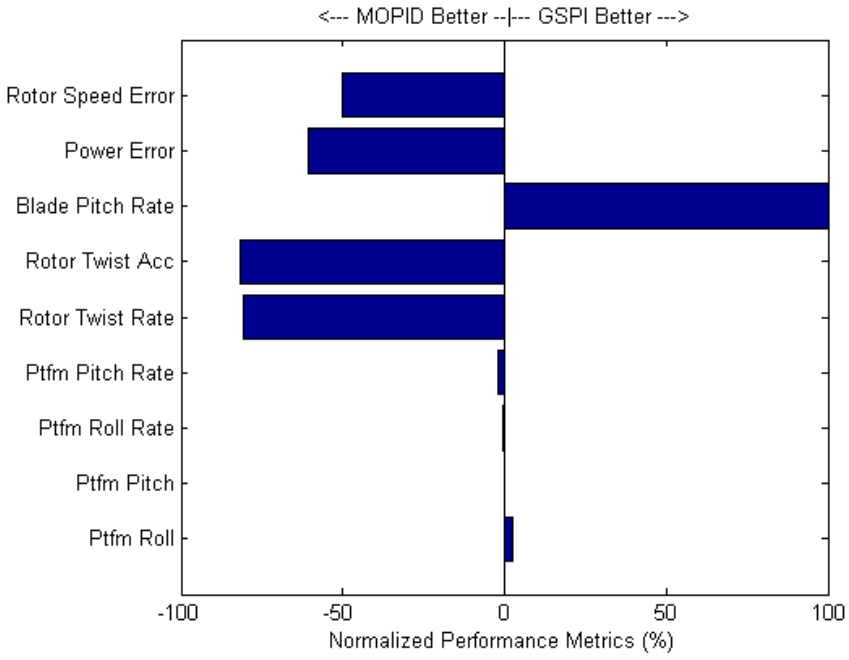

Figure 5.8: GSPI vs MOPID

and power error, respectively, and a 81.6% and 80.8% improvement in rotor twist acceleration and velocity, respectively. The improvements come at a 2995% increase, however, in blade pitch rate. It is explained in [16] that the baseline GSPI, which was originally designed for an onshore wind turbine, had its gains significantly reduced for its offshore implementation because of excitation of the platform roll and pitch natural frequencies. In other words, the desired, much higher, gain values for the baseline GSPI were not possible because of the single-input, single-output design choice. In the MOPID, this is not a problem, as minimization of these platform motions are control objectives and as can be seen in Figure 5.8, the platform motions for the MOPID controller are similar to those for the reduced-gain GSPI, even with the increased blade pitch rate. Furthermore, we verify that the RMS blade pitch rate of 6.6 deg/s is well below the actuator limit of 8 deg/s, which corresponds to the blade pitch actuator spending about 5.8% of the total

simulation time at its maximum rate.

5.8.2 LQR vs PID

While the input-output relationships have to be carefully selected by the user to balance design complexity and controller performance in the PID design process, the LQR process is an automated approach that utilizes all possible input-output relationships. Of course this requires a linear state-space model containing all such relationships. The designed LQR controller is compared to the MOPID, and the results are shown in Figure 5.9. The

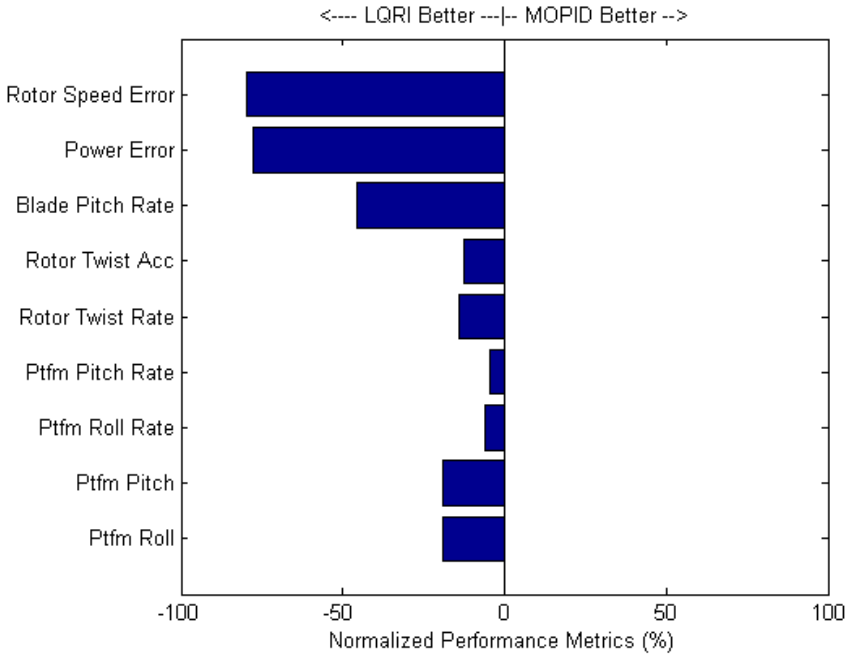

Figure 5.9: MOPID vs LQR

results suggest a 80.0% and 77.7% improvement in rotor speed and power error, as well as a 45.8% decrease in blade pitch rate. Similarly, we also see improvements in platform motion, with a 19% and 19.2% reduction in roll and pitch, respectively, and a 5.8% and 4.3% reduction in roll and pitch rates, respectively. Finally we see a 14.2 and 12.7% reduction in rotor twist

rate and acceleration, respectively. This drastic increase in performance can likely be attributed to the complex, coupled relationships between the states and inputs of the wind turbine system. In the PID case, we had to restrict feedback to only the most obvious input-output relationships. As a result, we probably missed some important coupled phenomena, such as the effect of generator torque on platform motion.

5.8.3 H_∞ vs LQR

Like the LQR controller, the H_∞ controller is designed based on all input-output relationships. It also takes into account the disturbance relationships, and through loop-shaping, can reject said disturbances based on their expected frequency profiles. The designed H_∞ controller is compared to the LQR, and the results are shown in Figure 5.10. Here, we see further improve-

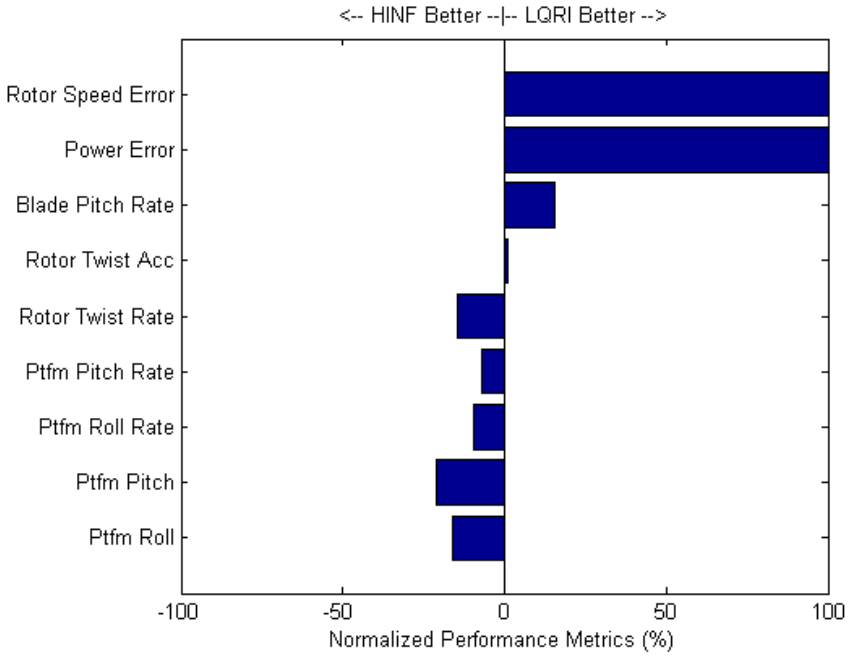

Figure 5.10: LQR vs H_∞

ments in fatigue minimization performance metrics, however this comes at

a cost to power and rotor speed error and blade pitch usage. Specifically, we see a 16.0% and 21.0% improvement in platform roll and pitch, and a 9.4% and 6.9% improvement in platform roll and pitch rates. We also see a 14.3% improvement in rotor twist rate, but a 1.1% increase in rotor twist acceleration. Finally, we see a 15.6% increase in blade pitch usage, and a 166% and 151% increase in rotor speed and power error. It should be noted, however, that the rotor speed and power error for the H_∞ controller is still 76% and 75% lower than in the baseline GSPI controller, and 40% and 49% lower than the MOPID controller, respectively. The overall comparisons will be further described in Subsection 5.8.5. The improvements shown here for platform motions and drivetrain loads can be attributed to the disturbance rejection capabilities of the H_∞ controller.

5.8.4 H_∞ with Feedforward vs H_∞

Under the H_∞ framework, it is very easy to add feed-forward signals to the feedback loop, provided that such signals are measurable, and increase the performance capabilities of the controller. The results for the H_∞ feed-forward controller compared to the disturbance rejecting H_∞ controller are shown in Figure 5.11. Using such a controller, we achieve a 53% decrease in power error and a 16% decrease in rotor speed, at a 3% cost to blade pitch usage. These power and rotor side improvements can largely be attributed to the preview information about the wind speed, which allows the controller to react to changing wind speeds before the rotor speed does. Platform pitch and roll rates, and the rotor twist metrics remain largely unchanged compared to the H_∞ controller, however platform roll and pitch metrics increase by 10% and 17%, respectively. Overall, the H_∞ feed-forward controller allows for similar improvements in fatigue minimization as the H_∞ controller, while recovering much of the power regulation capability.

5.8.5 Overall Controller Comparison

The results for all of the above-described controllers compared to the baseline GSPI controller are shown in Figure 5.12. Here, a value less than one

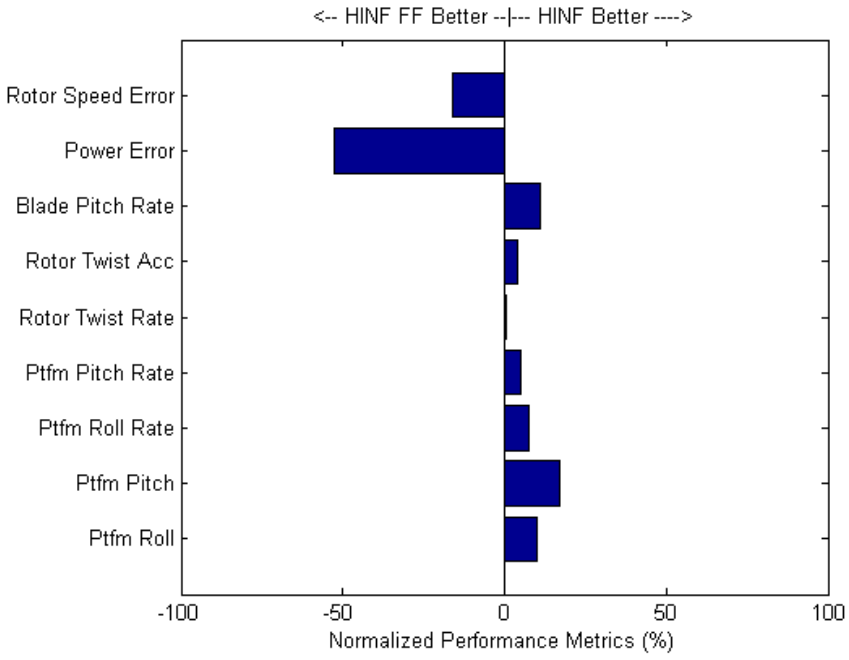

Figure 5.11: H_∞ vs H_∞ FF

represents an improvement in the respective performance metric compared to the baseline PID. Channels 1 through 9 are the same as above or, in order: platform roll (1) and pitch (2), platform roll and pitch rate (3 and 4), rotor twist rate (5) and acceleration (6), blade pitch rate (7), power error (8) and rotor speed error (9). Non-normalized magnitudes of the performance parameters for each controller validation test are also given in Table 5.1, below. It is clear that the floating wind turbine system benefits greatly from model-based, multi-objective controllers such as the LQR, H_∞ and H_∞ feed-forward. Furthermore, methods that use the wind and wave disturbance information, either through loop-shaping or feed-forward, can significantly reduce platform motions and drivetrain loads, compared even to other multi-objective methods.

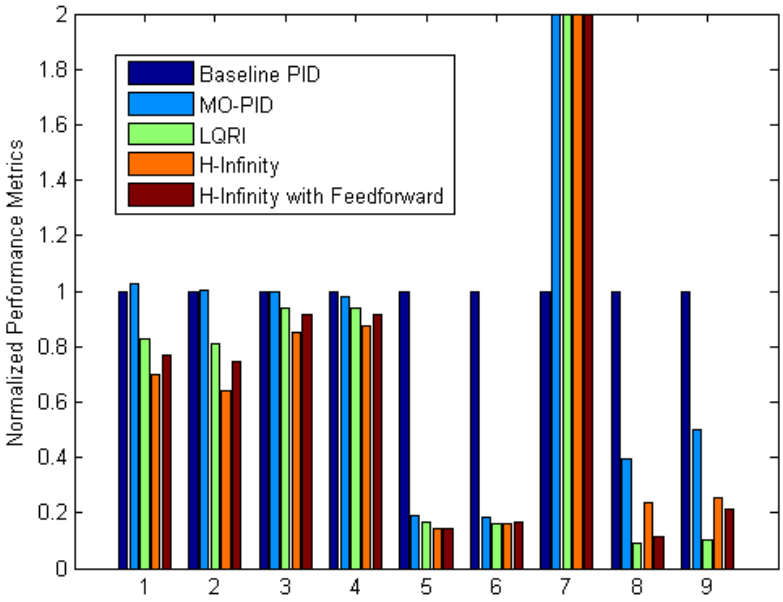

Figure 5.12: Overall Controller Comparison

5.9 Summary

In this chapter, we used the linear model derived in Chapter 4 to construct several multi-objective controllers with the goal of regulating power capture and major platform motions. The controllers include a PID controller, an optimal LQR controller, with integrator and observer, and two H_∞ controllers, one with wave disturbance rejection and the other with disturbance feedforward. After designing each of the controllers, we compared their performance with respect to one another, and to a baseline gain-scheduling controller created by the makers of advanced simulation software FAST.

The goal of this section was both to reinforce the notion that multi-objective control is necessary for the success of floating offshore wind turbine systems and, more importantly, that consideration of disturbance can significantly enhance controller performance. Through closed-loop simulations of the four increasingly complex controllers, we showed these two statements

Performance Parameter	GSPI	MOPID	LQRI	H_∞	H_∞ FF
Platform Roll (rad)	7.16e-03	7.34e-03	5.94e-03	4.99e-03	5.75e-03
Platform Pitch (rad)	1.48e-02	1.48e-02	1.19e-02	9.43e-03	1.11e-02
Platform Roll Rate (rad/s)	2.38e-03	2.38e-03	2.24e-03	2.03e-03	2.09e-03
Platform Pitch Rate (rad/s)	5.52e-03	5.42e-03	5.18e-03	4.83e-03	4.71e-03
Rotor Twist Rate (rad/s)	7.72e-03	1.48e-03	1.27e-03	1.09e-03	1.10e-03
Rotor Twist Acc (rad/s^2)	1.02e-01	1.87e-02	1.63e-02	1.65e-02	1.72e-02
Blade Pitch Rate (deg/s)	2.13e-01	6.58e+00	3.57e+00	4.12e+00	4.57e+00
Power Error (MW)	4.50e-01	1.78e-01	3.99e-02	1.06e-01	5.00e-02
Rotor Speed Error (rad/s)	1.11e+01	5.51e+00	1.11e+00	2.79e+00	2.31e+00

Table 5.1: Performance Results from Controller Validation Tests.

to be true. Specifically, we showed that controllers that utilize the derived wave disturbance matrix, either to reject the wave disturbance, or to predict the effects of wave disturbance through feedforward loops, are superior in terms of minimizing harmful motions and regulating power.

Chapter 6

Conclusion

6.1 Summary Remarks

This thesis proposes a simple physics-based control-oriented model for floating offshore wind turbines that aims to facilitate the design of advanced controllers. Using such a model provides several key advantages existing methods, which were highlighted in each of the chapters of this text.

In Chapter 3, we presented the simplified non-linear model for the floating wind turbine, which was derived from first principles. The general model has up to 15 or 16 states, 3 control inputs, 3 wind disturbance signals, and 9 wave disturbance signals for each major buoyant column or platform. This general model was then applied to a sample floating wind turbine that had been well defined in research, and the specific force and torque models for the aerodynamics, the hydrodynamics and the mooring lines were described. Finally, the model was validated in four distinct tests that covered a large range of operating conditions for the highly non-linear system.

As a control-oriented model, it is of course very important to be able to generate accurate linear state-space models from the non-linear plant. In Chapter 4 we described how to solve for equilibrium points of the WTS using a simple iteration scheme and the partial derivatives of the non-linear function. Using said equilibrium points, a procedure for linearizing the model was given, and some minor, intuitive adjustments were made to increase its accuracy. Finally, we used the realistic open-loop test defined in Chapter 3 to compare the linear model to the complex simulator FAST, as well as a high state FAST-linearized model.

Next, in Chapter 5, we designed several controllers using the proposed model. The controllers included a multi-objective PID controller, an LQR

controller with an integrator and reduced-order observer, a wave disturbance rejecting H_∞ controller, and a wave disturbance feedforward H_∞ controller. These controllers were then compared to one another, and to a baseline gain-scheduled PID controller developed by the makers of FAST. In the first comparison, we showed that the proposed PID controller greatly outperformed the baseline GSPI controller in rotor speed and power errors, and in drivetrain loads, but had relatively minor impact on platform motions. This increase in performance was attributed to the fact that the GSPI controller, which only uses generator speed for feedback, had to be detuned to avoid exciting resonances in the drivetrain and tower. The next comparison showed that the proposed LQR controller outperformed the proposed PID controller in every performance metric. Most importantly, it was able to greatly reduce platform motions, reducing tower fatigue loading. The wave disturbance rejecting H_∞ controller was able to further reduce drivetrain and platform motions, but at the cost of higher rotor speed and power fluctuation compared to the LQR controller. These fluctuation were still considerably less than those of the PID and baseline PI controllers. Finally, the H_∞ feedforward controller performed in between the other H_∞ controller and the LQR controller. From these results, we concluded that because of the complex coupling of the WTS, controllers with more information about the dynamics of the system, such as LQR and H_∞ controllers, are better suited for this particular problem. More importantly, controllers that can utilize information about the wind and wave disturbances, are superior. The non-linear model proposed in this thesis offers the ability to incorporate wave disturbance both directly (through feedforward), or indirectly (through rejection) thanks to the ability to generate the disturbance matrix in the linear model.

6.2 Contributions

The main contribution of this thesis is the development of the simplified, physics-based, control-oriented model of a floating wind turbine system. This model facilitates the creation of advanced controllers that are necessary for improving fatigue life of floating wind turbines while maximizing power

capture. More specific realizations of the contributions are listed below:

- An accurate non-linear model that is based on physical parameters that can easily be adjusted for different wind turbine systems, and for experimenting with mechanical design. Higher complexity simulators, which consider high order dynamics at a cost to complexity, also require considerable effort in changing mechanical parameters.

- A model that maintains its accuracy throughout the highly non-linear operating range for wind turbine systems, and can be linearized analytically at any point within this range for controller design. Most simple models used in existing research are based on parameter identification of complex simulators. This type of fitting must be done for each operating point, and is subject to high-order dynamical influence.

- A method to solve for equilibrium points of the system, which can be a very long and tedious process when using high complexity simulators. This method can also be extended to other useful tasks such as finding the moveable range of the wind turbine at a particular power capture level for wind farm optimization

- A method of obtaining the B_w disturbance matrix, which is currently not available in research. This disturbance matrix can be used for disturbance rejection or for feedforward control to greatly improve controller performance

- The generation of several advanced controllers for the baseline 5MW wind turbine described by the National Renewable Energy Laboratory. These controllers include a multi-objective PID controller, an LQR controller with an integrator and reduced-order observer, an H_∞ controller that rejects waves within its estimated energy spectrum, and finally a feedforward H_∞ controller that uses available wind and wave information to improve performance

6.3 Future Work

Control of offshore wind turbines continues to be an important role in reducing the cost of wind energy and making it a top competitor in the energy market. The research presented in this thesis can be extended to the following areas:

Combined Mechanical and Control Design of Floating Wind Turbines Since the proposed model is based on physical parameters, and since it can accurately predict the major motions of floating wind turbines systems, it is possible to collaboratively adjust the mechanical and controls properties of the system to optimize coupled parameters such as closed loop natural frequencies and stability.

Non-Linear Model Extensions Several possibilities for improvement of the non-linear model exist, including adding additional states such as blade or tower flexibility, adding additional inputs such as individual blade pitch control, and adding more complex behavior to the existing model such as skewed wake correction and other aerodynamic effects, or actuator dynamics. It was found in [50], for example, that the inclusion of actuator dynamics in the linear model greatly improved drivetrain performance for a simple PI controller. It should be deeply considered whether or not the increase in model complexity is worth the added accuracy, however.

Moveable Range and Wind Farm Optimization Because of the equilibrium point generation procedure outlined in this thesis, it would be possible to explore the effects of moving the individual floating wind turbines in a wind farm to optimize the combined power capture. This could also potentially reduce the large distances between turbines in the farm, decreasing the electrical interconnectivity costs.

LPV Control Finally, the nature of the simplified model, and the ease of generating equilibrium points makes it a strong candidate for LPV control.

Although LPV control is common for onshore wind turbines [51–53], it is a more difficult problem for offshore wind turbines because of platform motion. Still, some work has been done on LPV control for floating offshore wind turbines such as in [30] and [29]. The proposed model, however, would both facilitate the generation of linear models, and help to determine which analytical expression best fits the varying parameter relationship.

Bibliography

[1] A. Robertson, *Definition of the Semisubmersible Floating System for Phase II of OC4*, National Renewable Energy Laboratory, Golden, CO, Technical Report, NREL/TP-5000-60601, 2014.

[2] R. Wiser, *2013 Wind Technologies Market report*, U.S. Department of Energy, U.S., Technical Report, DOE/GO-102014-4459, 2014.

[3] A. Arapogianni, *Deep Water-The Next Step for Offshore Wind Energy.*, European Wind Energy Association, Brussels, Belgium, Technical Report, 978-2-930670-04-1, 2013.

[4] H. Namik, K. Stol, and J. Jonkman, "State-space control of tower motion for deepwater floating offshore wind turbines," in *Proceedings of the 46th AIAA Aerospace Sciences Meeting and Exhibit*, Reno, NV, p. 1307, 2008.

[5] H. Namik and K. Stol, "Individual blade pitch control of floating offshore wind turbines," *Wind Energy*, vol. 13, no. 1, pp. 74–85, 2010.

[6] J. S. González, A. G. G. Rodriguez, J. C. Mora, J. R. Santos, and M. B. Payan, "Optimization of wind farm turbines layout using an evolutive algorithm," *Renewable Energy*, vol. 35, no. 8, pp. 1671–1681, 2010.

[7] C. Elkinton, J. Manwell, and J. McGowan, "Algorithms for offshore wind farm layout optimization," *Wind Engineering*, vol. 32, no. 1, pp. 67–84, 2008.

[8] J. L. Rodriguez-Amenedo, S. Arnalte, and J. C. Burgos, "Automatic generation control of a wind farm with variable speed wind turbines,"

IEEE Transactions on Energy Conversion, vol. 17, no. 2, pp. 279–284, 2002.

[9] K. E. Johnson and N. Thomas, "Wind farm control: addressing the aerodynamic interaction among wind turbines," in *Proceedings of American Control Conference*, St. Louis, MO, pp. 2104–2109, 2009.

[10] B. Jonkman, *FAST User's Guide*, National Renewable Energy Laboratory, Golden, CO, Technical Report, NREL/EL-500-38230, 2005.

[11] G. Betti, M. Farina, G. A. Guagliardi, A. Marzorati, and R. Scattolini, "Development of a control-oriented model of floating wind turbines," *IEEE Transactions on Control Systems Technology*, vol. 22, no. 1, pp. 69–82, 2014.

[12] J. R. Homer and R. Nagamune, "Control-oriented physics-based models for floating offshore wind turbines," in *Proceedings of American Control Conference*, Chicago, IL, pp. 3696–3701, 2015.

[13] L. Y. Pao and K. E. Johnson, "Control of wind turbines," *IEEE Transactions on Control Systems Technology*, vol. 31, no. 2, pp. 44–62, 2011.

[14] G. van der Veen, I. Couchman, and R. Bowyer, "Control of floating wind turbines," in *Proceedings of American Control Conference*, Montreal,QC, pp. 3148–3153, 2012.

[15] O. Bagherieh and R. Nagamune, "Utilization of blade pitch control in low wind speed for floating offshore wind turbines," in *Proceedings of American Control Conference*, Portland, OR, pp. 4354–4359, 2014.

[16] J. M. Jonkman, *Influence of Control on the Pitch Damping of a Floating Wind Turbine*, National Renewable Energy Laboratory, Golden, CO, Technical Report, NREL/CP-500-42589, 2008.

[17] H. Namik and K. Stol, "Performance analysis of individual blade pitch control of offshore wind turbines on two floating platforms," *Mechatronics*, vol. 21, no. 4, pp. 691–703, 2011.

[18] J. Jonkman, *Definition of a 5-MW Reference Wind Turbine for Offshore System Development*, National Renewable Energy Laboratory, Golden, CO, Technical Report, NREL/TP-500-38060, 2009.

[19] J. M. Jonkman, *Dynamics Modeling and Loads Analysis of an Offshore Floating Wind Turbine*, National Renewable Energy Laboratory, Golden, CO, Technical Report, NREL/TP-500-41958, 2007.

[20] J. M. Jonkman, *Definition of the Floating System for Phase IV of OC3*, National Renewable Energy Laboratory, Golden, CO, Technical Report, NREL/TP-500-47535, 2010.

[21] D. Matha, *Model Development and Loads Analysis of an Offshore Wind Turbine on a Tension Leg Platform with a Comparison to Other Floating Turbine Concepts*, National Renewable Energy Laboratory, Golden, CO, Technical Report, NREL/SR-500-45891, 2010.

[22] A. N. Robertson and J. M. Jonkman, "Loads analysis of several offshore floating wind turbine concepts," in *Proceedings of The Twenty-first International Offshore and Polar Engineering Conference*, Maui, HI, pp. 443–450, International Society of Offshore and Polar Engineers, 2011.

[23] A. Myhr, C. Bjerkseter, A. Ågotnes, and T. A. Nygaard, "Levelised cost of energy for offshore floating wind turbines in a life cycle perspective," *Renewable Energy*, vol. 66, pp. 714–728, 2014.

[24] B. Skaare, T. D. Hanson, and F. G. Nielsen, "Importance of control strategies on fatigue life of floating wind turbines," in *Proceedings of 26th International Conference on Offshore Mechanics and Arctic Engineering*, San Diego, CA, pp. 493–500, 2007.

[25] S. Christiansen, T. Knudsen, and T. Bak, "Optimal control of a ballast-stabilized floating wind turbine," in *2011 IEEE International Symposium on Computer-Aided Control System Design*, Denver, CO, pp. 1214–1219, 2011.

[26] A. Cunha, E. Caetano, P. Ribeiro, and G. Müller, "Reducing blade fatigue and damping platform motions of floating wind turbines using model predictive control," in *Proceedings of the 9th International Conference on Structural Dynamics*, Porto, Portugal, pp. 3581–3588, 2014.

[27] S. Christiansen, T. Bak, and T. Knudsen, "Damping wind and wave loads on a floating wind turbine," *Energies*, vol. 6, no. 8, pp. 4097–4116, 2013.

[28] G. Betti, M. Farina, A. Marzorati, R. Scattolini, and G. Guagliardi, "Modeling and control of a floating wind turbine with spar buoy platform," in *Proceedings of 2012 IEEE International Energy Conference and Exhibition*, Florence, Italy, pp. 189–194, 2012.

[29] O. Bagherieh and R. Nagamune, "Gain-scheduling control of a floating offshore wind turbine above rated wind speed," *Control Theory and Technology*, vol. 13, no. 2, pp. 160–172, 2015.

[30] O. Bagherieh, *Gain-Scheduling Control of Floating Offshore Wind Turbines on Barge Platforms*, University of British Columbia, Vancouver, BC, MASc Thesis, 2013.

[31] E. Bossanyi, "Wind turbine control for load reduction," *Wind Energy*, vol. 6, no. 3, pp. 229–244, 2003.

[32] Y. A. Cengel, *Fluid Mechanics: Fundamentals and Applications*, McGraw Hill Publication, New York, NY, 2010.

[33] R. Wilson, "Wind-turbine aerodynamics," *Journal of Wind Engineering and Industrial Aerodynamics*, vol. 5, no. 3, pp. 357–372, 1980.

[34] K. Selvam, S. Kanev, J. W. van Wingerden, T. Van Engelen, and M. Verhaegen, "Feedback–feedforward individual pitch control for wind turbine load reduction," *International Journal of Robust and Nonlinear Control*, vol. 19, no. 1, pp. 72–91, 2009.

[35] J. M. Jonkman, "Dynamics of offshore floating wind turbinesmodel development and verification," *Wind Energy*, vol. 12, no. 5, pp. 459–492, 2009.

[36] M. W. Dingemans, *Water wave propagation over uneven bottoms: Linear wave propagation*, vol. 13, World Scientific, Singapore, 1997.

[37] J. Jonkman, *TurbSim User's Guide*, National Renewable Energy Laboratory, Golden, CO, Technical Report, NREL/TP-500-39797, 2009.

[38] W. J. Pierson Jr and L. Moskowitz, *A Proposed Spectral Form for Fully Developed Wind Seas based on the Similarity Theory of SA Kitaigorodskii*, New York University, New York, NY, Technical Report, N62306-1042, 1963.

[39] S. Hsu, E. A. Meindl, and D. B. Gilhousen, "Determining the power-law wind-profile exponent under near-neutral stability conditions at sea," *Journal of Applied Meteorology*, vol. 33, no. 6, pp. 757–765, 1994.

[40] J. M. Ortega and W. C. Rheinboldt, *Iterative Solution of Nonlinear Equations in Several Variables*, Academic Press, inc., San Diego, CA, 1970.

[41] J. G. Ziegler and N. B. Nichols, "Optimum settings for automatic controllers," *trans. ASME*, vol. 64, no. 11, pp. 759–768, 1942.

[42] B. D. Anderson and J. B. Moore, *Optimal Control: Linear Quadratic Methods*, Courier Corporation, U.S., 2007.

[43] C.-T. Chen, *Linear System Theory and Design*, Oxford University Press, Inc., New York, NY, 1995.

[44] W. L. Brogan, *Modern Control Theory*, Prentice Hall, NJ, 1991.

[45] X.-j. Yao, C.-C. Guo, and Y. Li, "Lpv h-infinity controller design for variable-pitch variable-speed wind turbine," in *Proceedings from IEEE 6th International Power Electronics and Motion Control Conference*, Wuhan, China, pp. 2222–2227, 2009.

[46] B. Connor, S. N. Iyer, W. E. Leithead, and M. J. Grimble, "Control of a horizontal axis wind turbine using h infinity control," in *Proceedings from First IEEE Conference on Control Applications*, Dayton, OH, pp. 117–122, 1992.

[47] B. A. Francis, *A Course in H_∞ Control Theory*, Springer, Berlin, Germany, 1987.

[48] J. E. Bibel and D. S. Malyevac, *Guidelines for the Selection of Weighting Functions for H-infinity Control*, Navel Surface Warfare Center, Dahlgren, VA, Technical Report, 92-16379, 1992.

[49] D. A. Smith, M. Harris, A. S. Coffey, T. Mikkelsen, H. E. Jørgensen, J. Mann, and R. Danielian, "Wind lidar evaluation at the danish wind test site in høvsøre," *Wind Energy*, vol. 9, no. 1-2, pp. 87–93, 2006.

[50] A. D. Wright, *Modern Control Design for Flexible Wind Turbines*, National Renewable Energy Laboratory, Golden, CO, Technical Report, NREL/TP-500-35816, 2004.

[51] K. Z. Østergaard, J. Stoustrup, and P. Brath, "Linear parameter varying control of wind turbines covering both partial load and full load conditions," *International Journal of Robust and Nonlinear Control*, vol. 19, no. 1, pp. 92–116, 2009.

[52] C. Sloth, T. Esbensen, and J. Stoustrup, "Active and passive fault-tolerant lpv control of wind turbines," in *Proceedings of American Control Conference*, Baltimore, MD, pp. 4640–4646, 2010.

[53] C. Sloth, T. Esbensen, and J. Stoustrup, "Robust and fault-tolerant linear parameter-varying control of wind turbines," *Mechatronics*, vol. 21, no. 4, pp. 645–659, 2011.

Appendix A

Physical Constants for the 5MW Sample WTS

This appendix lists the physical constants used for the sample WTS in Chapters 3, 4 and 5. Surfaces such as the C_p and C_t curves are not given, but the method for obtaining them is explained in the thesis body.

Property	Variable	Value	Unit
Water density	ρ	1025	kg/m^3
Physical mass	m_g	$14,072,718$	kg
Total inertia about x-axis of body frame	I_{xx}	$1.695e10$	$kg \cdot m^2$
Total inertia about y-axis of body frame	I_{yy}	$1.695e10$	$kg \cdot m^2$
Total inertia about z-axis of body frame	I_{zz}	$1.845e10$	$kg \cdot m^2$

Table A.1: General Properties

Property	Variable	Value	Unit
Air density	ρ_a	1.225	kg/m^3
Effective rotor radius	R_r	62.94	m
Distance vector from COM to center of thrust	$\vec{r}_{gt}$	$\begin{bmatrix} -5 \\ 0 \\ 99.889 \end{bmatrix}$	m
Rotor Inertia	J_r	$3.5444e7$	$kg \cdot m^2$
Generator Inertia	J_g	$5.34116e2$	$kg \cdot m^2$
Driveshaft stiffness on rotor side	k_r	$8.676e8$	Nm/rad
Driveshaft damping on rotor side	b_r	$6.215e6$	$Nm \cdot s/rad$
Gear ratio	N_{gr}	97	$[-]$

Table A.2: Aerodynamic Properties

Property	Variable	Value	Unit
Submerged density of the line	ρ_c	113.35	kg/m
Length of line	l_{cat}	835.5	m
Pretension of line	EA	$7.5363e8$	N
Distance vector from COM to line 1 attachment point	$\vec{r}^{\,b}_{gp1}$	$\begin{bmatrix} -40.868 \\ 0 \\ -4.11 \end{bmatrix}$	m
Distance vector from COM to line 2 attachment point	$\vec{r}^{\,b}_{gp2}$	$\begin{bmatrix} 20.434 \\ -35.3927 \\ -4.11 \end{bmatrix}$	m
Distance vector from COM to line 3 attachment point	$\vec{r}^{\,b}_{gp3}$	$\begin{bmatrix} 20.434 \\ 35.3927 \\ -4.11 \end{bmatrix}$	m
Location of line 1 attachment point	$\vec{x}_{anc1}$	$\begin{bmatrix} -837.6 \\ 0 \\ -200 \end{bmatrix}$	m
Location of line 2 attachment point	$\vec{x}_{anc2}$	$\begin{bmatrix} 418.8 \\ -725.3829 \\ -200 \end{bmatrix}$	m
Location of line 3 attachment point	$\vec{x}_{anc3}$	$\begin{bmatrix} 418.8 \\ 725.3829 \\ -200 \end{bmatrix}$	m

Table A.3: Mooring Line Properties

Property	Variable	Value	Unit
Damping coefficient for columns c_{a1}, c_{a2}, c_{a3}	$C_{d,a}$	0.68	$[-]$
Damping coefficient for columns c_{b1}, c_{b2}, c_{b3}, c_{c1}, c_{c2}, c_{c3}	$C_{d,bc}$	0.61	$[-]$
Damping coefficient for innermost columns c_{a4},c_{b4}, c_{c4}	$C_{d,4}$	0.56	$[-]$
Damping coefficient for heave plates	C_{dz}	4.8	$[-]$
Added mass coefficient for outer columns	C_a	0.63	$[-]$
Added mass coefficient for heave plates	C_{az}	0.67	$[-]$
Length of columns c_{a1}, c_{a2}, c_{a3}	l_a	6	m
Length of columns c_{b1}, c_{b2}, c_{b3}	l_b	4.11	m
Length of columns c_{c1}, c_{c2}, c_{c3}	l_c	9.889	m
Diameter of columns c_{a1}, c_{a2}, c_{a3}	$D_{d,a}$	24	m
Diameter of columns c_{b1}, c_{b2}, c_{b3}, c_{c1}, c_{c2}, c_{c3}	$D_{d,bc}$	12	m
Diameter of innermost columns c_{a4},c_{b4}, c_{c4}	$D_{d,4}$	8.054	m
Distance vector from COM to column c_{a1} center (undisplaced)	$\vec{r}^{\,b}_{ga1}$	$\begin{bmatrix} -28.87 \\ 0 \\ -7.11 \end{bmatrix}$	m
Distance vector from COM to column c_{b1} center (undisplaced)	$\vec{r}^{\,b}_{gb1}$	$\begin{bmatrix} -28.87 \\ 0 \\ -2.06 \end{bmatrix}$	m
Distance vector from COM to column c_{c1} center (undisplaced)	$\vec{r}^{\,b}_{gc1}$	$\begin{bmatrix} -28.87 \\ 0 \\ 4.94 \end{bmatrix}$	m
Distance vector from COM to column c_{a2} center (undisplaced)	$\vec{r}^{\,b}_{ga2}$	$\begin{bmatrix} 14.43 \\ -25 \\ -7.11 \end{bmatrix}$	m
Distance vector from COM to column c_{b2} center (undisplaced)	$\vec{r}^{\,b}_{gb2}$	$\begin{bmatrix} 14.43 \\ -25 \\ -2.06 \end{bmatrix}$	m
Distance vector from COM to column c_{c2} center (undisplaced)	$\vec{r}^{\,b}_{gc2}$	$\begin{bmatrix} 14.43 \\ -25 \\ 4.94 \end{bmatrix}$	m

Table A.4: Hydrodynamic Properties

Distance vector from COM to column c_{a3} center (undisplaced)	$\vec{r}^{\,b}_{ga3}$	$\begin{bmatrix} 14.43 \\ 25 \\ -7.11 \end{bmatrix}$	m
Distance vector from COM to column c_{b3} center (undisplaced)	$\vec{r}^{\,b}_{gb3}$	$\begin{bmatrix} 14.43 \\ 25 \\ -2.06 \end{bmatrix}$	m
Distance vector from COM to column c_{c3} center (undisplaced)	$\vec{r}^{\,b}_{gc3}$	$\begin{bmatrix} 14.43 \\ 25 \\ 4.94 \end{bmatrix}$	m
Distance vector from COM to column c_{a1} center (undisplaced)	$\vec{r}^{\,b}_{ga4}$	$\begin{bmatrix} 0 \\ 0 \\ -7.11 \end{bmatrix}$	m
Distance vector from COM to column c_{b1} center (undisplaced)	$\vec{r}^{\,b}_{gb4}$	$\begin{bmatrix} 0 \\ 0 \\ -2.06 \end{bmatrix}$	m
Distance vector from COM to column c_{c1} center (undisplaced)	$\vec{r}^{\,b}_{gc4}$	$\begin{bmatrix} 0 \\ 0 \\ 4.94 \end{bmatrix}$	m

Table A.5: Hydrodynamic Properties (cont'd)

Appendix B

Controller Parameters

This appendix lists the final controller parameters used for the validation tests in Chapter 5.

B.1 PID Parameters

The PID parameters are shown in Table B.1.

Table B.1: PID Values

Gain	PID 1	PID 2	PID 3	PID 4	PID 5	PID 6
P	250	100	-0.2	-10	50	0.002
I	200	1	-0.05	-2.5	5	0.0002
D	100	10	0	0	0	0

B.2 LQR Parameters

The LQR matrices $\underline{\mathrm{K}}_a$ and $\underline{\mathrm{K}}$ are given in B.1 and B.2, respectively.

$$\underline{\mathrm{K}}_a^T = \begin{bmatrix} -2.25\mathrm{e}{-05} & -5.40\mathrm{e}{-03} & 4.16\mathrm{e}{-10} \\ -2.29\mathrm{e}{-05} & -5.55\mathrm{e}{-03} & 5.14\mathrm{e}{-10} \\ 5.15\mathrm{e}{-05} & 1.24\mathrm{e}{-02} & 3.24\mathrm{e}{-11} \\ 2.84\mathrm{e}{-03} & 6.83\mathrm{e}{-01} & 2.72\mathrm{e}{-07} \\ 2.92\mathrm{e}{-05} & -1.21\mathrm{e}{-03} & -8.60\mathrm{e}{-12} \end{bmatrix}, \tag{B.1}$$

$$\underline{\mathrm{K}}^T = \begin{bmatrix} -3.81\mathrm{e}{-03} & -4.14\mathrm{e}{-01} & -2.16\mathrm{e}{-07} \\ -8.47\mathrm{e}{-04} & -9.63\mathrm{e}{-02} & 1.72\mathrm{e}{-08} \\ 6.43\mathrm{e}{-03} & 1.66\mathrm{e}{-01} & 2.97\mathrm{e}{-07} \\ 7.27\mathrm{e}{-01} & 1.63\mathrm{e}{+02} & 5.21\mathrm{e}{-05} \\ -2.15\mathrm{e}{+00} & -4.43\mathrm{e}{+02} & -2.23\mathrm{e}{-04} \\ 1.09\mathrm{e}{-02} & 1.04\mathrm{e}{+00} & 1.41\mathrm{e}{-06} \\ -5.77\mathrm{e}{+02} & 1.30\mathrm{e}{+04} & 2.23\mathrm{e}{-04} \\ 1.35\mathrm{e}{+00} & -1.41\mathrm{e}{+00} & 2.59\mathrm{e}{-06} \\ 4.89\mathrm{e}{-01} & -4.08\mathrm{e}{-01} & 3.84\mathrm{e}{-06} \\ -1.66\mathrm{e}{-01} & 9.07\mathrm{e}{-01} & 4.39\mathrm{e}{-06} \\ -5.19\mathrm{e}{+01} & 2.23\mathrm{e}{+02} & -1.59\mathrm{e}{-03} \\ 1.42\mathrm{e}{+02} & -7.06\mathrm{e}{+02} & 4.28\mathrm{e}{-03} \\ -1.11\mathrm{e}{-02} & 1.99\mathrm{e}{+00} & 7.22\mathrm{e}{-08} \\ -3.68\mathrm{e}{+02} & 5.33\mathrm{e}{+03} & 4.63\mathrm{e}{-05} \\ 2.54\mathrm{e}{+00} & -2.91\mathrm{e}{+01} & -1.28\mathrm{e}{-06} \end{bmatrix}. \quad \text{(B.2)}$$

B.3 Parameters for LQR Observer and H_∞ Controllers

Because of the large size of the observer matrix and the H_∞ systems, the values have not been tabulated in this thesis. Instead, they are available at `http://www.sites.mech.ubc.ca/ cel/files.php`.